IACMI/R003-2020/7.07

Materials Development and Advanced Process Simulation for Additive Manufacturing with Fiber-Reinforced Thermoplastics

Author: Alan Wedgewood
Date: February 27,2020

Final Technical Report
IACMI/R003-2020/7.07

Approved for Public Release.
Distribution is Unlimited.

U.S. DEPARTMENT OF
ENERGY

DOCUMENT AVAILABILITY

Reports produced after January 1, 1996, are generally available free via US Department of Energy (DOE) SciTech Connect.

Website http://www.osti.gov/scitech/

Reports produced before January 1, 1996, may be purchased by members of the public from the following source:

National Technical Information Service
5285 Port Royal Road
Springfield, VA 22161
Telephone 703-605-6000 (1-800-553-6847)
TDD 703-487-4639
Fax 703-605-6900
E-mail info@ntis.gov
Website http://www.ntis.gov/help/ordermethods.aspx

Reports are available to DOE employees, DOE contractors, Energy Technology Data Exchange representatives, and International Nuclear Information System representatives from the following source:

Office of Scientific and Technical Information PO
Box 62
Oak Ridge, TN 37831
Telephone 865-576-8401
Fax 865-576-5728
E-mail reports@osti.gov
Website http://www.osti.gov/contact.html

Acknowledgements

The information, data, or work presented herein was funded in part by the Office of Energy Efficiency and Renewable Energy (EERE), U.S. Department of Energy, under Award DE-EE0006926

We would like to acknowledge the support of the following DuPont scientists and engineers, who made significant contributions to this report: Mario A. Martinez (resin development and production), Dylan Garges (mechanical testing), Chad D. DeLong (CT scan and fiber orientation determinations) and Alexia J. Russo (DSC testing).

We also like to acknowledge the support of the following Purdue graduate research assistants, who made significant contributions to the work presented in this report: Vasudha N. Kapre (post-processing of point cloud data and specimen preparation), Sushrut Karmarkar (specimen preparation), Miguel Ramirez (specimen preparation).

Materials Development and Advanced Process Simulation for Additive Manufacturing with Fiber-Reinforced Thermoplastics

Principal Investigator: Alan Wedgewood
Organization: DuPont
Address: Chestnut Run Plaza 713/108
Wilmington, DE 19805
Phone: 302-999-3302
Email: alan.r.wedgewood@dupont.com

Co-authors:

Pasita Pibulchinda (Purdue)

Eduardo Barocio Vaca (Purdue)

Charles Hill (Local Motors)

Alan Wedgewood (DuPont)

Michael J. Bogdanor (Purdue)

Date Published: (February, 2020)

Prepared by:
Institute for Advanced Composites Manufacturing Innovation
Knoxville, TN 37932
Managed by Collaborative Composite Solutions, Inc.
For the
U.S. DEPARTMENT OF ENERGY
Under contract DE- EE0006926

Project Period:
(05/2019 – 02/2020)

Approved For Public Release

CONTENTS

LIST OF ACRONMYMS

CMSC	Composites Manufacturing and Simulation Center
AM	Additive Manufacturing
BAAM	Big Area Additive Printer
CAMRI	Composites Additive Manufacturing Research Instrument
CC	Compliance Calibration
CF	Carbon Fiber
CNC	Computer Numerical Controlled
CT	Computerized Tomography
CTE	Coefficient of Thermal Expansion
DCB	Double Cantilever Beam
DIC	Digital Image Correlation
DMA	Dynamic Mechanical Analysis
DOE	Department of Energy
DSC	Differential Scanning Calorimetry
EDAM	Extrusion Deposition Additive Manufacturing
GF-PA	Glass Fiber Polyamide
IACMI	Institute for Advanced Composites Manufacturing Innovation
LSAM	Large Scale Additive Manufacturing
MBT	Modified Beam Theory
MCC	Modified Compliance Calibration
MTS	Mechanical Test System
OEM	Original Equipment Manufacturer
ROI	Region of Interest
SLS	Selective Laser Sintering
PA	Polyamide
GF-PA	Glass Fiber reinforced Polyamide
ABS	Acrylonitrile Butadiene Styrene

LIST OF FIGURES

LIST OF TABLES

EXECUTIVE SUMMARY

DuPont, Local Motors, and the Composites Manufacturing and Simulation Center (CMSC) at Purdue worked together to advance process simulation capabilities for Additive Manufacturing (AM) and develop printable short fiber reinforced semi-crystalline engineering thermoplastics suitable for vehicle components. DuPont provided one candidate thermoplastic material, which was evaluated against the following three criteria:

1) Printability using extrusion additive manufacturing processes

2) Suitability for vehicle applications based on mechanical coupon screening tests

3) Predictive capability of process simulations

Indiana Manufacturing Institute provided modeling and simulation technology and access to Purdue's lab scale AM printer. Local Motors provided mechanical property requirements and printed demonstration prototype components using their Thermwood Large Scale Additive Manufacturing (LSAM) printer.

To meet the performance and cost requirements of the automotive industry, high fiber content semi-crystalline engineering materials are required. Printing experience and property data for a 50% by weight short glass fiber reinforced material were gathered. Further, material properties required for simulating the printing process with the glass-fiber reinforced material were characterized. Knowledge was acquired with regards to the processability and performance of this thermoplastic material. Predictions of part deformation and crystallinity level were verified against experimental observations. Any significant results other than verification of simulation, e.g., novel material identified here would be impactful.

1. BACKGROUND

DuPont, Local Motors, and the Composites Manufacturing and Simulation Center (CMSC) at Purdue jointly proposed this IACMI project at TRL 3 to advance process simulation capabilities for Additive Manufacturing (AM) and develop a printable fiber reinforced semi-crystalline engineering thermoplastic suitable for vehicle components. Advanced process simulation for additive manufacturing processes is deemed essential to the ability to design and fabricate structural components from printable materials. An understanding of the effect of processing conditions on the mechanical performance, along with the ability to print in a manner that meets the final geometric part tolerances, requires computer aided design tools, such as those being developed in support of this work. Understanding the trade-offs of selecting glass versus carbon fiber reinforcements addresses questions regarding cost and processing trade-offs. Assessing the printability of high glass fiber content systems, as done in this work, provides critical input to selecting the best fiber reinforcement type for an automotive application.

1.1. Proposed Innovation/Solution:

Aligning a material manufacturer with an automotive OEM accelerates commercial deployment of semi-crystalline engineering thermoplastics that can be printed on large volume AM machines to deliver functional vehicle components. The ability to produce structural, load carrying components will help drive the development of AM for large scale production. DuPont currently supplies reinforced engineering thermoplastic polymer systems to the automotive industry, however, the need for printable materials with high performance per unit cost remains an unmet industry need.

The project focused on screening one semi-crystalline engineering thermoplastic candidate against three criteria: 1) Printability using extrusion additive manufacturing processes, 2) Suitability for vehicle applications based on coupon screening tests, and 3) Predictive capability of process simulations. DuPont provided both thermoplastic materials and fundamental knowledge regarding how to model these materials. Indiana Manufacturing Institute provided modeling and simulation technology and access to Purdue's lab scale printer. Local Motors provided manufacturing requirements, demonstration prototype component targets and access to Thermwood's LSAM and Cincinnati Incorporated's BAAM commercial printers.

The material selected was Zytel® FE370093 BK309, a 50% glass filled specialty polyamide resin intended for additive manufacturing applications (GF-PA). The base polymer used for this Zytel® glass-reinforced polyamide is a unique specialty polyamide blend optimized for ultra-low shrinkage. The ultra-low shrinkage technology developed for Zytel® polyamides for 3D printing reduces mold shrinkage while retaining semi-crystalline behavior. Minimizing shrinkage and warpage enables parts with large and complex geometries to be printed reliably with high fidelity to the original design. With high modulus (>15 GPa) and tensile strength (<180 MPa), coupled to good impact strength (>90 kJ/m^2 Izod impact strength), this Zytel® specialty polyamide resin shows an excellent balance of mechanical properties.

Ease of printing, excellent resolution and attractive appearance of printed parts, while difficult to quantify, are important features of a 3D-printing composition. Articles prepared from the Zytel® glass-reinforced polyamide 3D-printing composition have an attractive sheen and a relatively smooth surface finish given the high amount of filler. The molten extrudate maintains high viscosity and melt strength while exiting the printer nozzle, which leads to good resolution when printing fine features and excellent performance when printing bridging features.

1.2. Role of Project Work In Demonstrating Solution:

The goal of the Technical Collaboration Project was to advance AM process simulation methods with the development of semi-crystalline engineering thermoplastics suitable for AM, to yield a robust manufacturing capability for producing vehicle components. Combining IACMI's advanced modeling and simulation capabilities being developed at the Purdue's Composites Manufacturing and Simulation Center, DuPont's ability to formulate and manufacture fiber reinforced thermoplastics and Local Motors' innovative use of AM to produce commercial vehicles, created a team with the talents required to deliver this robust manufacturing capability.

1.3. Expected Impact On Energy Savings And/Or Large-Scale Use Of Carbon Fiber Composite Materials:

The effect of additive manufacturing (AM) on energy demand for the aerospace and construction sector showed the potential for energy savings of 5-25% and 4-21%, respectively [1]. Weight reductions that are possible via AM was the largest factor for aerospace energy savings. For automotive and aerospace selective laser sintering (SLS) of metals has led the way, offering more efficient production processes and providing light-weight constructions, which lowers the vehicles energy demand [2]. This work aims to extends the adoption of AM for automotive to include semi-crystalline engineering polymers. Expanding the AM material options for AM helps achieve more sustainable vehicle production by shortening process chains, allowing more efficient process that reduce material consumption, and capturing the benefits of light weight automotive designs. Understanding the viability of a 50% by weight short fiber glass composite system as a 3D Printable resin, will help define the need for carbon fiber reinforced composites for automotive applications. Simulation methods advanced in this work can be applied to a wide variety of materials including both glass and carbon fiber reinforced resins.

1.4. PROJECT GOALS

The proposed work focused on screening one semi-crystalline engineering thermoplastic candidate against three criteria: 1) Printability using extrusion additive manufacturing processes, 2) Suitability for vehicle applications based on coupon screening tests, and 3) Predictive capability of process simulations. This project aimed to extend the capability of the AM process simulation methods to new material systems. Specifically, glass fiber-reinforced semi-crystalline engineering

thermoplastics suitable for AM of vehicle components. To meet the performance and cost requirements of the automotive industry, high fiber content semi-crystalline engineering materials are required. This program offers printing experience and property data for a high glass fiber content reinforced material. As a result, new technical knowledge was gained with regards to the processability and performance of high fiber content semi-crystalline engineering materials. In addition, this work provides an initial assessment of our ability to simulate both the processing and mechanical performance of components printed with a high fiber content material.

1.4.1. Printability

The printability assessment used test geometries, such as a single-wall structure with overhangs and straight segments, to not only assess printability of the reinforced polymer, but also to prepare coupons to experimentally measure the mechanical properties of the printed material and the interlayer fracture energy. Printing speeds in the range from 500 mm/min to 7500 mm/min were considered for investigation in the lab scale system at Purdue while printing speeds, which are coupled to extruder throughput and bead size, in the range of 500 mm/min to 24,000 mm/min can be readily investigated with the BAAM and LSAM systems. Factors that affect material processing, such as extrusion speeds, nozzle design, and deposition rate were investigated. Layer to layer adhesion and bead and inter-bead gap spacing dimensions were measured to assess basic printability requirementsFor lab scale printing, the objective is measured bead dimensions and inter-bead gap spacing after making a right angle turn. The acceptable variation or a lab scale printer (CAMRI) is less than 5% variation in the bead shape and the inter-bead gaps smaller than 5% of the bead width. For large scale printing (BAAM or LSAM) the objective is less than 10% variation in bead shape, with inter-bead gaps smaller than 10% of the bead width. It is expected that this work will result in a few specific equipment modifications.

1.4.2. Suitability for Vehicle Applications – Mechanical Performance

Mechanical and physical testing of parts was done to validate the process simulation and fabrication methods used to produce a fully functional part. Tensile properties were measured for lab scale produced coupons in the print, transverse and stack directions. Measurements were made with a laser scanner, to compare the printed part dimensions versus the designed dimensions. To assess the effect of scale on the printability and mechanical properties, mechanical testing was repeated for samples printed on a large-scale printing machine (LSAM). A comparison to the tensile property requirements for vehicle applications provided by Local Motors was done to assess the suitability of the candidate material for its use in vehicle applications.

1.4.3. Predictive Process Simulation

The flexibility to create almost any shape, hastens the need to develop advanced simulation approaches able to account for a myriad of process phenomena, such as transient heat transfer, viscoelastic material behavior, crystallization kinetics, part shrinkage, and residual stress

development. Understanding and modeling these phenomena existing in the AM process is a necessary step to enable the translation of designs into fully functional finished parts. Thus, the focus of this IACMI project, is to extend this approach to large volume AM, by leveraging the process simulation understandings offered by the Composites Manufacturing and Simulation Center at Purdue to further guide the development of fiber reinforced engineering polymers suitable for AM of vehicle components. The simulation predictions were validated against experimental measurements of the following performance parameters:

A) Part deformation after printing caused by internal stresses

B) Part crystallinity after printing caused by thermal history.

Both the shape change of the test geometry and the parts crystallinity was predicted through Purdue's process simulation tools and compared to experimental results.

1.4.4. Phase 2 Go/No Go Decision

The goal was to determine if the candidate material is suitable for vehicle applications and prototype part scale-up in Phase 2. The Go/No Go decision involves an assessment of the candidate material's suitability for vehicle applications, based on screening tests and predictive simulation modeling deliverables, define in the 1st and 2nd quarter milestones. If a suitable candidate, this material will be used in Phase 2. If not a suitable candidate, recommendations for developing improved candidate materials will be implemented in the beginning of Phase 2, by repeating the Phase 1 candidate evaluation steps. The proposed Phase 2 project will engage Local Motors as an OEM partner to both identify application targets and produce representative prototype parts, DuPont as a material supplier to both provide optimized printable materials, and the CMSC at Purdue to advance predictive simulation capabilities for AM.

1.4.5. Milestones

Milestone 7.7.2.1 - Measured interlayer fracture energy versus goal of 75% of the fracture energy of bonded layer strength obtained from heat-treated printed samples to achieve maximum strength through crystallization and enhanced polymer diffusion. (November 2019) Purdue University.

Milestone 7.7.2.2 - Measured tensile properties in the print and transverse directions versus the target properties listed below. (November 2019) Local Motors

- X-direction (Parallel to the bead) E= 14 GPa Strength = 100 MPa
- Y-Direction (Transverse to the bead) E= 3.5 GPa Strength = 33 MPa
- Z-direction (Stack direction) E = 3.5 GPa Strength = 33 MPa

Milestone 7. 7 .2.3 - Measured part deformation (spring back) versus predicted deformation with a goal of+/- 10%. Measured part crystallinity versus predicted goal of+/- 5%. (January 2020)

Go/No-Go 7. 7.1 - A team decision that material and process data measured in Phase 1 indicate with a high probability that executing the Phase 2 development plan will result in a semi-crystalline engineering thermoplastic, suitable for producing vehicle components, as determined by achieving the phase 1 milestone goals. Decision will be reported to IACMI and DOE. (January 2020) DuPont.

1.5. The Extrusion Deposition Additive Manufacturing Process

The Extrusion Deposition Additive Manufacturing (EDAM) process implemented in the LSAM machine from Thermwood shown in Figure 1.1. LSAM utilizes a large single screw extruder to melt pelletized polymer composite feedstock and provide pressure to a melt pump (gear pump) which provides precise flow control of the material from a nozzle. As the nozzle is translated across the surface of a part being formed, a compression roller follows the nozzle and provides a gentle pressure to compact the bead and produce a given layer height. Figure 1.2 shows the print head and the compression roller used in the LSAM. The combination of flow rate, nozzle speed, and roller height provides the control on bead dimensions for the final part. The use of fiber reinforced polymers in EDAM has enabled additive manufacturing of parts in the scale of meters [3]. The flow developed inside the nozzle as well as during deposition of a bead governs the orientation of the fibers, which control the thermal, mechanical, thermoelastic and thermoviscoelastic properties. Process conditions can be such that fibers dominantly orient parallel to the printing direction, thereby enhancing properties such as thermal conductivity, coefficient of thermal expansion, elastic modulus, etc. in this direction. The anisotropic properties of the printed composite and the non-isothermal nature of this process lead to residual stresses that can manifest as warpage during and after the manufacturing process of a geometry.

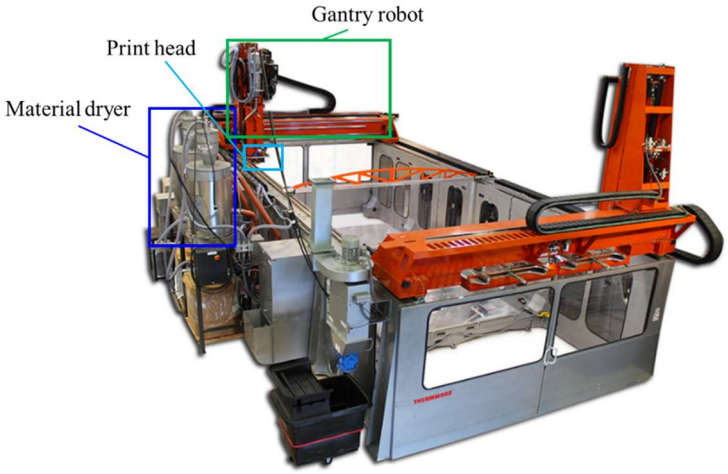

Figure 1.1: Thermwood LSAM Machine 10’ x 20’ model shown.

One of the primary challenges of this process is that the material contracts during cooling, crystallization, and solidification, such that deformations and internal stresses result. Process simulation will provide the capability to predict these effects and therefore prevent the trial and

error approach to achieving successful designs. In order to develop appropriate input parameters for the model, critical material properties need to be determined by direct testing in order to generate a material card for the model.

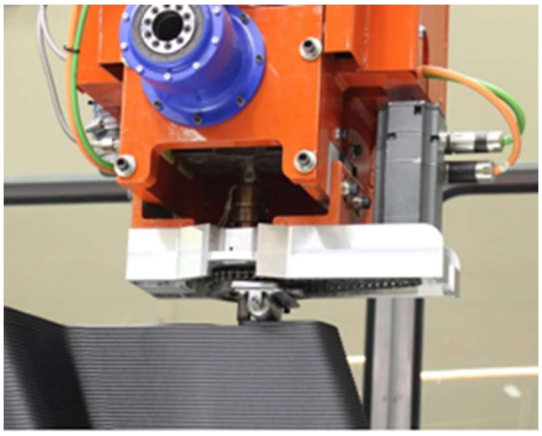

Figure 1.2: LSAM print head showing nozzle and compression roller.

2. TECHNICAL RESULTS

Detail descriptions of the printability assessment, material characterization, and process simulations carried out throughout this program are presented in this section. First, a printability assessment was carried out to study the effects that process conditions have on the tensile properties and fiber orientation distribution. Interlayer fracture tests were also carried out to determine the interlayer fracture toughness. Second, an extensive material characterization program was carried out to determine thermal, mechanical, thermomechanical, and thermoviscoelastic properties of the printed beads. The outcome of the characterization program was a digital material card required for simulating the printing process with ADDITIVE3D©[4][5] [6]¨ Third, two geometries were designed and additively manufactured in the LSAM. Measurements of temperature throughout the print and of deformation developed after printing served for validating predictions made with ADDITIVE3D©.

2.1. Printability Assessment

Prior experience of Local Motors in processing this class of material was helpful to rapidly establish extrusion conditions such as temperature profiles for the extruder and print speeds. Table 2.1 lists the extrusion condition used for processing the GF-PA in the LSAM. The heating zones listed in Table 2.1 are located in the same order as listed from the top of the extruder where pelletized feedstock enters the extruder to the tip of nozzle where beads of molten material leaves the nozzle. The primary focus of the printability assessment was on investigating the effects of deposition conditions on the mechanical properties and fiber orientation distribution in the print

direction. The primary deposition condition investigated was the compaction ratio or aspect ratio of the printed bead defined as the ratio of the final width to the final height. A greater aspect ratio involves more deformation of the initially circular bead cross-section and involves more flow of material in the direction transverse to the print direction. This initial study was aimed to provide additional understanding on the effect of the bead deposition conditions to the tensile properties of the printed material which also reflects in changes to other material properties that affect the overall deformation and residual stresses developed during the printing process of a part.

Table 2.1: Extrusion conditions used in the LSAM.

Extrusion Conditions	Value
Extrude Hopper ($°C$)	250
Extrude Zone 1 ($°C$)	260
Extrude Zone 2 ($°C$)	282
Extrude Zone 3 ($°C$)	296
Melt Pump Connector ($°C$)	261
Melt Pump ($°C$)	296
Extrusion Nozzle ($°C$)	343
Deposition Speed (mm/min)	2540

Aspect ratios of 3, 4 and 5, were investigated in the LSAM at Local Motors as well as with the Composites Additive Manufacturing Research Instrument (CAMRI) at Purdue University [6]. A constant bead-to-nozzle area ratio of 0.7712 was used in both cases. Thus, the combination of flow rate emerging from the nozzle to the speed of the print head was constant and the bead height was the only parameter changed. A bead-to-nozzle area ratio greater than one indicates that the flow emerging from the nozzle extends in the direction transverse to the print direction, whereas a bead-to-nozzle area ratio lower than one indicates that the extrudate is stretched as it emerges from the nozzle. In the former case, the flow developed transverse to the print direction can cause some of the fibers to flow align transverse to the print direction. In the latter case, the fibers are more likely to flow align along the print direction due to the extensional flow developed as the extrudate is stretched. Figure 2.1 shows a schematic representation of the beads printed in the LSAM with the three different aspect ratios. A numeric notation is adopted to indicate the local material orientation with the 1-direction corresponding to the print direction, the 2-direction corresponding to the direction transverse to the print, and the 3-direction corresponding to the stacking direction as shown in Figure 2.1.

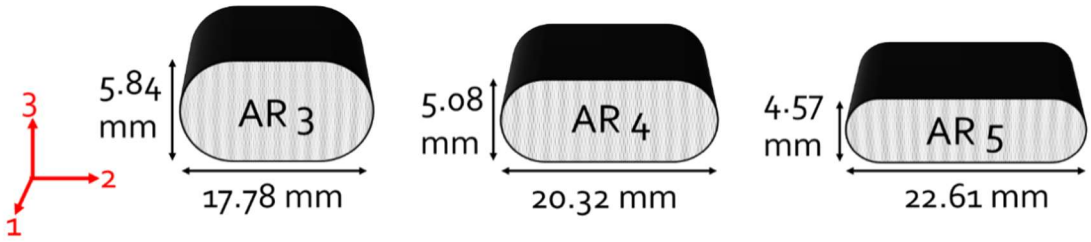

Aspect ratio	Bead to nozzle area ratio	Bead width (mm)	Bead Height (mm)
3	0.7712	17.78	5.84
4	0.7712	20.32	5.08
5	0.7712	22.61	4.57

Figure 2.1: Dimensions and schematic representation of beads with different aspect ratio.

2.1.1. Effects of Deposition Conditions on Fiber Orientation Distribution

In this program, the fiber orientation was obtained by using micro-Computerized Tomography (CT) technique scan-generated three-dimensional image of fibers. The raw CT-Scan data was collected using a Zeiss Xradia 510 Versa Micro CT instrument with a voxel size of 3.24um. The reconstructed data was a vertical stitch of 4 separate scans (each scan setting: 2001 frames, 20s exposure time, source voltage 80kV, and source power 7W). The reconstructed data was imported as 8-bit unsigned tiffs into Volume Graphics VGStudio Max 3.2 and filtered with a non-local means filter with a smoothing factor of 1. The fiber orientation was calculated using the Fiber Composite Material Analysis Add-in with an integration mesh defined by six cells in the thickness direction, 4 cells in the width direction, and 1 cell in the length.

The micro-CT scans were broken into finite rectangular sections as shown in the red sectioning lines in Figure 2.2: Micro CT scan of LSAM- AR 4..The orientation of the fibers within each of the finite rectangular sections was described through a second-order fiber orientation tensor [7].The average fiber orientation in the three-principal directions was calculated in each section. A11 is the orientation tensor in the 1 direction which is the print direction. Because the figure shows the bead's cross-sectional area, 1 direction is the direction pointing out of the page. A22 is the orientation tensor along the transverse direction which is to the left and right of the page. A33 is the orientation tensor along the stacking direction pointing up. A_{11}, A_{22}, and A_{33} can be calculated using the equation 2.1. Where θ is an angle away from the print direction and $\emptyset$ is an angle is the 2-3 plane.

$$A_{11} = \cos(\theta)$$

$$A_{22} = \sin(\theta)\cos(\emptyset)$$

$$A_{33} = \sin(\theta)\sin(\emptyset)$$

Table 2.2 listed the average fiber orientation in the 1-direction of the corresponding section in Figure 2.2: Micro CT scan of LSAM- AR 4.. The table of the average fiber orientation of the 2-direction and 3-direction can be found in Table 5.1 in the APPENDIX. The bolded numbers mean the section is completely filled with material, which is mainly in the middle of the bead. The regular unbolded numbers mean the section is not filled with material, therefore, they will need further calculation to obtain the actual area weighted average.

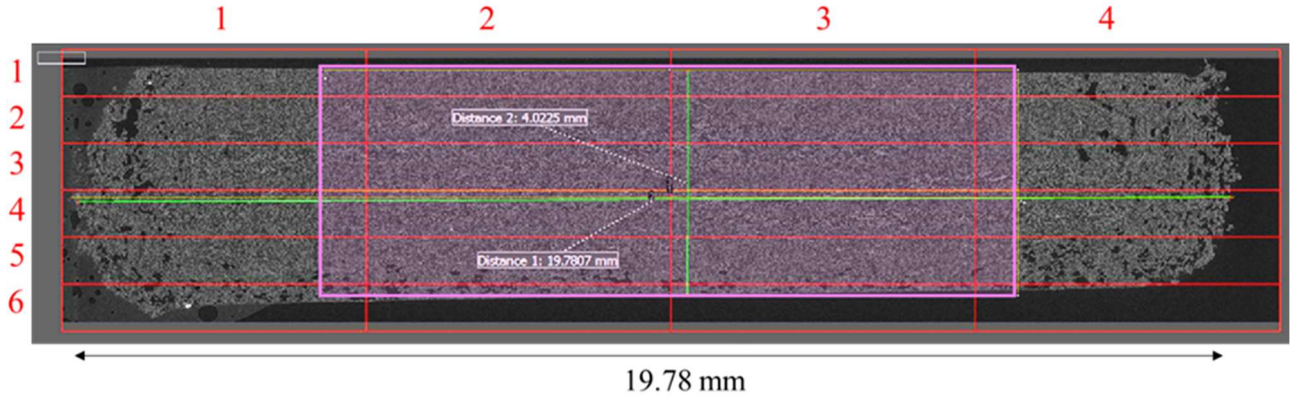

Figure 2.2: Micro CT scan of LSAM- AR 4.

Table 2.2: Fiber Orientation of LSAM- AR 4 in the 1-direction of each section of the bead.

A11 = 0.58	**1**	**2**	**3**	**4**
1	0.68	0.57	0.58	0.63
2	0.66	**0.47**	**0.51**	0.61
3	0.62	**0.44**	**0.43**	0.61
4	0.62	**0.49**	**0.45**	0.62
5	0.67	**0.62**	**0.6**	0.68
6	0.64	0.64	0.6	0.54

As shown in Table 2.2 the average fiber orientation in the outer region of the bead has higher A11 than in the middle region highlighted in blue. The final fiber orientation is a weighted area average of these sections. The weighted area average is preferred over the number average because the bead is an ellipse, therefore, the outer edge section is not completely filled with material. Therefore, the contribution of those outer edge sections should be less than the middle section which is completely filled with material. Area fraction is the area of the material in each section divided by the area of the CT scan rectangular divided section. For example, the section completely filled with material such as in the middle of the bead has an area fraction of 1. The section with only half of the area occupied with the material has an area fraction of 0.5. The ImageJ software was used to measure the area of the material filled in each section of the bead. The area weighted average fiber orientation of each section can be found in the APPENDIX.

For the mechanical testing purpose, the outer part of the bead or the curvature part of the bead was

removed by a wood planer. The outer part of the bead, in other words, the curvature part of the bead was machined away. It is inappropriate to assume the fiber orientation of the mechanical specimens, namely shear and tensile specimens to have the same fiber orientation as the whole bead's fiber orientation. Thus, another step is required. Figure 2.2 shows the region of the shear and tensile specimens in pink. ImageJ was again used to measure the area of the sections in pink. Therefore, the tensile specimen bead was only the area in pink shown in Figure 2.2. The area weighted fiber orientation of the pink region was calculated and shown in Figure 2.83 in the APPENDIX. Table 2.3 summarizes the fiber orientation tensor of the area weight whole bead and area weighted planed bead, highlighted in pink, which will be utilized in the characterization section.

Table 2.3: Summary of the area weighted average fiber orientation Tensor A_{ij} of LSAM- AR4 whole bead and planed bead.

Sample	Whole bead	Planed bead
LSAM – AR 4	$A_{ij} = \begin{bmatrix} 0.57 & 0 & 0 \\ 0 & 0.34 & 0 \\ 0 & 0 & 0.09 \end{bmatrix}$	$A_{ij} = \begin{bmatrix} 0.53 & 0 & 0 \\ 0 & 0.39 & 0 \\ 0 & 0 & 0.08 \end{bmatrix}$

Utilizing the same approach, the area weighted average fiber orientation tensor of CAMRI beads of aspect ratio of 3, 4, and 5 is listed in Table 2.4 below. As an example, Figure 2.3 shows the Micro CT scan of CAMRI- AR 3 with the remainder of the bead after machining in pink. The defect in the lower right area was introduced during the extraction of the sample from a printed panel.

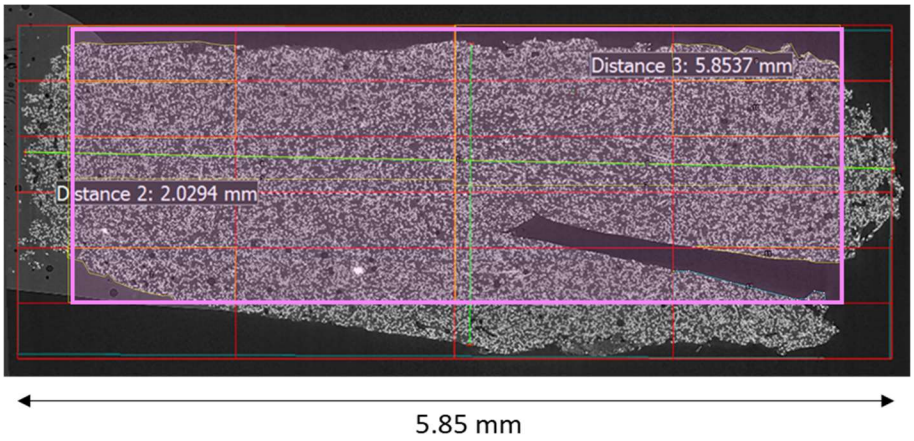

Figure 2.3: Micro CT scan of CAMRI- AR 3.

Table 2.4: Summary of the area weighted average fiber orientation Tensor A_{ij} of CAMRI- AR3, AR 4, and AR 5 whole bead and planed bead.

Aspect Ratio	Whole bead	Planed bead

CAMRI -AR 3	$A_{ij} = \begin{bmatrix} 0.69 & 0 & 0 \\ 0 & 0.23 & 0 \\ 0 & 0 & 0.08 \end{bmatrix}$	$A_{ij} = \begin{bmatrix} 0.69 & 0 & 0 \\ 0 & 0.24 & 0 \\ 0 & 0 & 0.07 \end{bmatrix}$
CAMRI -AR 4	$A_{ij} = \begin{bmatrix} 0.73 & 0 & 0 \\ 0 & 0.20 & 0 \\ 0 & 0 & 0.07 \end{bmatrix}$	$A_{ij} = \begin{bmatrix} 0.73 & 0 & 0 \\ 0 & 0.20 & 0 \\ 0 & 0 & 0.07 \end{bmatrix}$
CAMRI -AR 5	$A_{ij} = \begin{bmatrix} 0.74 & 0 & 0 \\ 0 & 0.19 & 0 \\ 0 & 0 & 0.07 \end{bmatrix}$	$A_{ij} = \begin{bmatrix} 0.70 & 0 & 0 \\ 0 & 0.24 & 0 \\ 0 & 0 & 0.06 \end{bmatrix}$

2.1.2. Effects of Deposition Conditions on Mechanical Properties

Boxes were printed with the LSAM for each aspect ratio and tensile samples were cut in the print direction from the long sides of the box (1 direction). First, the long sides of the box were planed to obtain the final uniform tensile bar gauge thickness (2 direction). Enough material was removed with a planer from each side to remove the rough surface created by the bead geometry. Based on the measured sample dimensions, 40% of the original printed bead width was removed or about 20% from each side.

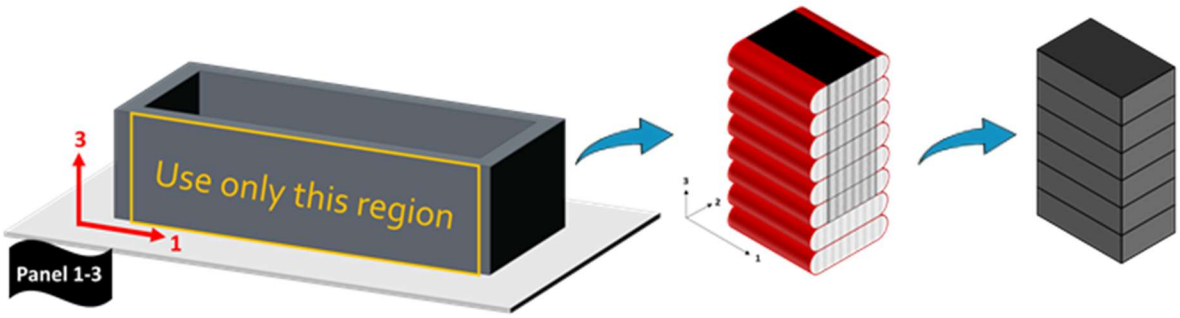

Figure 2.4: Illustration of the sequence followed for preparing specimens for tensile tests: printing box, extracting panels, machining of the panels.

Next, as depicted in Figure 2.4 above, rectangular pieces were machined in the print direction from the long side of the printed box. These tensile coupons were six printed bead layers wide (3 direction) and 165 mm long (1 direction). The gage width is designed to be the nearest integer of bead height closest to 20 mm. From these rectangular pieces, taper shouldered tensile bars were machined having a gauge width that was four beads wide (3 direction). As a result, the tab width is six beads wide or 1.5 times the gauge width. Though, not planed, the final gauge cross-sectional area was approximately 255 mm^2 for all three aspect ratios. All coupons were manufactured according to the ASTM D638 guidelines [8].

Tensile testing in the 1-direction was performed using a 100,000 lbf Servo Hydraulic Test Frame. The sample was held with hydraulic wedge grips with textured grip faces and the force was

measured with a 100,000 lbf load cell. The test speed was 2 mm/minute and data was collected at 20 Hz. A clip-on extensometer was used to measure the strain over a 2-inch gauge length. Figure 2.5 shows the test set-up including the servo hydraulic test frame, the load cell, and the extensometer.

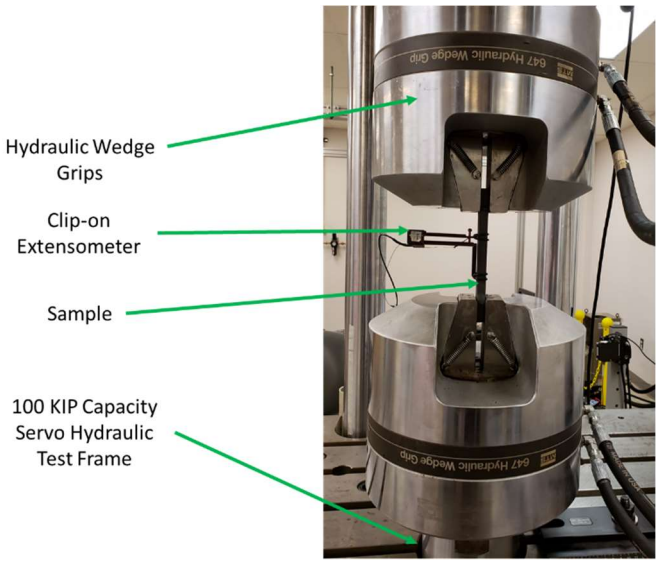

Figure 2.5: Illustration of servo hydraulic test set-up.

The Poisson ratio was determined using Digital Image Correlation (DIC) to measure the axial and transverse strain in the gauge length. The samples were tested at a rate of 2mm/minute and images of the sample were taken at a rate of 4 Hz during testing. A rectangular area was selected in the gauge section and an average value of the axial and transverse strains was calculated for each image. A plot of the transverse strain versus the axial strain was made and the slope of the resulting line between 0.05% and 0.25% axial strain was calculated to determine the Poisson Ratio. Figure 2.6 shows an example of the transverse versus the axial strain measured for one of the samples using the DIC.

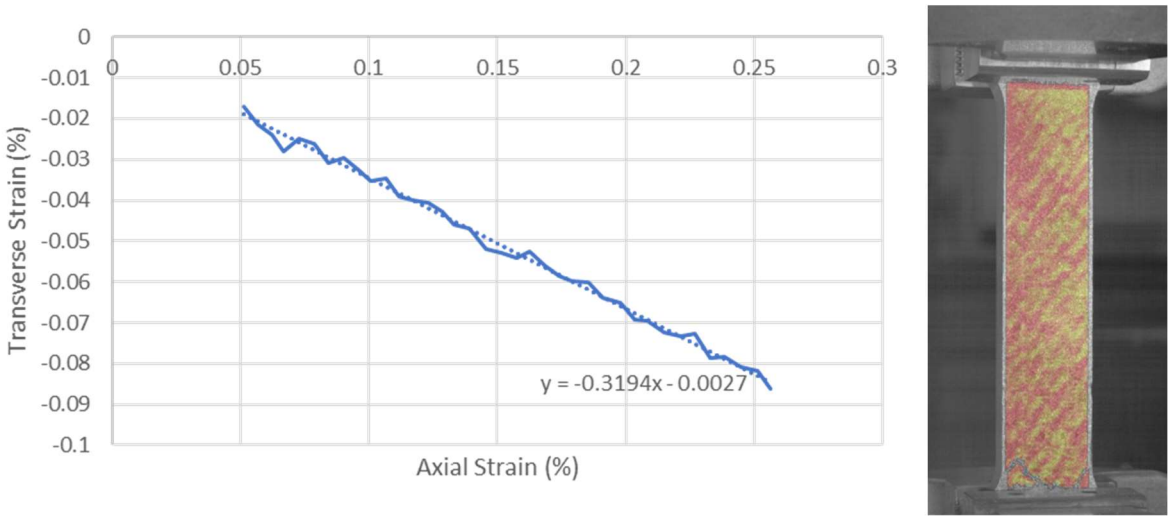

Figure 2.6: Example plot of the transverse versus axial strain measured by Digital Image Correlation used to determine the Poisson Ratio.

Tensile properties were measured in the print direction for the three different print conditions to assess the effect of the bead aspect ratio on the tensile modulus and strength. Figure 2.7 shows all sample failures initiated in the shoulder region at the interface between the continuous and interrupted print layer.

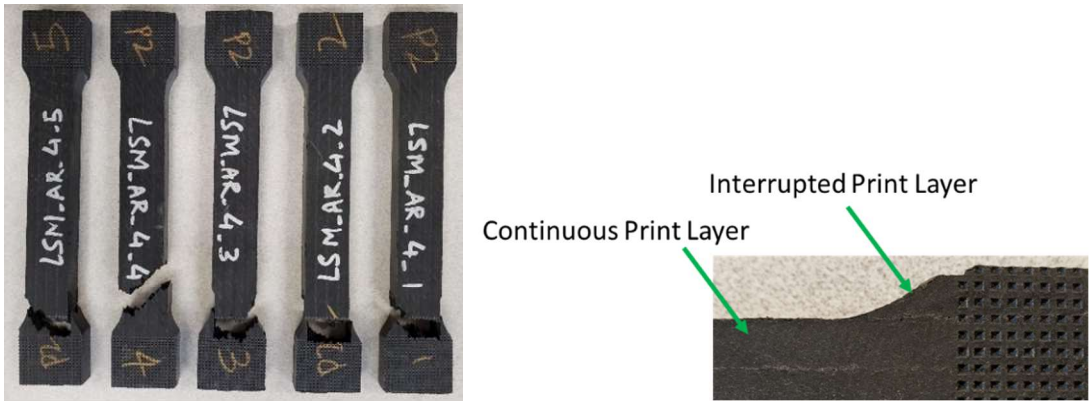

Figure 2.7: Failed LSAM -AR 4 sample, illustrating the initiation of failure in the shoulder region, between the continuous and interrupted print layers.

It is possible that failures occurred in this region due to additional shear stresses being generated due to uneven tensile load sharing between the interrupted print layer and the continuous print layer. A previous study of similarly shaped tensile bars revealed increased shear angle distribution in the shoulder region of the tensile bars. Shear angle is the principal strain angle, measure counterclockwise from the positive X-axis. Regions with higher shear angle, as shown in the blue and red color in Figure 2.8, indicate areas where additional shear stresses are being generated. Figure 2.8 shows the shear angle distribution at the surface of a specimen obtained with the Digital Image Correlation (DIC) system. It is possible that failure may be initiated in shear and not tensile failure. These samples may have increased strength if this effect can be minimized. Removing the

width of the tab section and testing completely rectangular bars with no interrupted print layers may yield increased strength.

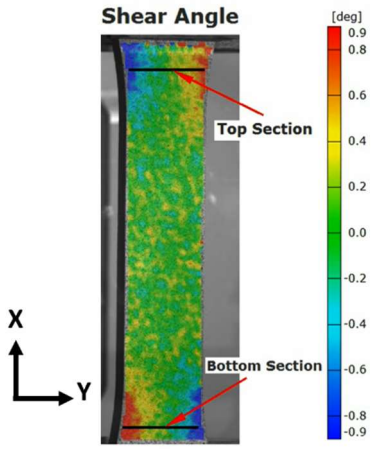

Figure 2.8: Digital Image Correlation image illustrating the high shear stress that develops in the shoulder region near the interface between the continuous and interrupted print layers.

Table 2.5 summarizes the tensile test results as a function of bead aspect ratio. As is shown, the results for the AR 4 & AR 5 samples were both similar to each other and higher than those found for the AR 3 samples. Consideration of the fiber orientation created by the processing conditions used and the material removed during sample preparation is expected to elucidate an understanding of this trend with aspect ratio. While the cross-sectional of the printed bead is equal for the three aspect ratios investigated, the area fraction of the bead removed in the planing process increases as the aspect ratio decreases. In other words, planing the panels printed with bead aspect ratios of three, four and five required a reduction in the bead cross-sectional area of at least 28%, 21%, and 16%, respectively. Further, this indicates that the elastic response obtained from the experimental tensile tests does not truly represent the variations resulting from variations in bead aspect ratio for the specimens printed in the LSAM. Time and budget constraints prevented measuring orientations for the aspect ratios of three and five which could have provided further understanding of the effects of the bead aspect ratio on the mechanical properties.

Table 2.5: Summary of tensile properties measured for different aspect ratios printed in the LSAM.

AR	Avg E1 (GPa)	SD	Avg Ult. Strength (MPa)	SD	Avg. Failure Strain (%)	SD	Poison Ratio
3	11.2	1.0	126.7	7.7	2.12	0.33	0.319
4	13.0	0.9	141.2	7.1	1.86	0.14	0.336
5	12.6	0.9	138.9	6.6	1.91	0.28	0.325

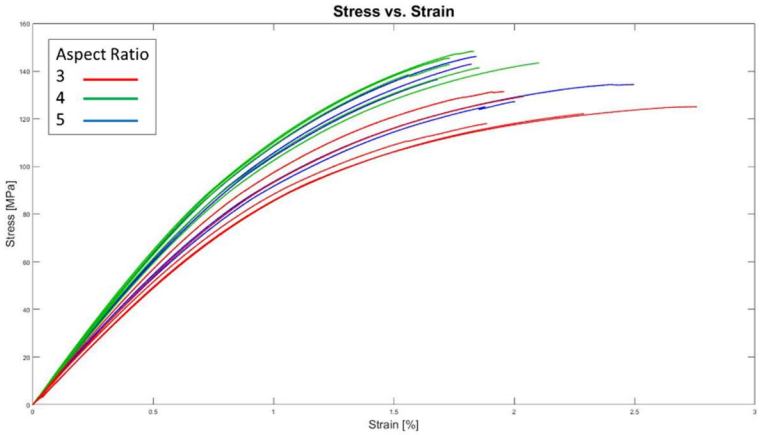

Figure 2.9: Stress-strain curves as a function of aspect ratio for the first five of seven tested samples.

A three-bead vertical wall was printed with the CAMRI system for each aspect ratio. The three aspect ratio walls were completed in a single print as shown in Figure 2.10. The sample preparation step is slightly different from the LSAM tensile samples. As shown in Figure 2.11 the two outer beads, one from each side were removed with a wood planer. Leaving only the middle bead for tensile specimen extraction.

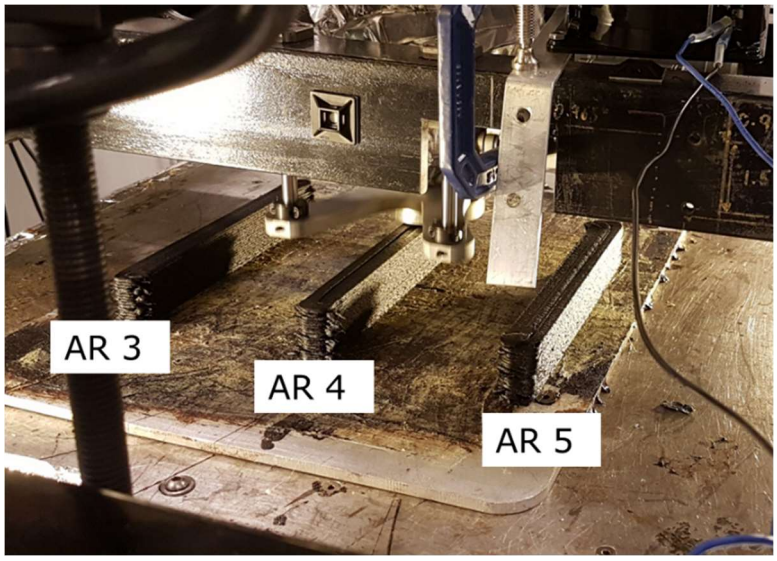

Figure 2.10: Printing of walls with three different aspect ratios in the CAMRI system.

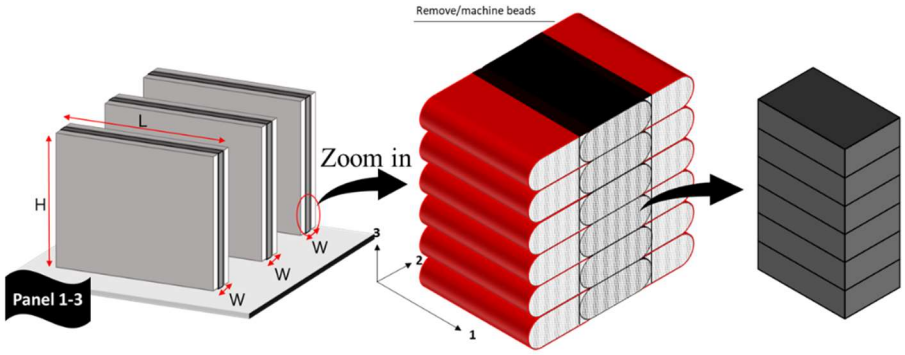

Figure 2.11: Extraction of single-bead wall from a vertical wall printed with three beads across the width.

A mechanical test system (MTS) load frame with 22-kip capacity was used for load transfer. The full-filed strain field was acquired from the Digital Image Correlation (DIC) system. A more detail procedure is discussed in section 2.2.3 Elastic Properties. shows the stress vs strain plot of the CAMRI- AR 3, CAMRI- AR 4 and CAMRI- AR 5. Table 2.6 shows the average tensile modulus (E_1) and the average ultimate strength of all the aspect ratio.

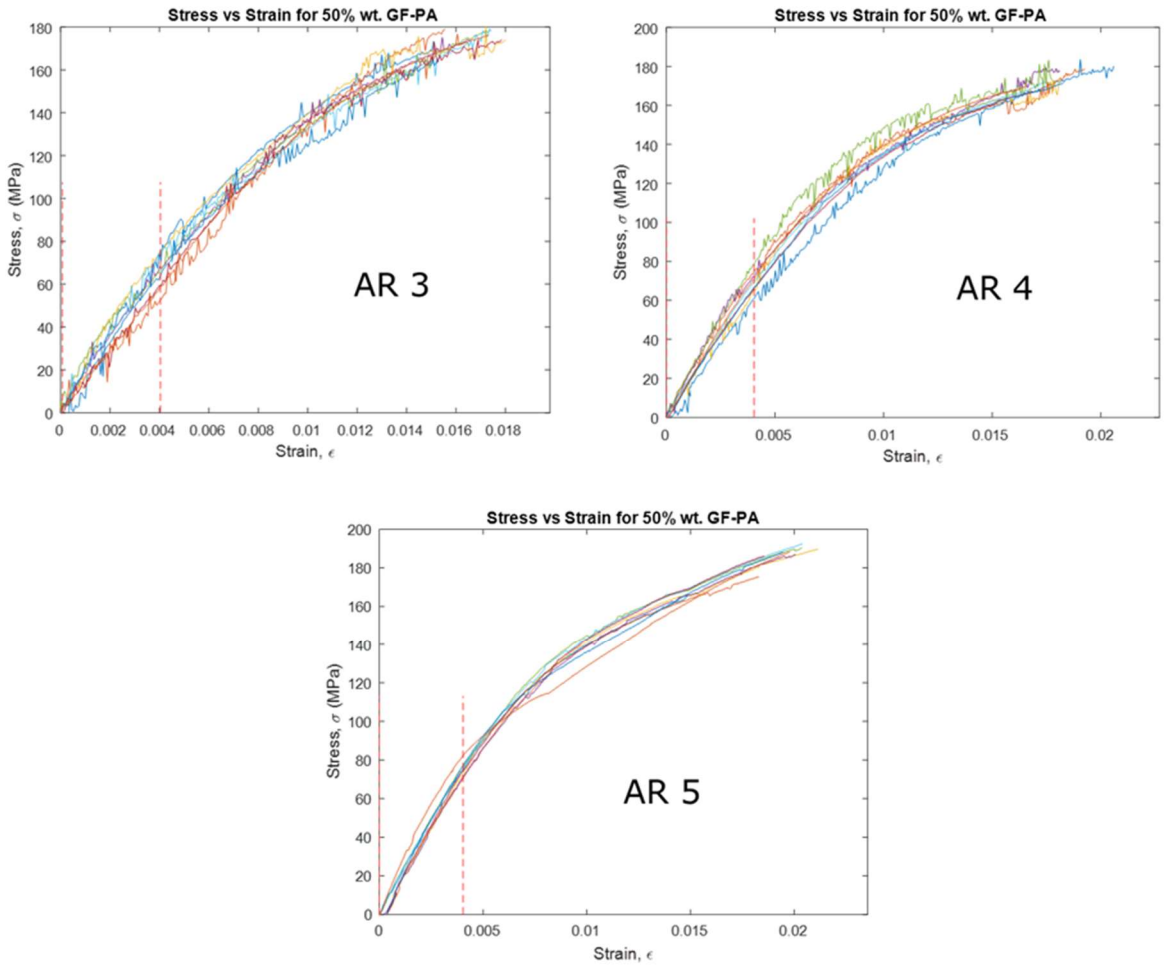

Figure 2.12: Stress vs strain plot of the tensile test in 1-direction of CAMRI- AR 3, CAMRI- AR 4 and CAMRI- AR 5.

Table 2.6: Tensile modulus in 1-direction of CAMRI- AR 3, CAMRI- AR 4 and CAMRI- AR 5.

CAMRI	Avg E1 (GPa)	SD	Avg Ult. Strength (MPa)	SD
AR 3	16.10	2.30	175.74	4.68
AR 4	17.43	1.17	175.94	6.37
AR 5	19.50	0.82	184.81	8.70

2.1.3. Interlayer Fracture Toughness

The double cantilever beam (DCB) test for mode-I fracture testing in this section followed the recommendation of ASTM D5528. The purpose of the test is to determine the opening mode interlaminar fracture toughness G_{IC} of additive manufactured prints with different processing conditions namely different aspect ratio. Moreover, the first milestone 7.7.2.1 requires the

measured mode-I interlayer fracture energy to be at least 75% of the fracture energy measured from heat-treated printed samples to achieve maximum strength through crystallization and enhanced polymer diffusion. The reference mode-I interlayer fracture energy was measured from samples with bead aspect ratio of 3 which were heat-treated at 170°C for 2 hours.

First, DCB specimens were printed with different processing conditions, namely varying aspect ratio as mentioned at the beginning of section 2.1: Printability Assessment. The specimens were obtained from the same one bead wall printed for the tensile specimen in the previous section. While the print reached 4th layer from the last layer, Polyimide or Teflon film was placed on the two longer walls of the geometry as shown in Figure 2.13. The tape/film are approximately 25 mm long and approximately 150 mm apart. Next, each specimen was extracted from the region shown in Figure 2.13 using the cold saw. The length of every DCB specimen is 177.8 mm (7 in) long. The height and the width depend on the aspect ratios which are recorded in the Appendix section.

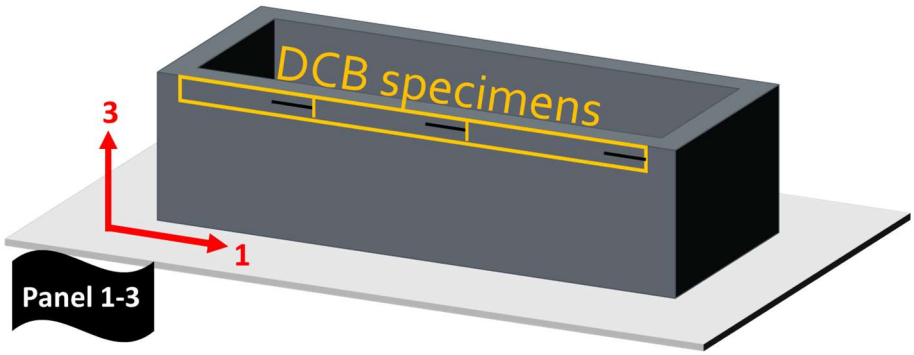

Figure 2.13: Illustration of the location where the DCB specimens were extracted.

Figure 2.14 shows the steps to prepare DSC specimens. First, each side of the specimen was machined until flat with the CNC. Then, two 25.4 mm (1 in) wide steel piano hinges were glued and screwed to each side of the specimen as shown in the bottom left of Figure 2.14. The screw used in this case should not be longer than two bead height, therefore should not reach the initial crack. Lastly, a very thin white spray paint was sprayed on one side of the specimen, along with a speckle pattern for the DIC purposes as also shown in Figure 2.14. In addition to the procedure described, the AR 3 specimens were heat treated at 170 °C for 2 hours before CNC machining. The interlayer fracture energy of AR 3 samples was used as a reference of a sample with maximum strength through crystallization and enhanced polymer diffusion to justify milestone 7.7.2.1.

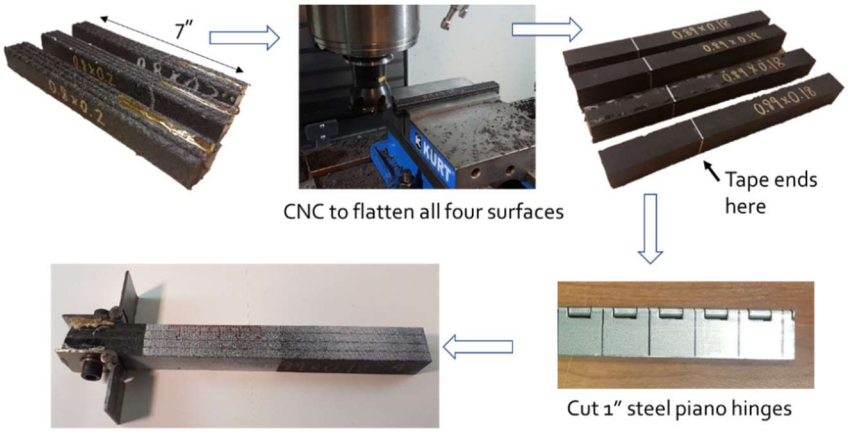

Figure 2.14: DCB specimen preparation.

Testing of the DCBs was conducted in a universal testing machine MTS-810 equipped with a 5 KN load cell and under fixed grip conditions to attain stable crack propagation. Per recommendation of the ASTM-D5528 standard, a loading rate of 2 mm/min was used for opening the DCB whereas an unloading rate of 10 mm/min was used for closing the DCB. Figure 2.15 shows the setup used in the DCB fracture tested performed in the universal testing machine. Load and displacement were recorded during both loading and unloading at a rate of 10 Hz.

A traveling optical microscope (Leica S6D) equipped with a camera (PixeLINK Model PL-B776) was employed to monitor the extension of the crack tip during the fracture test. Frames were recorded at intervals of 0.75 s and throughout the entire fracture test. In order to track the location of the crack tip, a millimetric scale was drawn at the edge of the DCB in red color. This way, the frames recorded with the traveling microscope can be used to track the evolution of the crack tip during the fracture test. In order to obtain multiple measurements from a single specimen, three loading cycles were performed after extending the crack for about 15 mm in each loading cycle. Three crack extensions were estimated using the frames recorded during the fracture test of the DCB including the visual onset of crack extension.

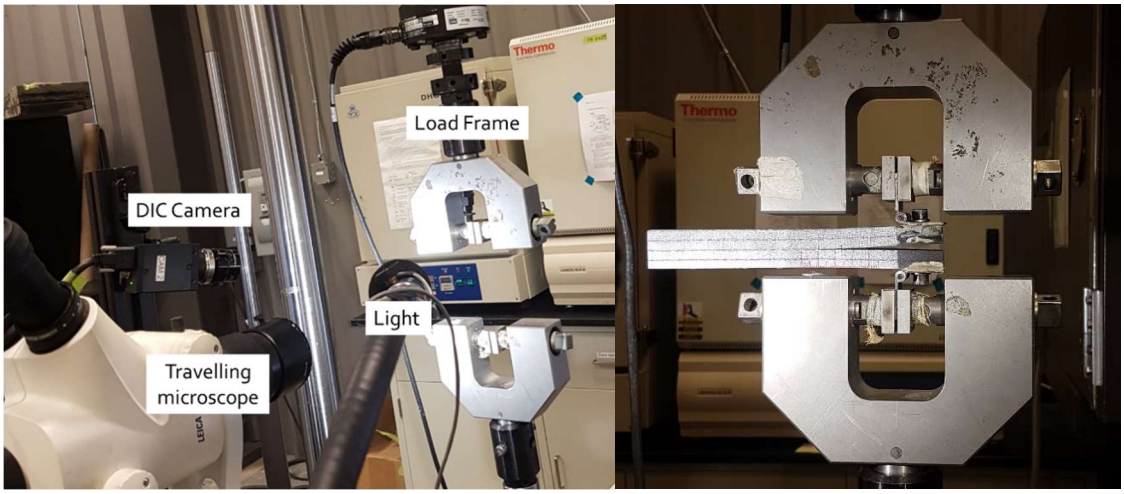

Figure 2.15: Setup used for testing DCB specimens in Universal Testing Machine.

Three methods were utilized to compute the energy release rate G_I from the DCB fracture test, namely the Compliance Calibration (CC) method, the Modified Beam Theory (MBT) method and the Modified Compliance Calibration (MCC) method [9], [10]. The approach that yielded the most conservative values of critical energy release rate G_{IC} was adopted at the end. Utilizing the load P and the displacement at the load point δ recorded during the fracture test, the energy release rate G_I can be estimated with the CC method as given by Equation 2.1

$$G_1 = \frac{nP\delta}{2ba} \tag{2.1}$$

where n is a calibration parameter obtained by fitting a straight line in a double logarithm plot of the inverse of the compliance, C, versus the crack length. Compliance is defined as $C=\delta/P$. Additionally, b is the width of the sample and a is the crack length. The second approach used to compute G_{1c} was the MBT method given by Equation 2.2

$$G_1 = \frac{3P\delta}{2b(a + |\Delta|)} \tag{2.2}$$

The parameter Δ can be obtained experimentally by generating a least squares plot of the cube root of the compliance, $C_{1/3}$, as a function of the crack length, a. The distance from the origin to the intercept of the least squares plot with the origin determines the correction parameter Δ. MCC was the last method utilized in the calculation of G_{1C} and it is given by Equation 2.3.

$$G_1 = \frac{3P^2C^{2/3}}{2A^1bh} \tag{2.3}$$

The parameter A_1 used in the MCC approach is determined by creating a plot of the crack length normalized by the thickness of the DCB, a/h, as a function of the cube root of the compliance, $C_{1/3}$. The slope of the line fitted along the experimental data points corresponds to A'.

Three loading cycles were performed wherein the crack tip was extended by about 15 mm in each cycle. However, only the data obtained from the last loading cycle was used for the analysis

because the first two loading cycles were affected by the yielding of the piano hinges used for load introduction. Figure 2.16 shows the load-displacement curve of the third cycle of the AR 3 sample 1 (AR3-1).

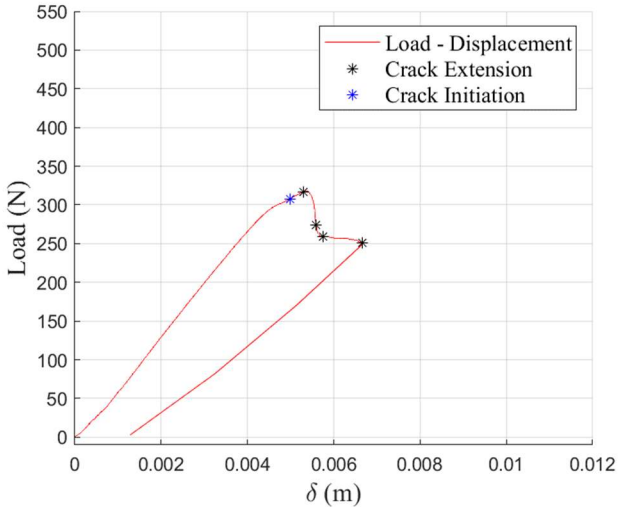

Figure 2.16: Load-displacement curve of the last loading cycles (Specimen AR3-1).

Calculating G_{IC} with the MBT method requires the determination of the parameter Δ. The top left of Figure 2.17 shows the plot of the cubic root of the compliance to the crack length used in the determination of the parameter Δ. In order to utilize the CC method to determine G_{1C} at the points of crack initiation and extension, the parameter n was determined from the slope of the line shown in the top right corner of Figure 2.17. Now to estimate G_{IC} using the MCC method, the parameter A_1 was determined from the slope of the linear fit shown in bottom left of Figure 2.17. After determining the coefficients required for estimating G_{IC} using the aforementioned methods, a delamination resistance curve that shows G_{IC} as a function of the crack length was generated to verify the independence of G_{IC} with the crack length. Figure 2.17 bottom right shows the delamination resistance curve created with the G_{IC} estimated with each of the three methods.

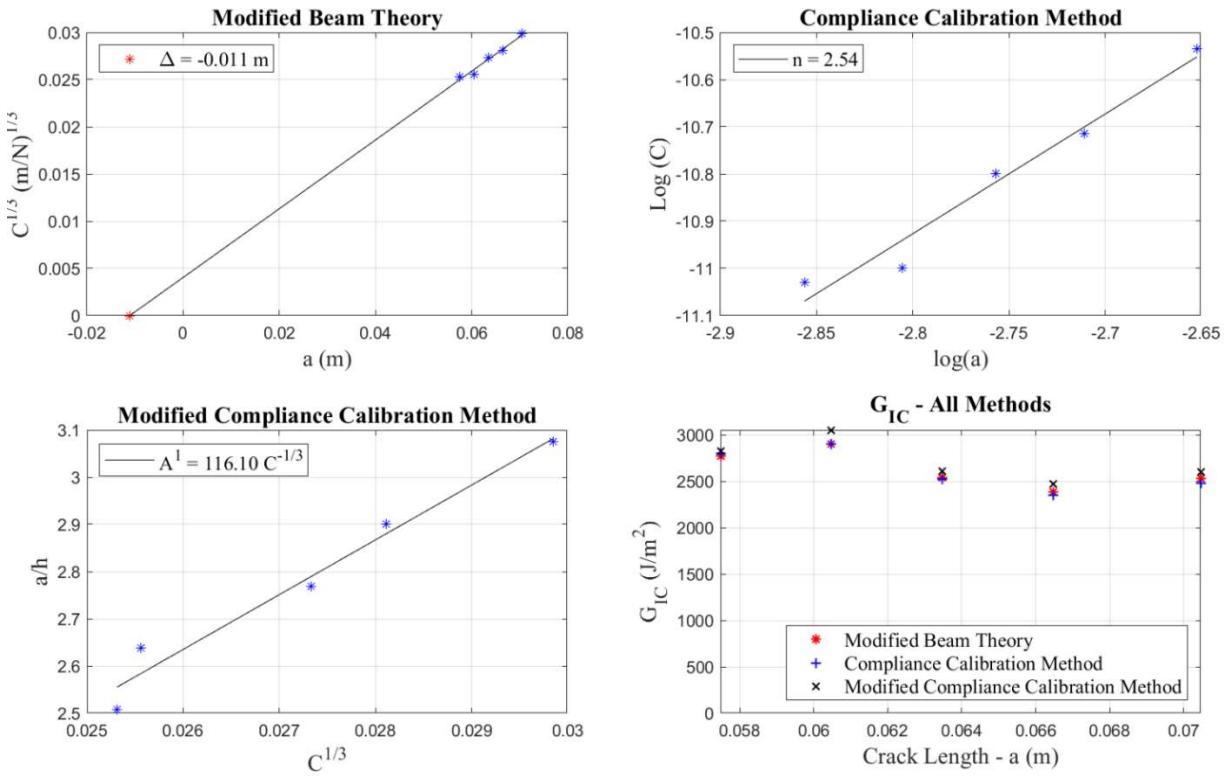

Figure 2.17: Determination of parameters in MBT, CC, and MCC method.

For all the specimens tested, the CC method yielded the most conservative mean values of G_{IC}. Therefore, the estimates of G_{IC} obtained with this method were used. Values for the mean and the standard deviation of the experimentally determined G_{IC} were computed for each of the conditions investigated and considering the results of all the specimens tested as shown in Table 2.7. The average G_{IC} of AR 5 is 79% of the AR 3 which were heat treated and well bonded. Milestone 7.7.2.1 requires the measured interlayer fracture energy to be at least 75% of the fracture energy of fully bonded layer. Therefore, the G_{IC} of AR 5 exceed the goal of 75 % of the heat treated, maximum crystallized G_{IC}. The average G_{IC} of AR 4 is 73 % of the AR 3 which almost achieved the goal of Milestone 7.7.2.1.

Table 2.7: Summary of G_{IC} characterized from each set of aspect ratio.

Sample	Mean G_{IC} (J/m^2)	SD G_{IC} (J/m^2)	Average G_{IC} (J/m^2)	SD G_{IC} (J/m^2)
AR 3 - 1	2661	231	2536	842.78
AR 3 - 2	3670	128		
AR 3 - 3	2038	157		
AR 3 - 4	1774	67		
AR 4 - 1	1966	71	1839	399.31
AR 4 - 2	1384	133		
AR 4 - 3	2320	68		

AR 4 - 4	1684	79		
AR 5 - 1	2346	107	1997	441.63
AR 5 - 2	1571	161		
AR 5 - 3	2409	216		
AR 5 - 4	1662	62		

2.2. Experimental Characterization Of Additively Manufactured Fiber Reinforced Thermoplastic

An extensive material characterization program was conducted in this project to determine temperature-dependent material properties required for simulating the EDAM process. ADDITIVE3D© [11], [12], a physics-based simulation framework, was used for simulating the EDAM process in this program. The EDAM process involves the scales illustrated in Figure 2.18. The smallest scale depicted in Figure 2.18 is at the level of the microstructure resulting from the deposition process, matrix and fibers with different orientations within the printed bead. The second length scale depicted in Figure 2.18 is the bead level and involves homogenization of the material properties at the level of the bead. The following length scale is the printed mesostructure which consist of multiple beads.Finally, the largest scale, is the printed component which may comprise of regions with different printed mesostructuresThe EDAM process simulation is captured at the length scale of the printed bead and therefore requires effective properties of the printed material homogenized at the same length scale. This way, effects of different printing patterns and geometries are captured in the simulation of the EDAM process performed with ADDITIVE3D©.

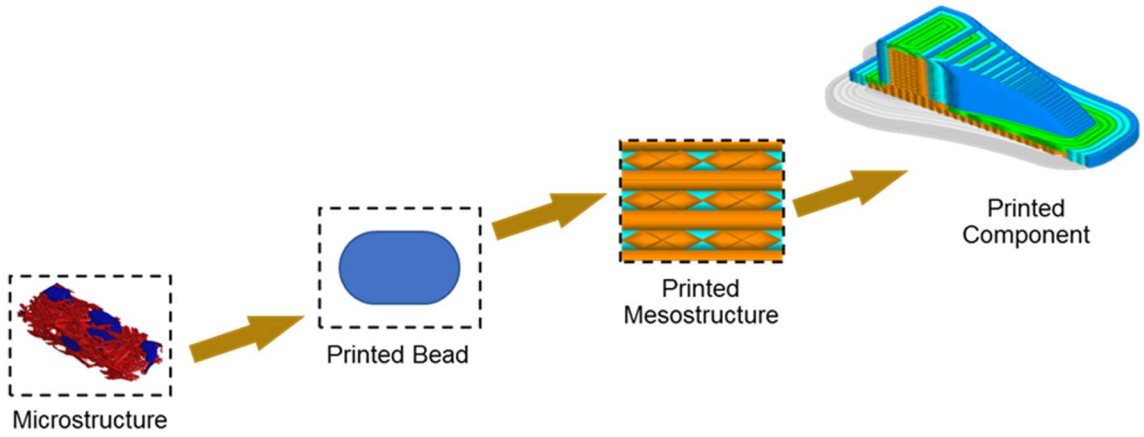

Figure 2.18: Scales in the EDAM process.

2.2.1. Specimen Preparation

The material characterization was carried out with the panels printed with a bead aspect ratio of 4 and bead dimensions of 17.78 mm wide and 5.84 mm tall (0.8” x 0.2), which is the condition used predominantly in the LSAM system. The goal is to characterize mechanical, thermomechanical, thermoviscoelastic, and thermophysical properties in all three-principal direction. Given that the

GF-PA is a semi-crystalline polymer, the melting and crystallization kinetics also need to be characterized. To perform the characterization that is dependent on the bead orientation, two types of panels were printed. Panels for characterizing properties in the 1-3 plane were extracted from hollow rectangles printed with one bead walls, whereas panels for characterizing properties in the 1-2 plane were extracted from rectangular panels printed horizontally on the build plate. The experimental characterization of the printed material was performed with panels printed in both the LSAM and the CAMRI system. Table 2.8 summarizes the AM system used for characterizing each of the material properties required for simulating the printing process. Properties labeled as system independent indicated that are not dependent on the fiber orientation distribution within the printed bead. The motivation for utilizing specimens printed in the CAMRI system was primary to accommodate the microstructure of an entire bead in the specimens used in the experimental characterization of the material. Following the experimental characterization, a virtual characterization step was carried out to predict the effective properties of the beads printed in the LSAM. Further details on the virtual characterization are provided in the section 2.2.4.2.

Table 2.8: Summary of AM system used for characterizing each of the material properties.

Property	AM system used for specimen preparation
Microstructure	
Fiber orientation	LSAM, CAMRI
Fiber length	LSAM
Elastic	
Tensile 1-Direction	LSAM, CAMRI
Tensile 2-Direction	LSAM
Tensile 3-Direction	LSAM
Shear 1-2 Plane	LSAM
Thermomechanical	
Glass transition temperature	System Independent
Coefficient of thermal expansion	CAMRI
Melting and Crystallization Kinetics	System Independent
Thermophysical	
Heat capacity	System Independent
Thermal conductivity	LSAM
Thermoviscoelastic	CAMRI

Figure 2.19 illustrates the preparation process of the panel in the 1-3 plane. First, a one bead vertical panel was printed with the LSAM system at Local Motors. The width of the printed bead and therefore the width of the single-bead walls is 20.32 mm (0.8”). Similarly, the walls are 25 beads in height which corresponds to around 127 mm (5”). Notice that the side of the wall is not smooth due to the curvature of the bead. Once the wall cooled to room temperature, the surface of the panels was machined for removing the scalloped surface. A wood planer equipped with carbide tips was used for machining the panels. By removing equal amounts of material from each side, a

12 mm wide panel was obtained. Additionally, the two bottom most layers of the wall were discarded.

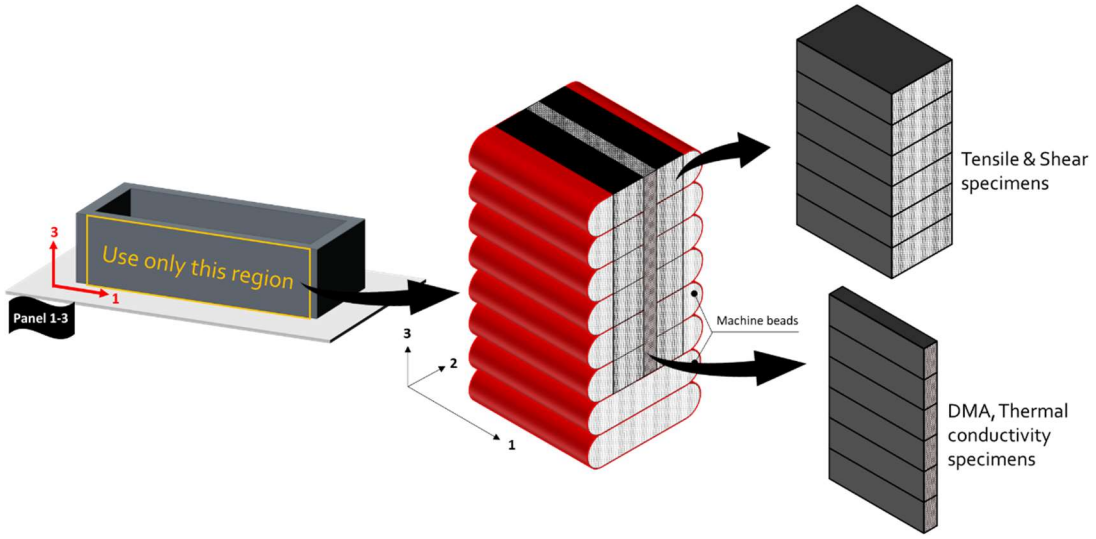

Figure 2.19: Steps for preparing panels in the 1-3 plane.

The preparation process of the panels in the 1-2 plane starts with printing a horizontal panel with five layers in the stacking direction. The height of one layer is 0.2 in (5.08 mm) which makes the height of the panel approximately 25.4 mm. Then, using the wood planar, two layers from the bottom and one layer from the top were removed. The final height of the part is approximately 10 mm. Figure 2.20 shows the steps followed for preparing panels for characterizing the material properties in the 1-2 plane.

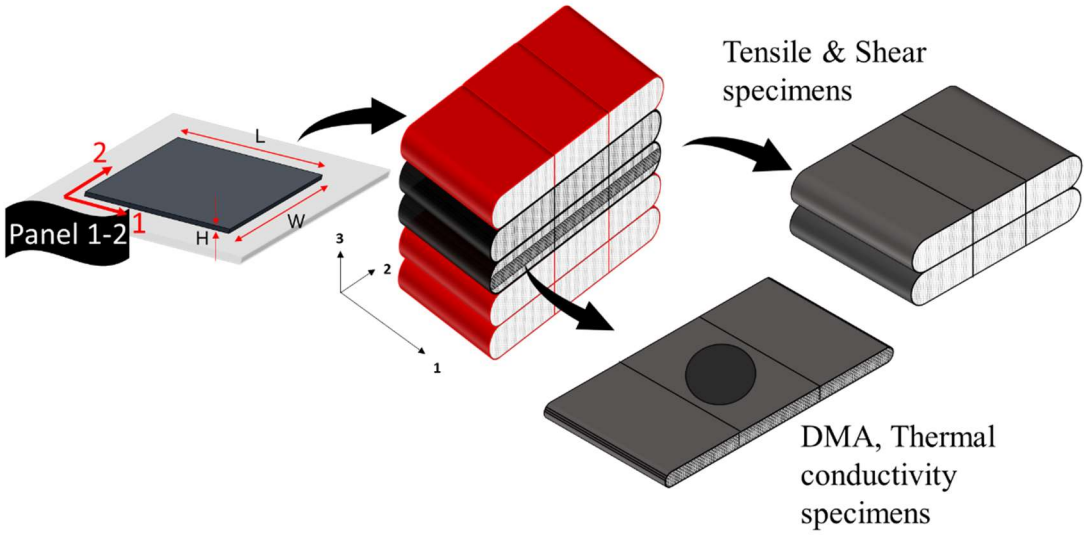

Figure 2.20: Steps for preparing panels in the 1-2 plane.

2.2.2. Microstructure of Printed Material

Most properties characterized in this program are dependent on the microstructure of the printed bead, namely fiber length distribution, fiber orientation distribution, and void content. For example, the coefficient of thermal expansion (CTE) and the elastic properties are strongly dependent on the fiber orientation distribution [13].

The GF-PA used in this program is made through a compounding process that yields a composite material with relatively short average fiber length. Furthermore, additional attrition of the fibers can occur during the melting process of the pellets in the single-screw extrusion process [14]. Therefore, the distribution of fiber lengths was characterized for material processed in the LSAM system.

To isolate fibers from the matrix, a small section of the LSAM printed part with AR of 4 was burnt off in a small furnace. The samples were heated to 700°C and kept in the furnace for a total of two hours before turning off the furnace. This process burnt off the polyamide in the composite, leaving the glass fibers accompanied with some residues. Figure 2.21 shows the printed material before and after matrix burnt off. The LSAM printed GF-PA is indicated by the red circle.

Figure 2.21: Printed GF-PA before and after burning off the matrix.

Following the burn off of the matrix, the white glass fiber was transferred in to a microscope glass slide and dispersed with silicone oil. A thin microscope cover glass was placed on top of the fiber which also helps further dispersed the fibers. A mosaic of images was captured with a LEICA DMI 5000 M optical microscope. The image constructed with the mosaic of images was then used for measuring the length of the fibers. Figure 2.22 shows a section of the image used for measuring fibers. The software ImageJ [15] was utilized for manually measuring 1000 fibers. To measure the fiber length, line segments were drawn manually for each fiber ignoring fragments and residues such as the one highlighted Figure 2.22.

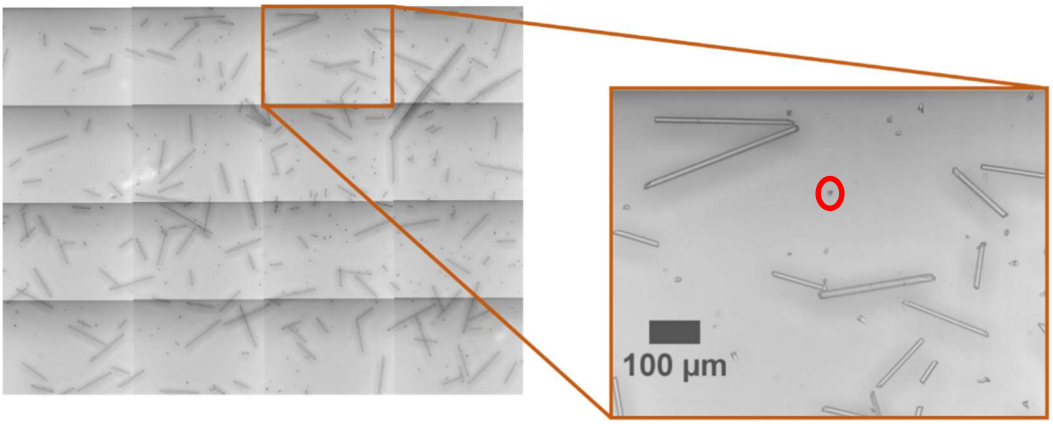

Figure 2.22: Fibers dispersed on a glass slide.

A histogram was constructed with the 1000 measurements to display the distribution of fiber length (Figure 2.2 5). While the longest fiber measured was 638.83 µm, the shortest fiber measured was 22.09 µm. There are two method of averaging fiber length, the number average and the weighted average. The number average method, L_n, can be computed using the equation below, where n_i is the number of fibers of length L_i. Number average is the common way to determine the average quantity of interest.

$$L_n = \frac{\sum_i n_i L_i}{\sum_i n_i}$$

On the other hand, the weighted average method,L_w, is better capture the presence of longer fibers as it is believed to influence the mechanical properties more than the short fibers [16]. Weight

average fiber length can be calculated using equation below

$$L_w = \frac{\sum_i n_i L_i^2}{\sum_i n_i L_i}$$

The number average fiber length computed is 205.83 μm and the weight average fiber length computed is 272.41 μm. The weighted average fiber length is used in the micromechanics virtual characterization and reverse engineering in later section.

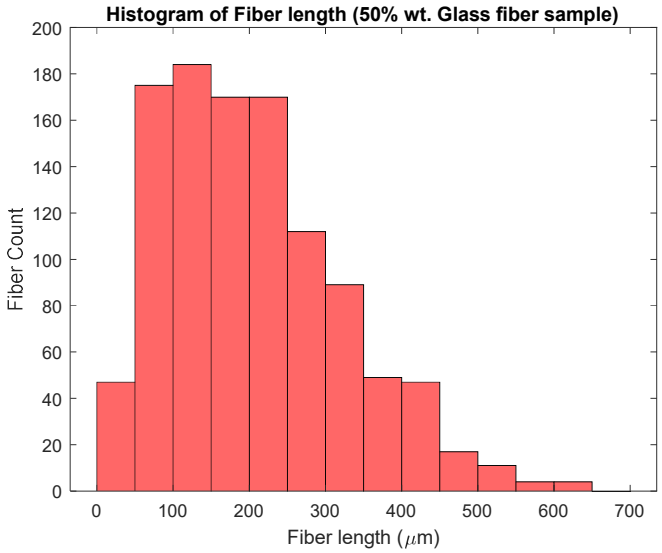

Figure 2.23: Fiber length distribution of material printed in the LSAM.

As mentioned in the section 2.1.1 Effects of Deposition Conditions on Fiber Orientation Distribution, the fiber orientation was obtained by using micro-Computerized Tomography (CT) technique scan-generated three-dimensional image of fibers. The microCT scans, then were broken into finite rectangular sections. The area weighted average fiber orientation tensor in the three-principle direction were calculated. For the mechanical testing purpose, the outer part of the bead or the curvature part of the bead was removed by a wood planar. Thus, another step was completed to calculate the area weighted average fiber orientation of the machined bead. A detailed procedure was discussed in section 2.1.1. A11 is the orientation tensor in the 1 direction which is the print direction. Because the bead shows the bead cross sectional area, 1 direction is the direction pointing out of the page. A22 is the orientation tensor along the transverse direction which is to the left and right of the page. A33 is the orientation tensor along the stacking direction pointing up. The fiber orientation Tensor A_{ij} of the whole bead and planed bead is summarized in Table 2.9.

Table 2.9: Summary of the number average, area weighted average fiber orientation Tensor A_{ij} of LSAM- AR4 whole bead and planed bead.

Sample	Number Average Whole Bead	Area Weighted Whole bead	Planed bead
LSAM – AR 4	$A_{ij} = \begin{bmatrix} 0.58 & 0 & 0 \\ 0 & 0.32 & 0 \\ 0 & 0 & 0.10 \end{bmatrix}$	$A_{ij} = \begin{bmatrix} 0.57 & 0 & 0 \\ 0 & 0.34 & 0 \\ 0 & 0 & 0.09 \end{bmatrix}$	$A_{ij} = \begin{bmatrix} 0.53 & 0 & 0 \\ 0 & 0.39 & 0 \\ 0 & 0 & 0.08 \end{bmatrix}$

2.2.3. Elastic Properties

To characterize an orthotropic material, 9 constants are required to complete the compliance or stiffness matrix. The constants are reduced from 21 to 9 due to the three mutually orthogonal planes of symmetry. Those constants are E1, E2, E3, G12, G13, G23, v12, v13, and v23 as shown in the compliance matrix used in Equation 2.4. Some of which can be calculated by the relationship of ν21/E2 = ν12/E1, ν31/E3 = ν13/E1, ν32/E3 = ν23/E2.

$$\begin{Bmatrix} \varepsilon_{11} \\ \varepsilon_{22} \\ \varepsilon_{33} \\ 2\varepsilon_{23} \\ 2\varepsilon_{13} \\ 2\varepsilon_{12} \end{Bmatrix} = \begin{bmatrix} \frac{1}{E_1} & -\frac{v_{21}}{E_2} & -\frac{v_{31}}{E_3} & 0 & 0 & 0 \\ -\frac{v_{12}}{E_1} & \frac{1}{E_2} & -\frac{v_{23}}{E_3} & 0 & 0 & 0 \\ -\frac{v_{13}}{E_1} & -\frac{v_{23}}{E_2} & \frac{1}{E_3} & 0 & 0 & 0 \\ 0 & 0 & 0 & \frac{1}{G_{23}} & 0 & 0 \\ 0 & 0 & 0 & 0 & \frac{1}{G_{13}} & 0 \\ 0 & 0 & 0 & 0 & 0 & \frac{1}{G_{12}} \end{bmatrix} \begin{Bmatrix} \sigma_{11} \\ \sigma_{22} \\ \sigma_{33} \\ \sigma_{23} \\ \sigma_{13} \\ \sigma_{12} \end{Bmatrix} \quad (2.4)$$

However, in this study only E1, E2, E3, G13, and v13 were physically measured. The other properties were obtained via micromechanics. Tensile test, and shear (Iosipescu) test procedures and results will be discussed.

2.2.4. Tensile Properties

The sample preparation includes printing, machining, heat treating, water jetting, drying, and applying speckle patterns. Printing and machining were covered in the subsection 2.2.1. All the panels were heat treated at 170 °C for two hours in a forced convection oven. This step is required

to achieve the maximum possible crystallinity in the material and to relieve thermal stresses developed during the printing process of the panels. Following the waterjet cut, the specimens were dried in an industrial material dryer for 12 hours at 50 °C to remove the moisture from the specimens. Note that specimens were extracted from panels instead of being printed to their final shape with no post-machining operations because the goal is to characterize the tensile properties of the material, not the properties of the mesostructure of the printed shear structure. The tensile test in the print direction and data reduction was performed at DuPont and the test in the transverse and stacking direction were performed at Purdue University. The first set of tensile properties reported corresponds to the 1-direction. Please refer to the section 2.1.2 for the detail of the test and results. The dimension of the tensile coupons in the 1 direction in the 1-3 plane can be found in Figure 5.1 of the APPENDIX.

The specimen in the 2-direction or the transverse direction is simpler to extract than the 1-direction specimen. The gage length of the specimen is approximately 60 mm and the bead width is 20.32 mm. Therefore, there are 3 beads in the gage section. Dimensions of the 2-direction tensile specimen can be found in Figure 5.2 in the APPENDIX. The specimen in the 3 direction or the stacking direction has a gage length of the specimen of approximately 48 mm and the bead height is 5.08 mm. Therefore, there are approximately 9 layers in the gage section. Dimensions of the 2-direction tensile specimen can also be found in Figure 5.3 in the APPENDIX.

The tensile test in the print direction and data reduction was performed at DuPont. The details can be found in the section 2.1.2. Table 2.10 shows the modulus and ultimate strength measured for each sample.

Table 2.10: Modulus of Elasticity of Print Direction Specimens.

Sample	$\boldsymbol{E_x}$ **(GPa)**	$\boldsymbol{X_X^T}$ $\boldsymbol{(MPa)}$
1	13.23	142.9
2	13.50	145.6
3	12.88	141.6
4	12.55	143.5
5	13.65	148.5
Average	13.16	144.4
SD	0.45	2.70
Variance	0.16	5.83

The transverse and stacking direction were tested at Purdue University. In terms of specimen preparation, all specimens were painted at the gage section with three thin coats of white enamel painting with 15-minute interval between each coat. Black speckle dots were stochastically deposited onto the gage section by a 0.007" (0.18 mm) dot size roller after the paint had dried overnight.

A mechanical test system (MTS) load frame with 22-kip capacity was used for load transfer. The full-field strain field was acquired from the Digital Image Correlation (DIC) system which includes light sources and two 5-megapixel cameras one looking down to the specimen from the top and

one looking up from bottom which simultaneously capturing images as shown in Figure 2.24. Due to the heterogeneous nature of the composite, it is expected to have some non-uniformity in the strain field. 11 specimens were tested and fractured specimens are shown in Figure 2.25.

Figure 2.24: Tensile Test Setup.

Every sample failed laterally with some of the fracture failing at the grip and some failing in the gage section. According to ASTM 3039 [17], the failure code of the samples are LAT- lateral failure at the grip region located at the top, LGM – lateral failure at the gage section in the middle, and Sample #3 failed LIT – lateral inside grip/tab region at the top.

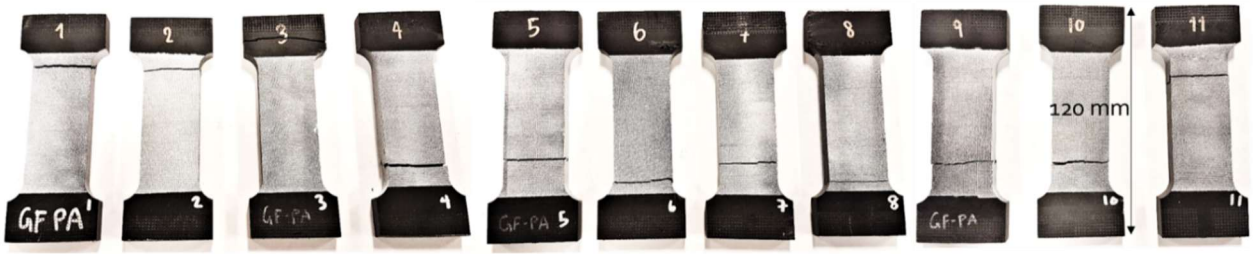

Figure 2.25: Fractured transverse direction tensile specimens.

The strain snapshot of the transverse direction is shown in *Figure 2.26*. There are some 'hot spots' shown in the strain field which corresponds to the interface region because there is no fiber crossing the adjacent bead interface. The only contribution to strength in the interface region is the matrix which is more compliant than the region within the beads.

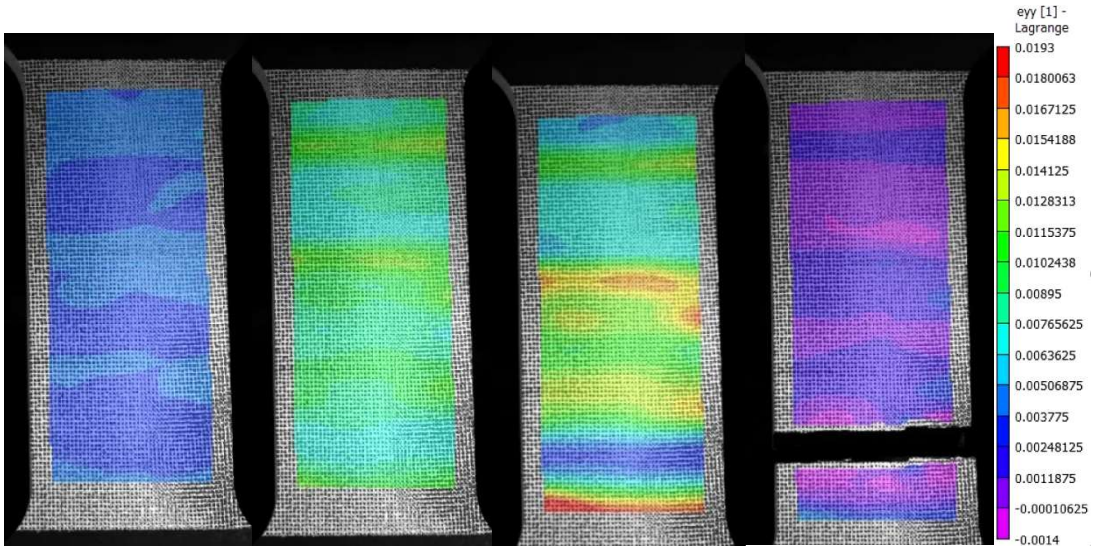

Figure 2.26: Strain field of tensile coupons in the transverse direction.

Figure 2.27 is the stress vs strain plot of every sample. There is some variation among samples in both modulus and strength. Table 2.11 shows the modulus and ultimate strength measured for each sample.

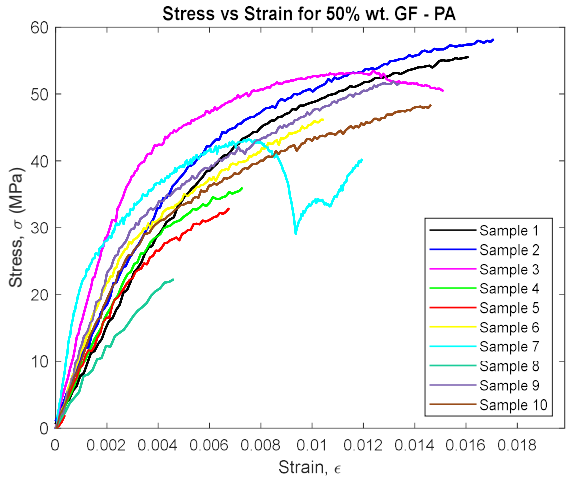

Figure 2.27: Stress-strain plots of transverse direction specimens.

Table 2.11: Modulus of elasticity of transverse direction specimens.

Sample	E_2 (GPa)	Ultimate Strength (Mpa)
1	7.35	55.59
2	7.93	58.20
3	10.81	53.55
4	7.45	35.98

5	6.85	32.89
6	8.18	46.21
7	5.32	43.22
8	5.33	22.26
9	8.91	51.92
10	8.07	49.17
11	5.52	48.38
AVG	7.43	45.22
STDEV	1.66	10.89
VAR	2.77	118.54

Regarding the tensile test in the stacking direction, ten specimens were tested and the fractured specimens are shown in Figure 2.28. Every sample had Lateral failure type with some of the fracture failed at the grip some failed in the gage section. According to ASTM 3039 [17] failure code, is LAT- lateral failure at the grip region located at the top, and LGM – lateral failure at the gage section in the middle.

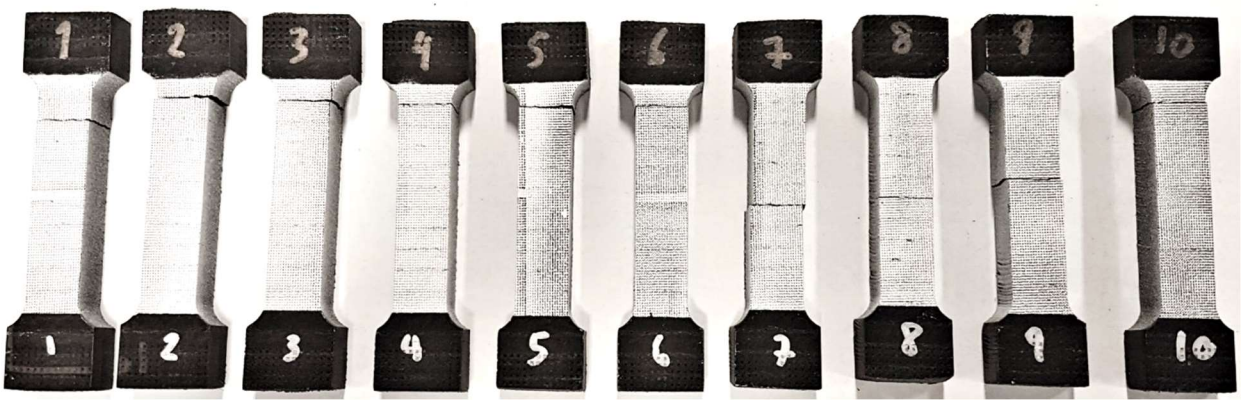

Figure 2.28: Fractured stacking direction tensile specimens.

The strain snapshot of the transverse direction is shown in *Figure 2.29*. The hotspots of the specimens correspond to the interface region between layers which is more compliant than the rest because it is governed by only the matrix properties. *Figure 2.30* is the stress vs strain plot of every sample.

Table 2.12 shows the modulus and ultimate strength measured for each sample.

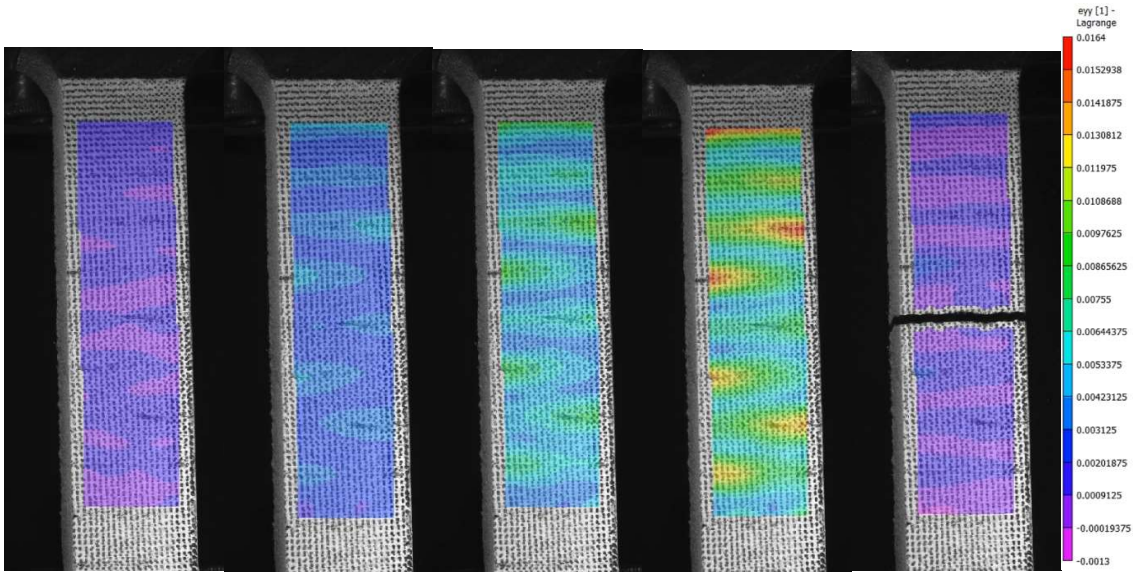

Figure 2.29: Strain field of tensile coupons in the stacking direction

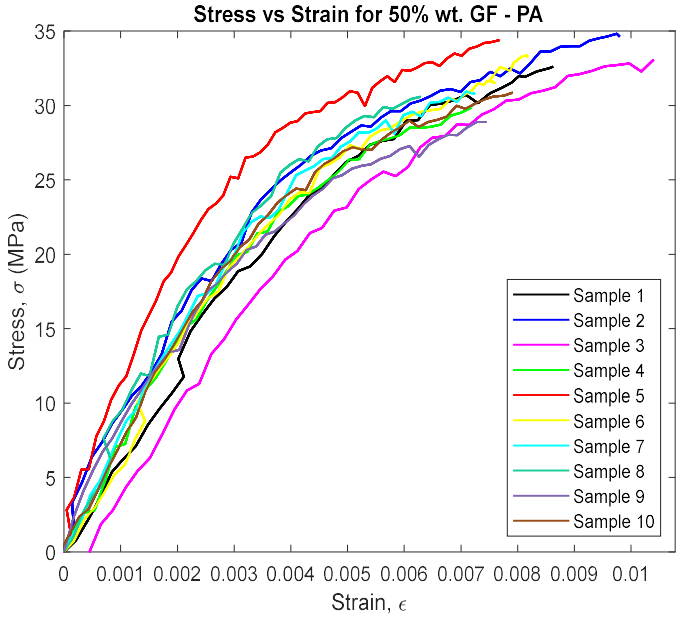

Figure 2.30: Stress-strain plots of stacking direction specimens

Table 2.12: Modulus of elasticity of specimens in stacking (3) direction

Sample	Modulus of Elasticity (Gpa)	Ultimate Strength (Mpa)
1	6.73	32.64
2	5.63	34.84
3	5.87	33.60
4	5.98	31.69
5	6.66	34.51
6	6.47	33.37
7	5.92	31.68
8	5.64	30.76
9	5.30	29.93
10	6.23	30.97
AVG	6.04	32.40
STDEV	0.47	1.66
Var	0.22	2.74

2.2.4.1. Shear Properties

The orientation investigated was on edge (1-3 plane). The test in the 1-3 direction characterizes shear modulus and strength, shear properties describing the response resulting from a shear force or deformation applied to the 1-3 material planes. The shear specimen geometry followed specifications outlined in ASTM D-5379 [18] which are illustrated in Figure 2.31. The sample preparation steps are identical to tensile specimens' preparation, except the specimen's geometry. As mentioned earlier the bead width of the printed wall is 0.8" (20.32 mm), therefore the width of the wall is approximately 20.32 mm. In this experiment, the side of the wall was smoothened using the wood planar and the center region of the bead results in a width of 12 mm. The two bottom most layers of the wall were also discarded.

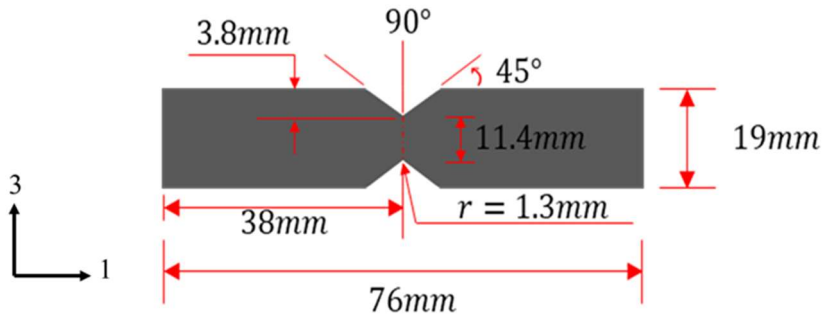

Figure 2.31: Dimension of a shear coupon.

There are two types of shear specimen alignment with respect to the bead as shown in Figure 2.32. Group A) consists of four layers total having two full layers between the notches and two almost

full layers on the edges. Group B) consists of three full layers total, and two partial layers on the top and bottom. Between the notches, there is one full bead and two partial beads. Since the geometry of the Iosipescu fixture is fixed, there is no variation of the specimen geometry for this specific bead dimension. The samples were dried with the tensile specimens. Note that specimens were extracted from panels instead of being printed to their final shape with no post-machining operations because the goal is to characterize the shear properties of the material, not the properties of the mesostructure of the printed shear structure.

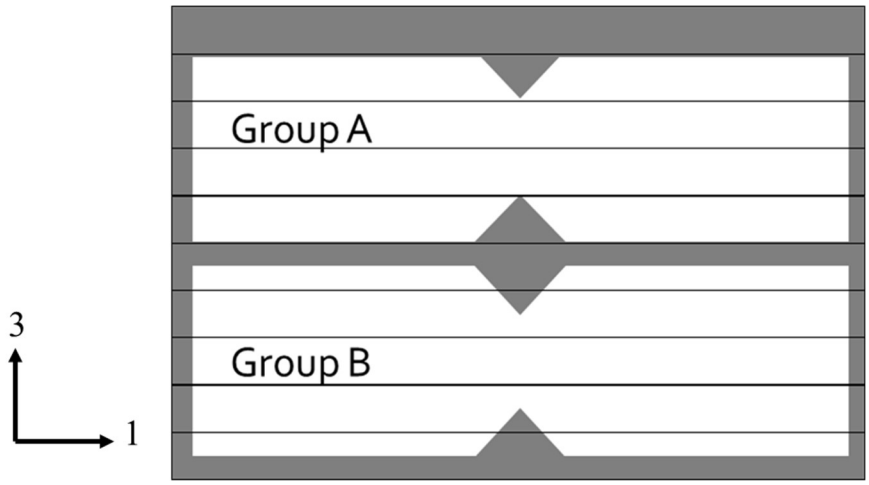

Figure 2.32: Group A) and Group B) specimen alignment with respect to the bead height.

Identically to tensile specimens preparation, once the shear specimens have been appropriately dried, they were sprayed paint with three thin coats of white enamel paint to the region around the notch, then a speckle pattern was applied. Figure 2.33 shows a specimen with a speckle pattern.

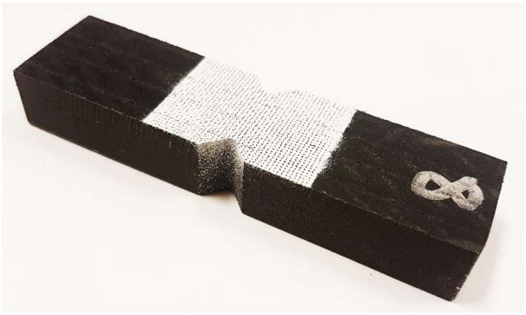

Figure 2.33: Shear specimen with speckle pattern.

The experiment was performed using the MTS universal testing machine equipped with a 5 kN load cell. The illustration of the Iosipescu fixture from Wyoming Test Fixture Inc is shown in Figure 2.34. The complete DIC testing setup as shown in Figure 2.35 which includes two 5-megapixel cameras facing one side of the specimen, one looking down to the specimen from the top and one looking up from bottom while simultaneously capturing images. Once the DIC is calibrated and the setup is done, the specimen was inserted into the fixture with the notch located along the line of action of loading by means of an alignment tool that references the fixture. The

specimens were loaded at a rate of 2 mm/min and load values were recorded at a rate of 5 Hz.

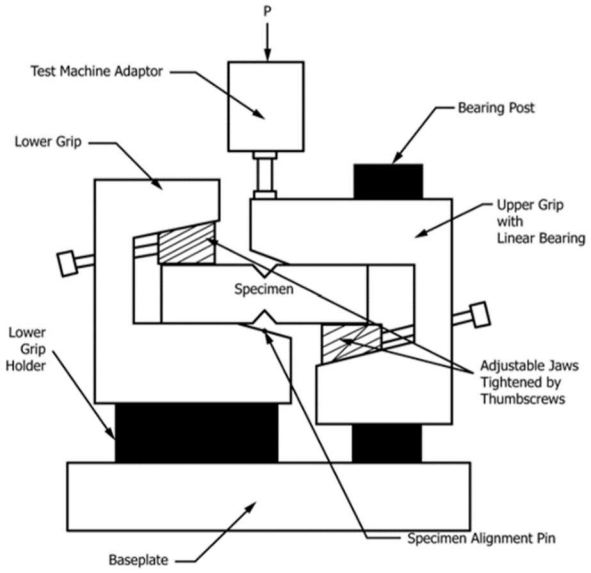

Figure 2.34: V-Notched beam test fixture schematic.

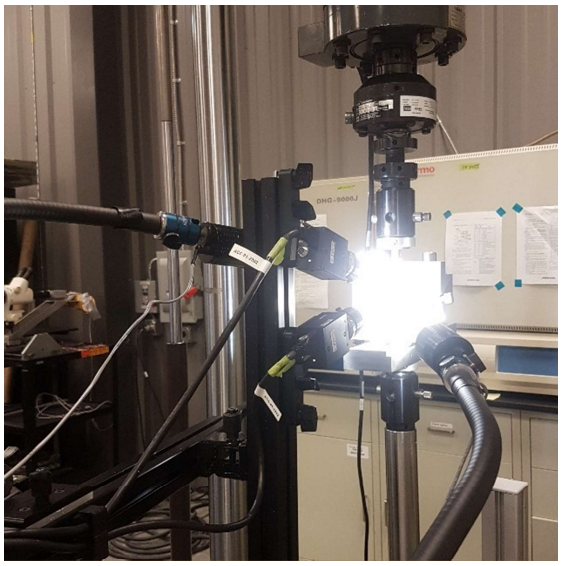

Figure 2.35: Shear test setup.

Figure 2.36 shows the fractured samples after the shear test. The failure of the samples are very consistent and repeatable. The failure mode according to ASTM 5379 [18] for this category is HGN - horizontal cracking (H) in the gage section (G) and between notches (N).

Figure 2.36: Fractured shear specimens.

Figure 2.37 shows six snapshots of the strain in the x-y direction (ϵ_{xy}) at the beginning, just before crack, after a crack was observed, while cracking, just before fracture, and after the specimen completely fractured. The strain shown in the figure is Lagrange strain tensor which defines gradients in terms of the original configuration. As expected, the high strain region is around the middle of the specimen. The crack starts at the interface between layers in the central region. Again, because there is no fiber crossing between the layers, the interface region is governed by only the matrix.

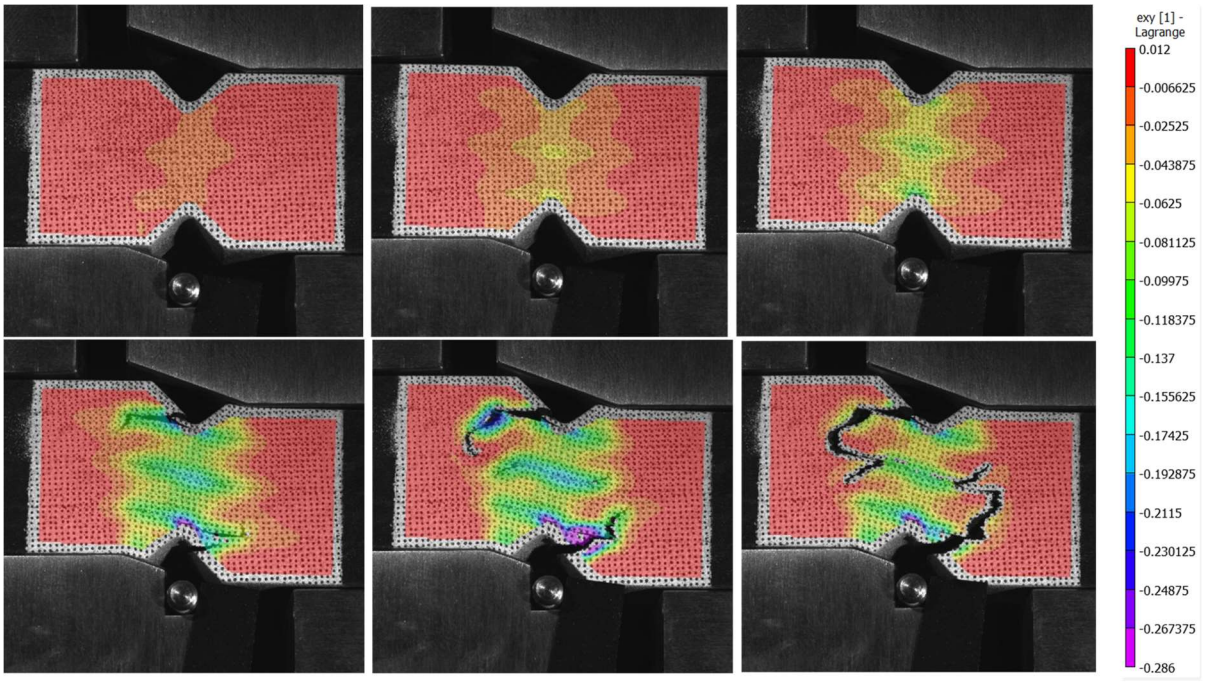

Figure 2.37: Snapshots of a shear specimen with ε_{xy} color gradient.

The DIC images were analyzed to extract the average strain over the region of interests (ROI), which in this study, is a rectangular area at the center of the specimen measuring 11 mm wide by

11 mm as shown in Figure 2.2-21. Again, the strain exported from DIC is Lagrange strain tensor which it defines gradients in terms of the original configuration. The average stress which is force applied by the crosshead divided by the cross-sectional area between the notches, and strain behavior were imported and analyzed in Matlab©.

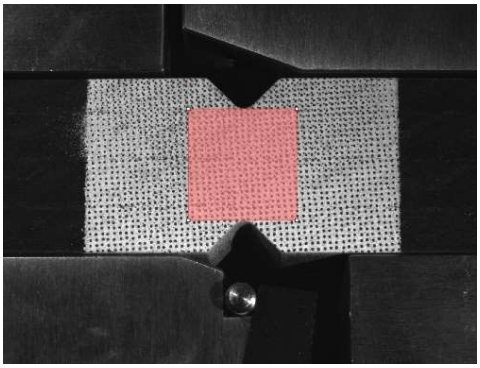

Figure 2.38: Region of interests for DIC analysis.

Figure 2.38 shows the graphs of shear stress vs engineering shear strain. Shear stress (y-axis) data were obtained from the load applied to the fixture by the initial cross-sectional area of the v-notch section. The engineering shear strain (x-axis) was obtained by twice the Lagrange strain (ϵ_{xy}) in the x-y direction obtained from the DIC. The ϵ_{xy} data is the average strain over the entire ROI. Only the linear section of the stress vs strain plot was used to calculate the shear modulus. Specifically, a linear fit was carried out for the stress vs strain data in the shear strain region comprised between 3000 με and 9000 με (indicated with dashed vertical lines in Figure 2.38) . The shear modulus (G_{13}) and ultimate shear strength (τ_{13}^{max}) are shown in Table 2.13 below. Lastly, Table 2.14 summarizes the shear modulus of elasticity and average ultimate shear strength in all three principal directions.

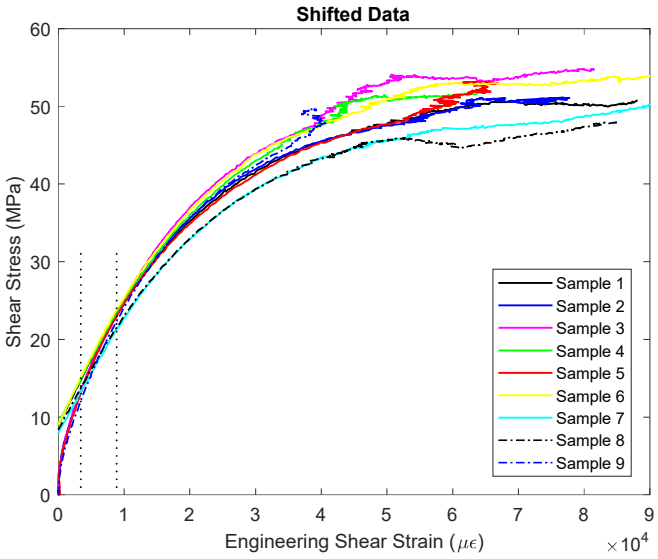

Figure 2.39: Shear stress vs engineering shear strain of all the samples.

Table 2.13: Ultimate shear strength, shear modulus, and 0.2% offset shear strength.

Sample	Ultimate Shear Strength (MPa)	Shear Modulus (GPa)	0.2 % Offset shear strength (MPa)
1	50.77	1.52	32.63
2	51.15	1.80	30.62
3	54.84	1.83	32.82
4	51.92	1.54	34.11
5	53.11	1.81	29.76
6	54.19	1.59	33.63
7	50.74	1.47	30.80
8	47.96	1.43	30.72
9	49.70	1.88	30.90
Average	51.60	1.65	31.78
STDEV	2.18	0.17	1.54
Variance	4.75	0.03	2.36

Table 2.14: Modulus of elasticity and average ultimate strength of the three principal directions.

	Modulus (GPa)				**Average Ultimate Strength (MPa)**			
	E_1	E_2	E_3	G_{13}	σ_1^{ult}	σ_2^{ult}	σ_3^{ult}	$\boldsymbol{\tau_{13}^{max}}$
AVG	13.16	7.43	6.04	1.65	144	7.43	32.4	51.60
SD	0.45	1.66	0.47	0.03	2.7	10.89	1.66	2.18

2.2.4.2. Micromechanics: Virtual Characterization for Mechanical Properties of Material Printed in the LSAM

EDAM short fiber composite bead is a heterogeneous material whose microstructure consists of a matrix material, short fibers, and voids that are in the order of micrometers. The objective of micromechanical modeling is to predict the interaction between the microstructure and the macroscopic/ overall properties. In other words, to take constituent properties obtained from the microstructure and predict the composite's mechanical performance. The process is homogenization in linear elasticity. The simplified explanation of the process is to find an equivalent homogeneous material which has the same effective macro stiffness as the real heterogeneous composite, under the same boundary conditions.

The mean field homogenization model used in this study is Mori-Tanaka model [19]. It assumes that each inclusion, i.e. fibers, behaves as if it were isolated in the matrix. That there is no interaction between inclusions and that the stress and strain in one inclusion does not affect any other inclusion. Therefore, the Mori-Tanaka model, in theory, is restricted to moderate volume fractions of inclusions. The Mori-Tanaka model is illustrated in Figure 2.40 taken from the Digimat user's manual [20].

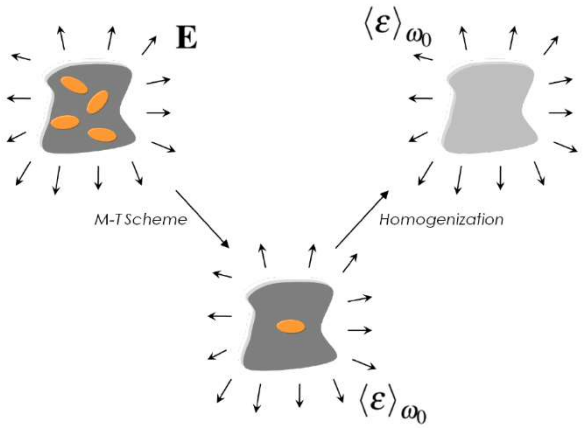

Figure 2.40: Illustration of the Mori-Tanaka (M-T) model [20].

The goal of this section is to obtain effective material properties at length scale of the bead given the experimental characterization of the microstructure (fiber orientation and fiber length) and the experimentally measured material properties. This step is necessary to account for the contribution of the material removed in the planing process of the panels in the effective properties of the bead. Further, the homogenization step conducted with Digimat predicted effective properties based on the microstructural characteristics of the bead and the properties of the constituent materials (fiber and polymer). However, the properties or the matrix is not precisely defined since fiber reinforced polymers can be compounded with additional additives to enhance different aspects of the material production and material performance. Table 2.15 lists estimates for the properties of the glass fiber and the polyamide provided by DuPont and obtained from the literature [21][22]. To capture the effects of the different additives used, the elastic properties of the polyamide were reversed

engineered based on the elastic moduli measured in three principal directions and fiber orientation of the tensile coupons. The process is illustrated in Figure 2.41. An optimal value of 3.1 GPa was obtained for the elastic modulus of the polyamide after multiple iterations through the process illustrated in Figure 2.41.

Table 2.15: Fiber and matrix properties.

Properties	Glass Fiber (E-glass)	Nylon (polyamide)
Symmetry	Isotropic	Isotropic
Density $\frac{kg}{m^3}$	2540	109
Young's Modulus (GPa)	72	3.1
Poisson ratio	0.22	0.35
Fiber aspect ratio	27.2	-
Fiber Diameter	10 microns	-

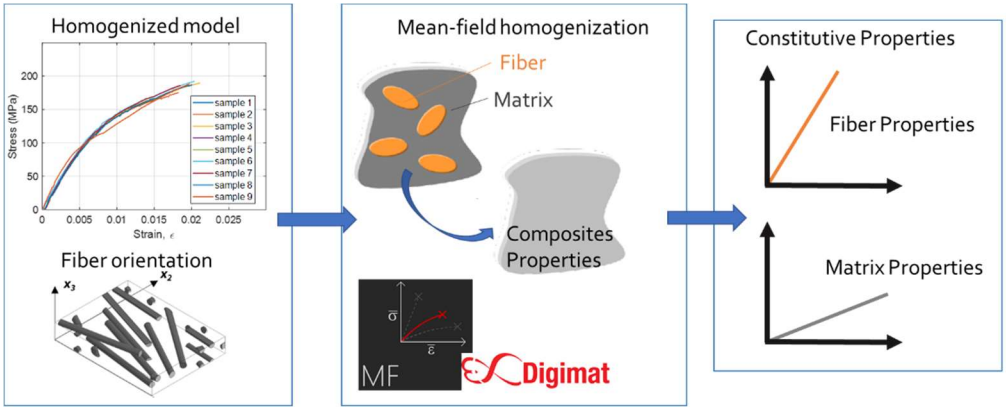

Figure 2.41: Reverse engineering process.

Utilizing the area weighted fiber orientation of the whole bead along with the constitutive properties, the nine elastic properties at the bead level is listed in Table 2.16 below.

Table 2.16: Elastic properties at the bead level.

Properties	Values	Units
E1	13.16	GPa
E2	7.43	GPa
E3	6.04	GPa
v12	3.45	
v21	2.40	
v13	2.21	
v31	0.37	
v23	0.21	
v32	0.32	
G12	0.15	GPa
G13	0.40	GPa

G23	0.32	GPa

2.2.5. Thermophysical Properties

2.2.5.1. Heat Capacity

The heat capacity characterization was outsourced to the Thermophysical Properties Research laboratory Inc, West Lafayette, IN. Heat capacity was characterized as a function of temperature according to the ASTM E1269[20] standard. The heat capacity and density of the material are required for calculating the thermal conductivity from the diffusivity measurements. Circular specimens with dimensions of 5.8 mm (0.23") in diameter and 1.5 mm in thickness or square specimens with dimensions of 3.8 mm in length and 1.5 mm in thickness are required. Further, the heat capacity measurements are independent of the material orientation, and therefore specimens can be prepared from any plane in the material. Figure 2.42 shows the plot of heat capacity as a function of temperature and the heat capacity value are tabulated in Table 5.4 in the APPENDIX. The changes in heat capacity C_p due to temperature (sensitive heat) are decoupled from the changes in heat capacity due to the crystallization of the polymer (latent heat) by considering a linear increase in heat capacity from the inflection point where crystallization starts to develop to the point where the crystallization terminates (shown in Figure 2.42). In addition to releasing or absorbing heat during the crystallization of the polymer or the melting of polymer crystals, respectively, additional polymer shrinkage develops, which is discussed in more detailed in the section 2.2.7.2.

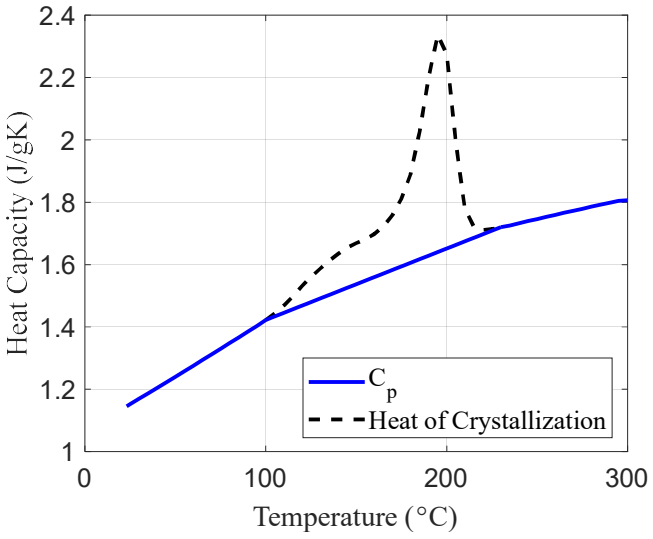

Figure 2.42: Heat capacity as a function of temperature of the GF-PA material system.

2.2.5.2. Thermal Conductivity

The thermal conductivity of a material is a measure of its ability to conduct heat. It determines the

quantity of heat which flows in unit time through unit area of a layer of the substance of unit thickness with unit difference of temperature between its faces. The characterization was also out sourced to Thermophysical Properties Research laboratory Inc which utilized the ASTM E1461 [23] laser flash method.

The specimens for the laser flash method is circular specimens with a diameter, D, of 12.7 mm $(1/2'')$ and a thickness, h of 3 mm (0.12"). The specimens require to be completely solid and with the two faces parallel. Thermal conductivity in the three principal directions were required namely with the parallel faces oriented normal to the print direction (1-direction), the transverse to the print direction, (2-direction), and the stacking direction (3-direction). The thermal diffusivity was characterized at the level of the bead, and thus specimens represent the bead-level printed microstructure. Figure 2.43 shows schematically specimens with beads oriented in the three principal directions. However, the bead dimensions may exceed the dimensions allowed for the specimen. In this case, the region from which the specimens were extracted were specified. This will allow predicting the effective thermal diffusivity at the bead level.

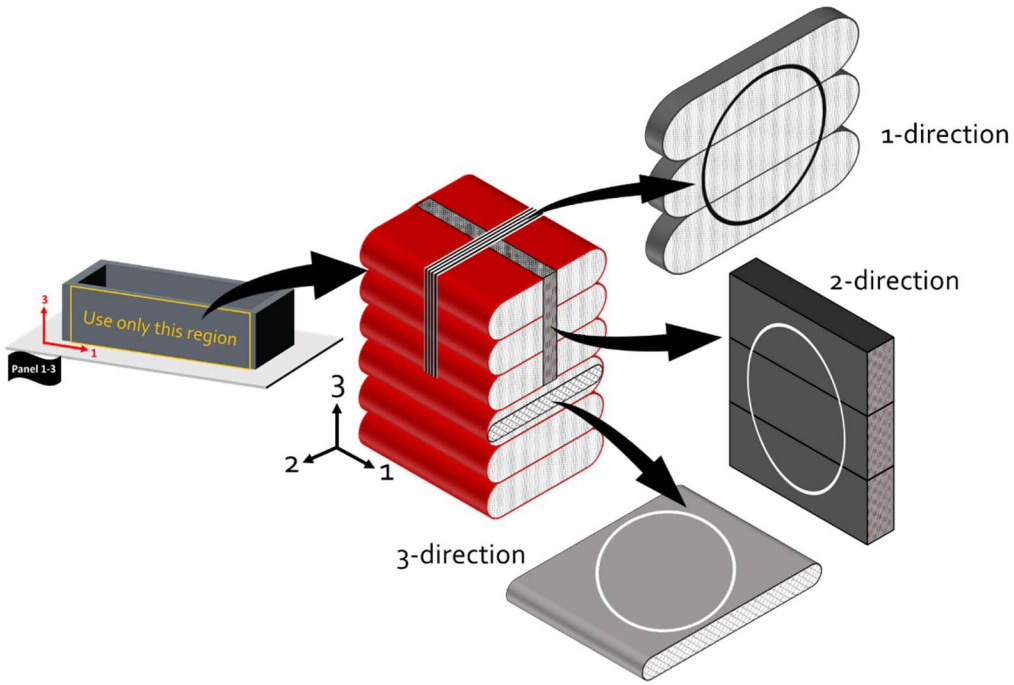

Figure 2.43: Schematic representation of bead distribution within specimens for thermal diffusivity.

Figure 2.44 shows the plot of Thermal conductivity of the specimens as a function of temperature in the three principal direction. The thermal conductivity in the 1, 2, and 3-direction is indicated as K_{11}, K_{22}, and K_{33}, respectively. The values are tabulated in Table 5.5 in the APPENDIX.

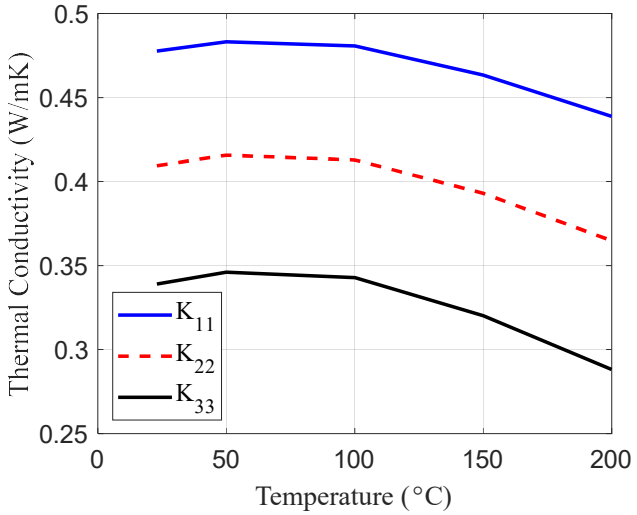

Figure 2.44: Thermal conductivity of 50% wt. GF-PA in the three principal direction.

The thermal conductivities shown in Figure 2.44 were characterized from samples that represent only a fraction of the printed bead. Which is due to limitations in sample thickness and dimensions applicable to the characterization method employed. However, effective thermal conductivities in the three principal directions are required at the length scale of the bead. To circumvent the limitation of these experimental measurements, a procedure based on micromechanics methods for predicting the thermal properties of the printed bead was conducted.

2.2.5.3. Micromechanics: Virtual Characterization for Thermophysical Properties of Material Printed in the LSAM

The section dedicated to sample preparation showed the limitations in sample dimensions in some of the material characterization methods. The thermal conductivity measurements is one of such a cases where sample dimensions are limited to capture only a fraction of a printed bead. Therefore, a virtual characterization step was performed to obtain the thermal conductivity at the bead level. As shown previously for the mechanical properties in the section 2.2.3, the objective of virtual is to reverse engineer the unknown properties of the constituent given the microstructural characteristics of the samples used in the experimental material characterization, and the experimental values obtained. Figure 2.45 illustrates the process of virtual characterization that involves the fiber orientation tensor of the samples used for thermal conductivity measurements and the experimentally measured thermal conductivity in the three-principal direction. Next, using the mean-field homogenization method, the thermal conductivity of the polyamide was reverse engineered performing multiple iterations until an optimal value for the thermal conductivity of the polyamide was obtained.

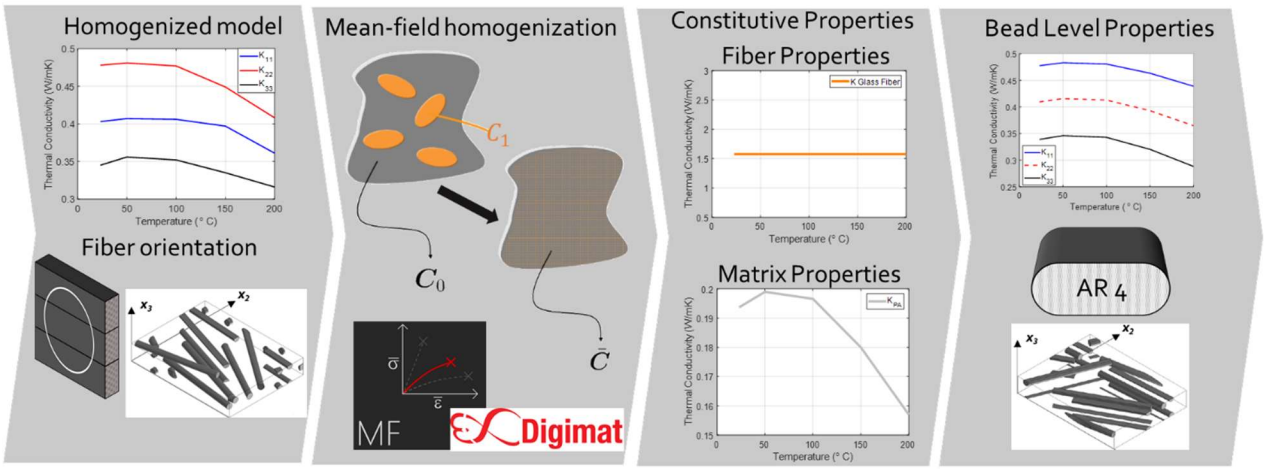

Figure 2.45: Virtual characterization for the bead level properties.

The thermal conductivity of glass fiber is assumed to be constant at 1.56 W/mK [22]. The thermal conductivity of polyamide was reverse engineered at 25, 50, 100, 150, and 200 ◦C. Once the constituent properties were obtained, the effective thermal conductivities were predicted for the 50% wt. GF-PA (30% vol. GF-PA) with the fiber orientation for the whole bead with Aspect Ratio (AR) of 4. The thermal conductivity of the three principal direction is plotted as a function of temperature in Figure 2.46 and tabulated in Table 2.17.

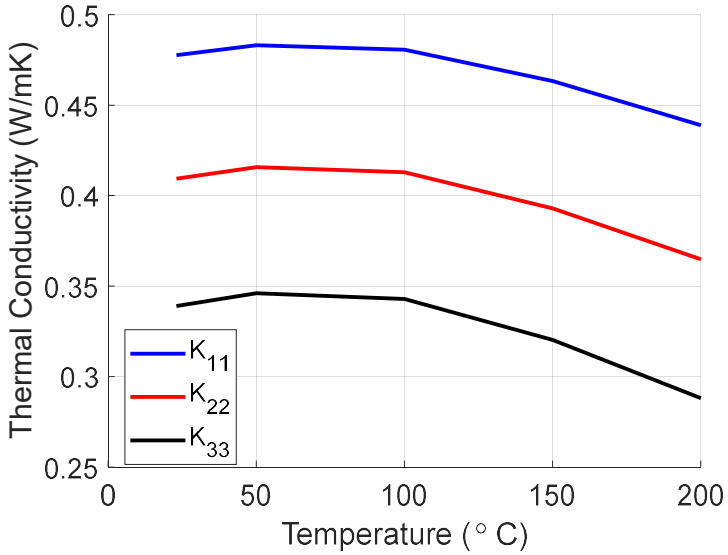

Figure 2.46: Thermal conductivity in the three principal direction.

Table 2.17: Thermal conductivity in the three principal direction and polyamide constitutive properties.

Temp (C)	*1 -direction*	*2 -direction*	*3 -direction*	*Polyamide*
23	0.478	0.409	0.339	0.194

50	0.483	0.416	0.346	0.199
100	0.481	0.413	0.343	0.197
150	0.463	0.393	0.320	0.180
200	0.439	0.365	0.288	0.157
250	0.319	0.229	0.136	0.057
300	0.299	0.208	0.114	0.044

2.2.6. Melting and Crystallization Kinetics

In EDAM process, a solid filament is drawn into an extruder, heated to a temperature where the polymer flows readily, then deposited layer-by-layer onto a build plate. After deposition, the extrudate layers bonds with the previous layer and solidifies. Depending on the polymer, the solidification process will occur either via a glass transition or crystallization process, and the type of process will have a significant impact on the mechanism of strength enhancement of the bonding between polymer layers.

2.2.6.1. Polymer Crystallization

Polyamide is a semi-crystalline polymer which partly crystallizes when they are cooled from the melt. Polymer crystallization is an exothermic process in which polymer chains locally fold in dense arrangements, called crystals, which causes a shrinkage of the material. In order to capture the polymer crystallization process in an EDAM process simulation, it needs to be described with an appropriate model definition. Two sets of experiments, isothermal and non-isothermal experiment, were performed to provide data sets to fit a phenomenological model capturing the crystallization kinetics.

A first set consists of isothermal crystallization experiments where the sample is heated and held for several minutes at the recommended material processing temperature to melt all the polymer crystals. Subsequently, the material is quenched to a constant temperature and maintained at the same temperature until the polymer starts to crystallize. Since the heat flow due to the kinetics (crystallization) can overlap with the heat flow due to the sensitive heat (due to changes in temperature and heat capacity), a baseline DSC experiment is performed to decouple the potential overlap of these two heat sources. One approach is to repeat the same isothermal DSC experiment but with a sample that has a similar thermal mass as the sample with polymer but that does not undergo any exothermic or endothermic reaction. Inert materials with a constant heat capacity in the range of temperature under consideration are recommended for the baseline measurement. As an additional recommendation for the DSC experiments, the weight used for preparing the DSC samples should be consistent within $6 \pm 0.5\ mg$. Also, material should be dried according to the recommendations provided by the manufacturer. An example of an isothermal DSC experiment conducted on a 50% wt. GF-PA is provided as a reference in Figure 2.47. The blue line corresponds to the temperature whereas and the green line corresponds to the heat flow of the sample due to the change in temperature (positive value means exothermic and negative endothermic). The peak

indicated with a red circle in Figure 2.47 corresponds to the heat released during the crystallization of the polymer under isothermal conditions.

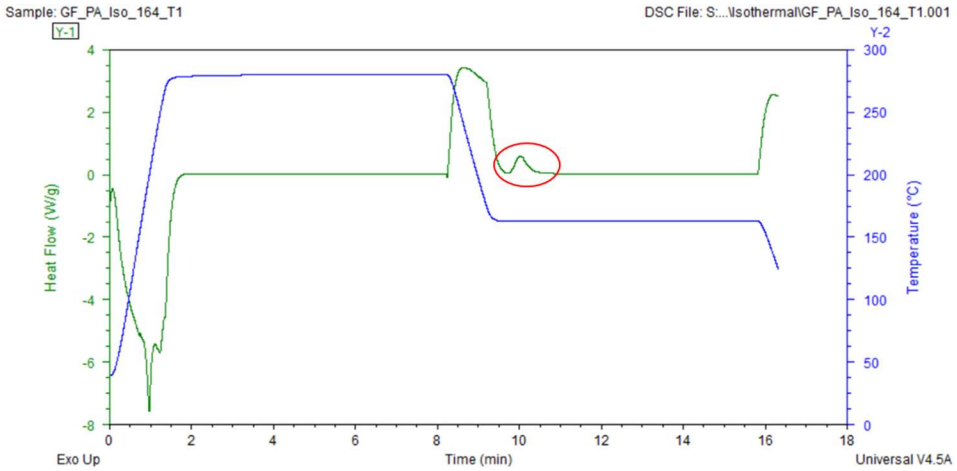

Figure 2.47: Example of isothermal DSC experiment of a semi-crystalline polymer

A general recipe for the isothermal experiments of the 50% wt. GF-PA is provided in Table 2.18. It should be noted that the cooling rate highlighted in red in Table 2.18 corresponds to the maximum cooling rate that can be achieved with the DSC.

Table 2.18: Steps required for the isothermal DSC experiments of 50% wt. GF-PA.

Step	Description
1	Equilibrate temperature at 30 $°C$
2	Ramp temperature at 200 $°C/min$ to 280 $°C$
3	Dwell for 7 min
4	Ramp temperature at 280 $°C/min$ to X$°C$
5	Dwell for 7 min
6	Ramp temperature at 200 $°C/min$ to 30 $°C$

The isothermal temperature (X) at which the experiments will be conducted is highlighted in yellow in Table 2.18. The same recipe will be carried out twice with the material under investigation and once with an inert material which is glass. Clearly, both samples should have similar thermal mass. The temperature range to perform the isothermal experiments was already determined from a non-isothermal DSC experiment and is defined between 155 $°C$ and 167 $°C$.

The polymer crystallization is an exothermic process where heat is released in proportion to the progress of the physical transformation. Therefore, the heat flow measured through the DSC serves to characterize the kinetics of the crystallization process. To determine an absolute value of crystallinity, a reference vale for enthalpy of crystallization or total heat of crystallization H_c^∞ for a completely crystallized material is required. However, complete crystallization of the polymer is not attained generally in engineering polymer grades such as the one used in this work. Therefore, the H_c^∞ for a similar polyamide was obtained from the literature and was equal to 98 J/g [24]. Since the heat capacity can be treated as a weight average property, the H_c^∞ considered in the calculation

of the crystallinity of the fiber reinforced polymer was only fifty percent of the one reported in the literature. The evolution of the crystallinity is described in terms of the degree of crystallinity defined as the ratio between the exothermic heat released during the crystallization process $H_c(t)$ and the total heat of crystallization H_c^{∞} (Equation 2.5). Figure 2.48 shows an schematic representation of the heat released during the polymer crystallization.

$$X(t) = \frac{H_c(t)}{H_c^{\infty}} \tag{2.5}$$

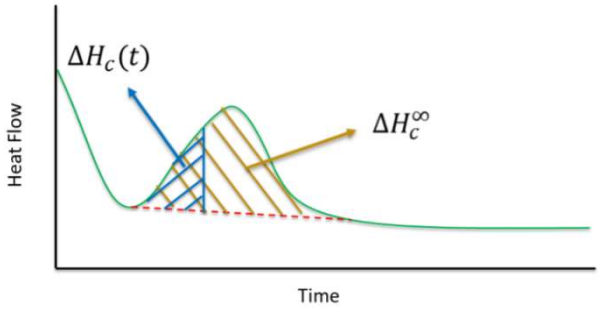

Figure 2.48: Schematic representation of the heat flow during polymer crystallization.

The isothermal crystallization data was required for generating an Avrami plot to find the Avrami exponents. This is a common way of analyzing isothermal crystallization kinetics data [25]. The Avrami equation in Equation 2.6 can be rewritten to get

$$\log\left(-log\left(1-\frac{X}{X_{\infty}}\right)\right) = \log k(T) + nlogt \tag{2.6}$$

Figure 2.49 is a diagram of $\log\left(-\log\left(1-\frac{X}{X_{\infty}}\right)\right)$ vs. log t, the Avrami exponents n can be read out as the slope of the resulting graphs. In order to generate the data, the relative crystallinity $\frac{X}{X_{\infty}}$ was computed for each isothermal temperature by dividing the crystallinity vector X by its maximum value X_{∞}. There are two different slopes that can be identified for all of the isothermal temperatures as shown in Figure 2.49. This indicates that two dominant crystallization mechanisms are governing the overall crystallization behavior, each represented by a corresponding Avrami exponent. In order to determine the Avrami exponents, linear functions were fitted to the different portions of the data for each temperature. The resulting Avrami exponents for the five different temperatures are tabulated in Table 2.19.

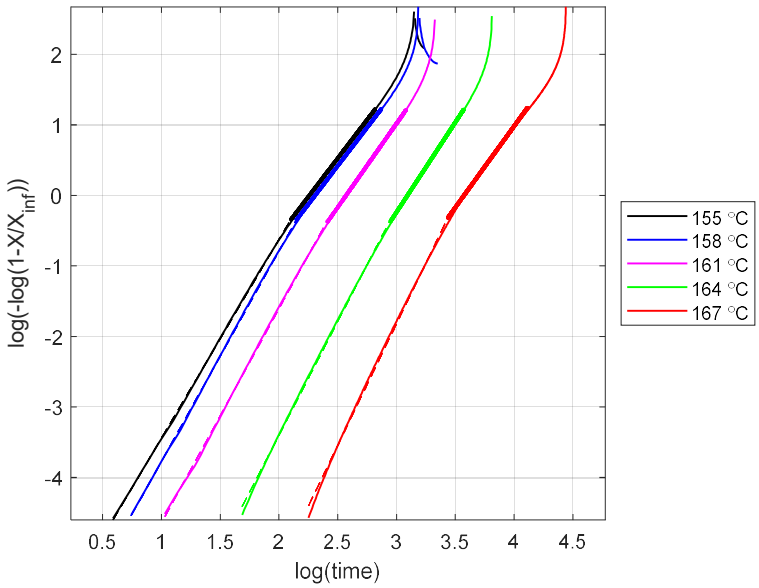

Figure 2.49: Avrami plot constructed from isothermal crystallization experiments conducted for 50% wt. GF-PA.

Table 2.19: Summary of the extracted Avrami exponents.

Temperature	***Avrami exponent 1***	***Avrami exponent 2***
155 ◦C	2.82	2.18
158 ◦C	2.98	2.18
161 ◦C	3.04	2.38
164 ◦C	3.22	2.55
167 ◦C	3.45	2.30
Average	3.10	2.32
Selected value	3.1	2.3

The EDAM printing process is a highly non-isothermal process, i.e. material cools down after material deposition. During a non-isothermal experiment, the material is exposed to varying temperature conditions, so the nucleation rate and the growth rate vary, resulting in a different degree of crystallinity. Thus, the second set of experiments to characterize crystallization kinetics of non-isothermal DSC experiments is needed. In this type of experiments, the material is heated at a constant rate to the recommended material processing temperature at 285 ℃ and held for several minutes until the all the polymer crystals are molten. Then, the sample is cooled at constant rate to the room temperature. Utilizing the cooling rates and heating rates of the same magnitude is recommended to also characterize the melting behavior. To extract more information on the melting behavior after crystallizing under controlled non-isothermal conditions, a second heating and cooling cycle should be performed. Again, the weight used for preparing the DSC samples was consistent within 6 $\pm 0.5\, mg$. One of the non-isothermal DSC experiments conducted on a 50% wt. GF-PA is provided as a reference Figure 2.2-33. The red circled peak is the exothermic

crystallization peak.

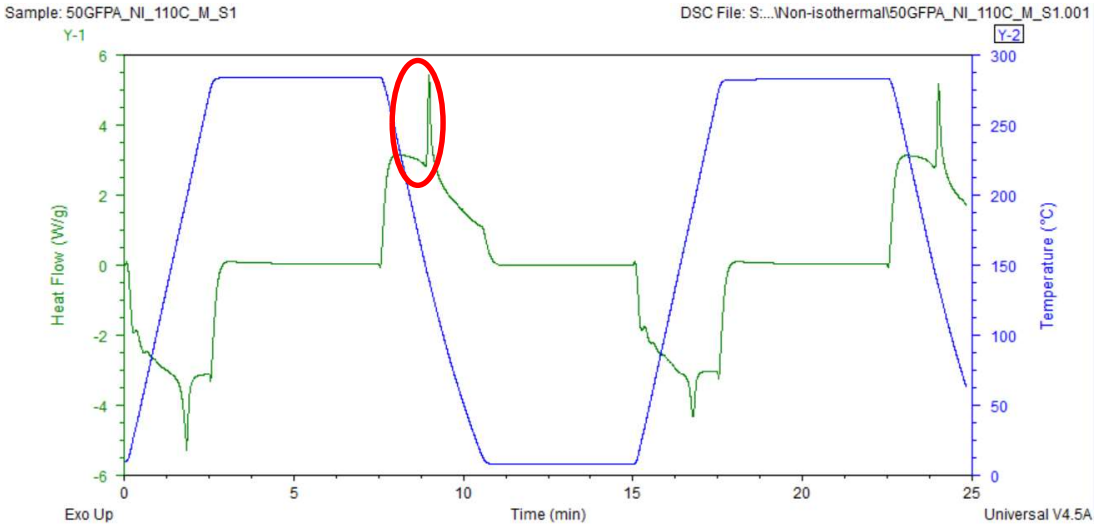

Figure 2.50: Non-isothermal DSC experiment of a 50% wt. GF-PA .

A general recipe for the non-isothermal experiments of the 50% wt. GF-PA is provided in Table 2.20. The variables in non-isothermal experiments are heating rate and cooling rate ranges from 10 $°C/min$ to 150 $°C/min$ with an increment of 10 $°C$. Clearly, the heating rate should be the same as the cooling rate for any experiment.

Table 2.20: Steps required for the non-isothermal DSC experiments of 50% wt. GF-PA

Step	Description
1	Equilibrate temperature at 30 $°C$
2	Ramp temperature at ____ $°C/min$ to 280 $°C$
3	Dwell for 5 min
4	Ramp temperature at ____ $°C/min$ to 30 $°C$
5	Repeat step 1-4

Similar to the analysis procedure of the isothermal experiments, the experimental exothermic crystallization data was exported from the DSC analysis software TA Universal Analysis© and stored in Excel© files. This data was imported with a Matlab© script to compute the evolution of crystallinity for the non-isothermal experiments. The crystallinity calculation procedure to compute was the same as for the isothermal experiments. The resulting mass fraction crystallinities for the different cooling rates are illustrated in Figure 2.51.

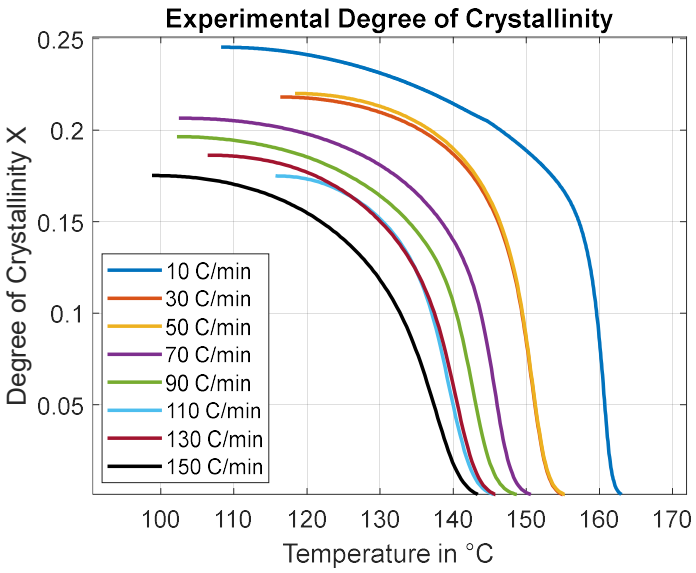

Figure 2.51: Evolution of the degree of crystallinity characterized for different cooling rates.

From studying isothermal experiment in Figure 2.49, the data shows two different slopes which can be identified for all of the isothermal temperatures. This indicates that two dominant crystallization mechanisms are governing the overall crystallization behavior, each represented by a corresponding Avrami exponent. Therefore, the Velisaris and Seferis [26] non-isothermal dual kinetics model was selected for modeling the non-isothermal due to its capabity of capturing two crystallization mechanisms. A slightly modified version of the Velisaris and Seferis model is shown in Equation 2.7 and Equation 2.8 below.

$$X_{vc}(T,t) = X_{vc\infty}(w_1 F_{vc_1} + w_2 F_{vc_2}) \tag{2.7}$$

$$F_{vc_i} = 1 - \exp[-C_{1_i} \int_0^t T \cdot exp\left[\frac{-C_{2_i}}{(T - T_g + T_{c_i})} - \frac{C_{3_i}}{\left(T(T_{m_i} - T)^2\right)}\right] n_i \tau^{n_i - 1} d\tau \tag{2.8}$$

Where X_{vc} is the crystallinity volume fraction, w_1 and w_2 are weight factors, C_{1_i} are pre-exponential factors capturing the temperature dependence, C_{2_i} are empirical parameters associated with the temperature dependence of diffusion, C_{3_i} are empirical parameters associated with the free enthalpy of nucleation, n_i are the Avrami coefficients for each crystallization mechanism. The known parameters and their values are listed in Table 2.21. Leaving 11 parameters to be determined based on the experimental data: C_{1_i}, C_{2_i}, C_{3_i}, w_1, $T_{\mathrm{m,i}}$,and $T_{\mathrm{add,i}}$ where i = 1, 2.

Table 2.21: Known parameter for the fitting process of the crystallization kinetics model.

Parameter	Value
Avrami exponent n_1	3.1

Avrami exponent n_2	2.3
Glass transition temperature T_g (°C)	70
w_2	(1 - w_1)
x_∞	0.25

The Table 2.22 provides the final parameters that describes the 50% wt. GF-PA material. Figure 2.52 illustrates the comparison of the model predictions, utilizing the model parameter from Table 2.22, with the experimental crystallization curves for several different cooling rates.

Table 2.22: Obtained best fit parameters for the Velisaris and Seferis [26] crystallization kinetics model for the 50% wt. GF-PA. .

Parameters	Mechanism 1 ($i = 1$)	Mechanism 2 ($i = 2$)
w_i	0.877	0.123
n_i	3	2
C_{1i} $(s^{-n}K^{-1})$	$8.131 \cdot 10^5$	$5.631 \cdot 10^8$
C_{2i} (K)	$2.605 \cdot 10^3$	$1.701 \cdot 10^6$
C_{3i} (K^3)	$6.467 \cdot 10^7$	$5.507 \cdot 10^{10}$
T_{ci} (K)	70.58	66.73
T_{mi} (K)	511.55	235.03

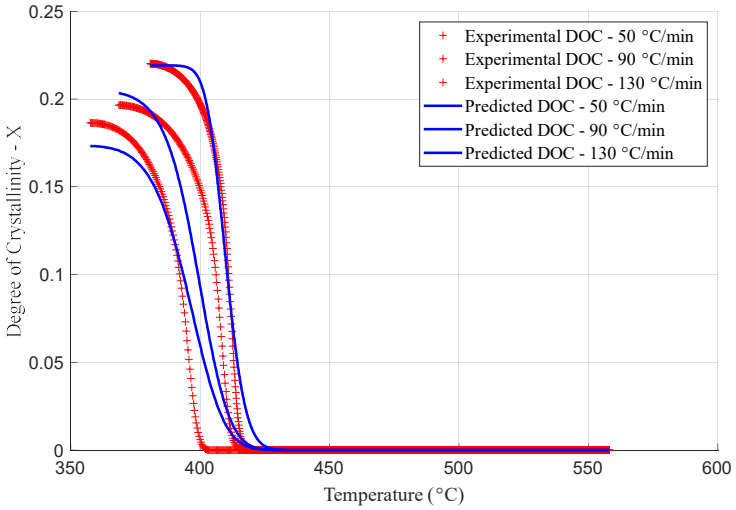

Figure 2.52: Comparison of the model prediction for crystallinity with the experimental data for various different cooling rates.

2.2.6.2. Polymer Melting

In EDAM, re-melting occurs at the regions when a newly deposited material is in contact with the partially crystallized previous deposited bead. The melting material was characterized using DSC experiments similar to the crystallization kinetics characterization experiments. In fact, the same non-isothermal data was utilized, but focusing on the heating cycle.

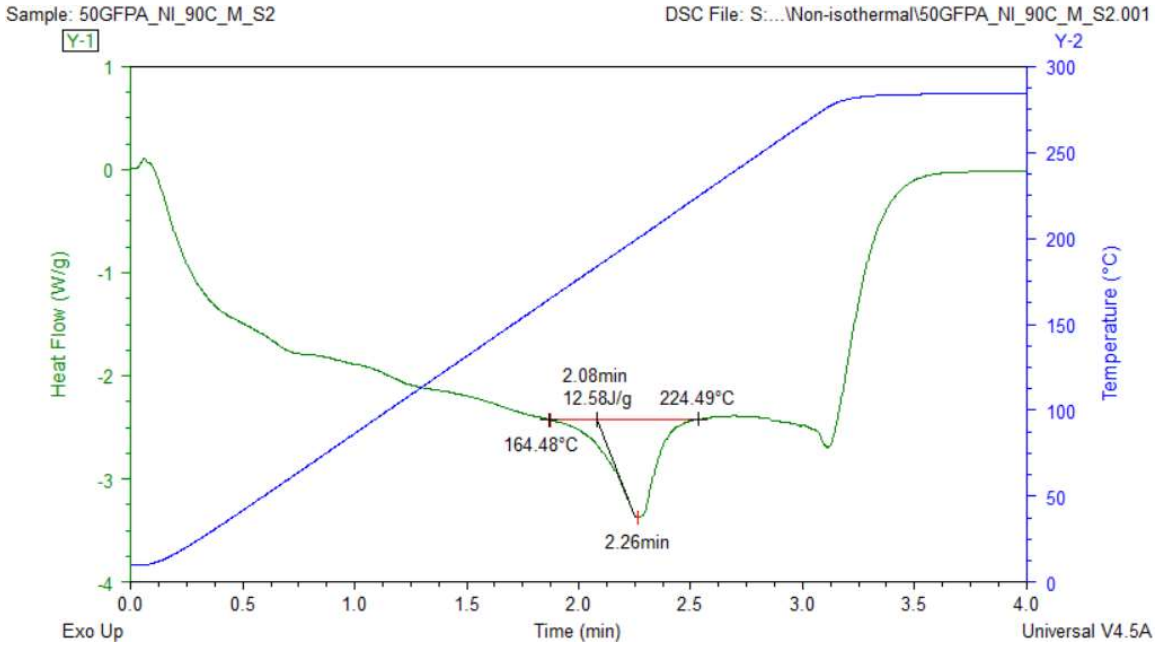

Figure 2.53: Illustration of the endothermic melting peaks in the heat flow signal for the heating rates 90°C/min.

The heating rates are in the range of 10°C/min – 150°C/min and the melting kinetics behavior was investigated by analyzing the endothermic melting peak in the heat flow signal. Figure 2.53 shows the melting peaks for the heating rates of 90°C/min. An statistical temperature dependent melting model proposed by Greco and Maffezzoli [27] was utilized to describe the melting process of the material as shown in Equation 2.9.

$$X_m(T,p) = \left\{1 + (d-1)e^{-k_{mb}(T-T_c)}\right\}^{\frac{1}{1-d}} \tag{2.9}$$

Where $X_m(T,p)$ is the relative degree of melting, and T_C is average maximum melting peak temperature which is the average maximum temperature of the peaks from the experimental data. Leaving, d, shape parameter, and k_{mb}, the intensity factor the only two fitting parameters. The resulting values for the optimized parameters are provided in Table 2.23. A comparison of the model prediction with the temperature dependent degrees of melting for the different melting rates from the experiments is illustrated in Figure 2.54.

Table 2.23: Optimized parameters for the melting model.

Parameter	Value
T_C (K)	464.27
k_{mb}	0.1532
d	1.7575

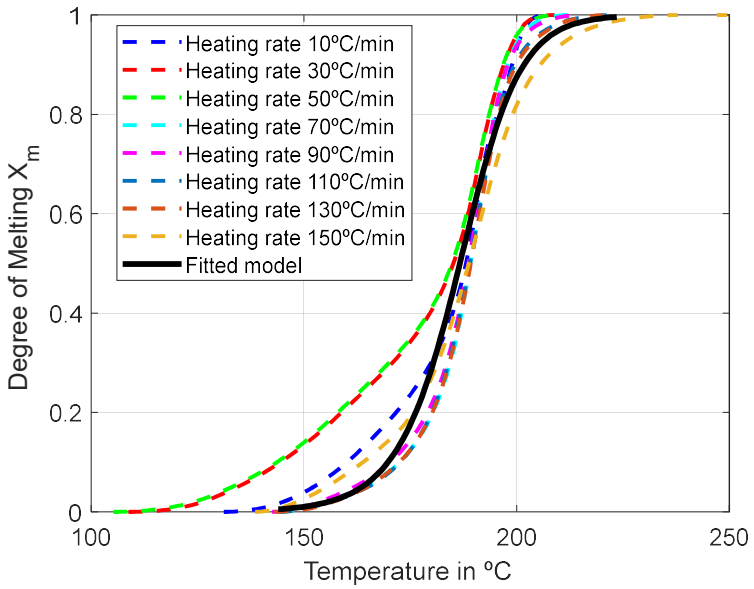

Figure 2.54: Comparison between the experimental results and the prediction by the fitted melting model for the temperature dependent evolution of the degree of melting.

2.2.7. Thermomechanical Properties

2.2.7.1. Glass Transition Temperature

The glass transition is a property of only the amorphous portion of a semi-crystalline solid. The crystalline portion remains crystalline during the glass transition. At a low temperature the amorphous regions of a polymer are in the glassy state which the molecules are frozen on place. When a semi-crystalline polymer is heated, the temperature at which the polymer structure turns from solid to rubbery is called the Glass Transition Temperature,T_g[28]. At this temperature polymer now is in its rubbery state and portions of the molecules can start to move around.

In this project the dynamic mechanical analysis (DMA) was utilized to measure T_g. DMA measures the viscoelastic moduli, storage and loss modulus, damping properties, and tan delta, of materials as they are deformed under a periodic (sinusoidal) deformation (stress or strain). DMA experiments were carried out in a TA InstrumentsQ800. The double cantilever fixture used in this experiment is shown in Figure 2.55, the middle fixture oscillates with a frequency of 1Hz, with the strain amplitude of 60 με.

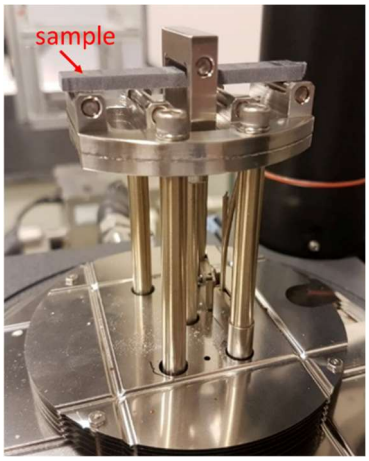

Figure 2.55: DMA setup with double cantilever fixture used for stress relaxation experiments.

The temperature of the furnace ramped to 250℃ by 5℃ /min. Since, T_g is independent on the direction, a sample of any direction can be tested. The length of the sample was 60 mm, width is approximately 3.78 mm, and a thickness of 2.75 mm.

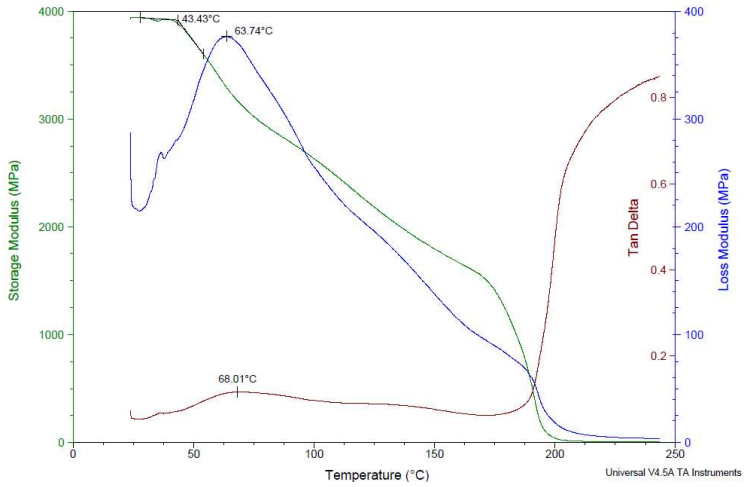

Figure 2.56: Tg obtained from the storage modulus, the loss modulus, and the tan delta vs temperature of 50% GF-PA.

The glass transition temperature can be obtained from three methods: from storage modulus, loss modulus, and tan delta. The graph of the storage modulus, loss modulus vs temperature and the T_g obtained from the three methods is depicted in Figure 2.56. The T_g obtained from the DMA and DSC is listed in Table 2.24. The T_g obtained from the onset of decrease in the storage modulus is 43.43 ℃ which occurs at the lowest temperature and relates to mechanical failure. The T_g obtained from the peak of loss modulus is 63.74 ℃ which occurs at the middle temperature and is more closely related to the physical property changes attributed to the glass transition in plastics. It reflects molecular processes and agrees with the idea of T_g as the temperature at the onset of segmental motion. Lastly, T_g from the Tan Delta Peak is 68.01 ℃ occurs at the highest temperature

which is physically midpoint between the glassy and rubbery states of a polymer [28]. Glass transition temperature of polymer is a range temperature. For modeling, the T_g of 63.74℃ was chosen as the value in between the T_g of storage modulus and tan delta.

Table 2.24: Tg from the storage modulus, the loss modulus, and the tan delta.

T_g		
Storage Modulus	***Loss Modulus***	***Tan Delta***
43.43 ℃	63.74 ℃	68.01 ℃

Coefficient of Thermal Expansion and Crystallization Shrinkage

In EDAM process, after a melted material is deposited on a surface, it cools down and shrinkage occurs. The total shrinkage of a semi-crystalline thermoplastic polymer is composed of both the thermomechanical shrinkage, governed by the coefficients of thermal expansion, and the crystallization shrinkage that is imposed when the material crystallizes. Coefficient of thermal expansion is a parameter used to express the dimensional change (volume, length, etc.) of a material in response to temperature change. Thermal expansion is defined as the change of dimensions of a body or material as a result of a temperature change. The material property constant describing this phenomenon is the coefficient of thermal expansion (CTE), indicated by the symbol α and defined as shown in Equation 2.10.

$$\alpha = \frac{\Delta\varepsilon}{\Delta T} \tag{2.10}$$

Where Δ ε is the increment of strain measured for an unconstrained material subject to a temperature change ΔT. One CTE is used to describe thermal strains for temperatures above the glass transition temperature whereas a second CTE is used for temperature below the glass transition temperature.

To ease the data reduction process, the material used in this section is 50% wt. GF-PA printed with the Composite Additive Manufacturing Research Instrument (CAMRI) system. The CAMRI system prints a much smaller bead. Keeping the aspect ratio of 4, the print bead has a bead height of 1.6 mm and bead width of 6.4 mm. The CTE sample is a square with the width of 25.4 mm and thickness of approximately 3 mm. The sample preparation steps are identical to the tensile and shear samples described in section 3.2.2 Mechanical Characterization. The order of the process is: print, heat treat, waterjet, dry, and speckle. Because 50% wt. GF-PA has fiber oriented in such a way that the printed material is anisotropic, the CTE is dependent on the directions. Therefore, samples have to be prepared for all three-principal directions. The samples tested were in the 1-2 plane (perpendicular to the stacking direction) and 2-3 plane (perpendicular to the printing direction). The 1-direction CTE was obtained from the 1-2 plane, and the 3-direction CTE was obtained from the 2-3 plane. The 2-direction CTE can be obtained from both of the samples in both planes. However, the 1-2 plane results in smoother and linear CTE while the crystallization shrinkage is more observable in the 2-3 plane. Therefore, the CTE in the 2-direction was obtained from 1-2 plane, while crystallization shrinkage was obtained from the 2-3 plane.

It is preferred to use panels printed in CAMRI system because the bead size is smaller. Therefore, multiple CAMRI system's full bead can be captured within the 25.4 mm x 25.4 mm square. This eases the virtual characterization step because the fiber orientation of the whole CAMRI bead can be utilized directly, instead of taking more micrographs of a machined shaved LSAM beads.

For the experimental set up, a Digital Image Correlation (DIC) system with a camera was utilized in combination with an INSTEC heating stage and a thermocouple to determine the temperature dependent CTE of the printed composite material and the crystallization strains. The digital camera was leveled with the plane of the sample and placed over it. The distance between the sample and the camera was adjusted to capture the full sample area covered with the speckle pattern. The test set up is shown in Figure 2.57, the sample was placed on the Kapton film in the middle of the heating stage, with both lights shining on it. The purpose of the Kapton film is to prevent melted material sticking to the heated stage plate. Next, the sample was subjected to the prescribed three-step thermal cycle during which the digital camera recorded photographs every 15 seconds. In the first step of the thermal cycle, the temperature of the heated stage was increased to 285 ℃ at a rate of 3 ℃ /min. In the second step, the temperature was held constant for 15 minutes. In the third and final step the sample was cooled down at a rate of 2 ℃ /min.

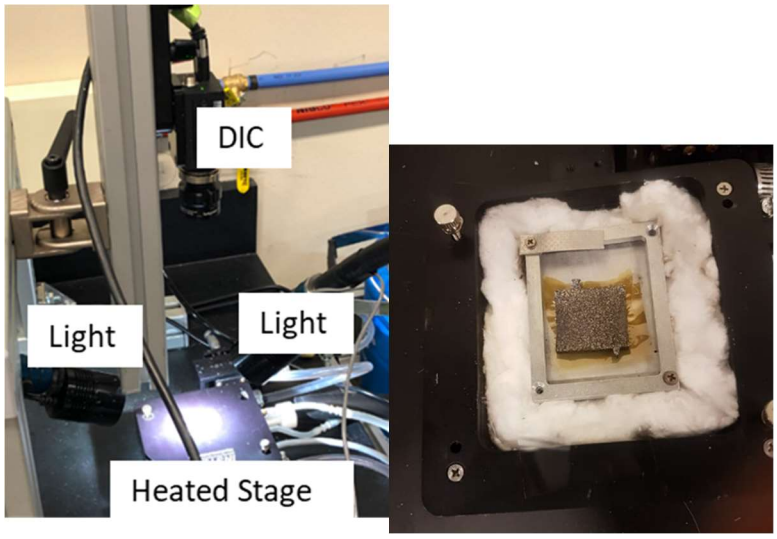

Figure 2.57: (Left) Digital image correlation setup for CTE test, (Right) sample on the Kapton film in the heated stage.

The snapshot of sample in the 2-3 plane is shown Figure 2.58. The snapshots were taken when the temperature of the heated stage is 88 ℃, 150℃, 200℃, and 230℃ as labeled. In the CAMRI prints, the fibers are mainly aligned in the 1-direction or the print direction in which fibers constrain the expansion/shrinkage of the part while temperature changes. Therefore, the sample in the 1-2 plane doesn't expand nor shrink significant enough to notice in snapshots.

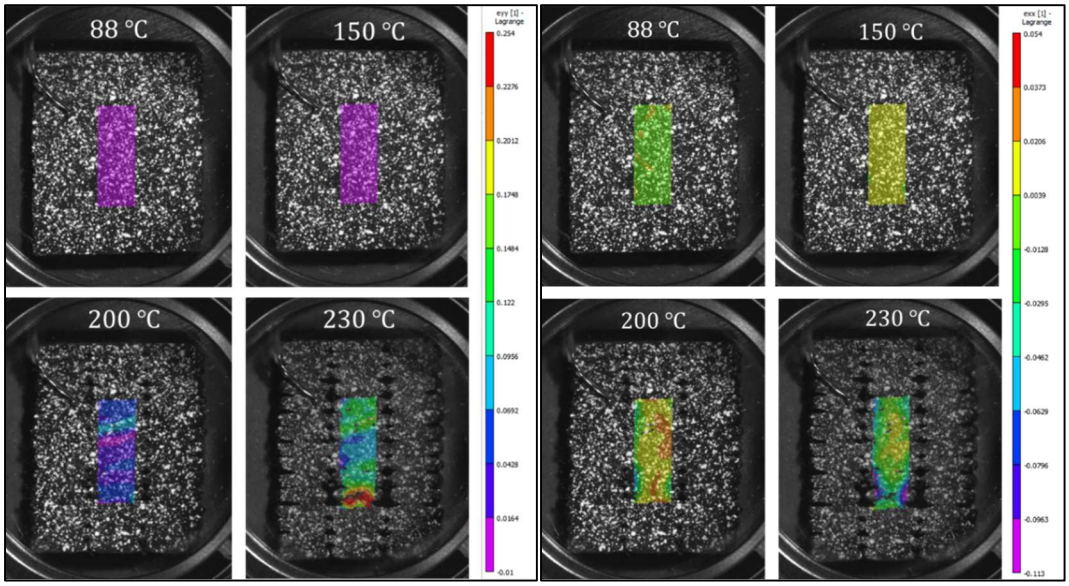

Figure 2.58: (Left) Strain in the 3-direction, (Right) strain in the 2-direction.

The strain in the three principal direction were exported from the DIC and imported into Matlab© for CTE calculation. Figure 2.59 illustrates the computed strain histories for each of the investigated directions. Figure 2.59 has three different colors, each separating the three material transitions. Temperature in the blue section is below glass transition temperature, green is between T_g and melting temperature (T_m), and red is above T_m. Crystallization occurs in the green section, as well as crystallization shrinkage.

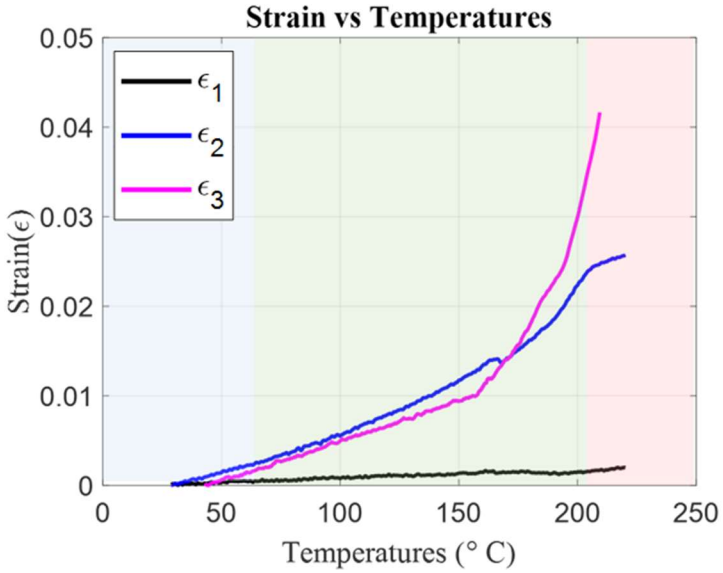

Figure 2.59: Computed strain histories from the recorded DIC data.

The CTE was obtained by linear fitting the strain at room temperature up to $T_g = 63$ ℃ and another linear fitting the strain from T_g up to 150 ℃, as illustrated in the Figure 2.60. The strain the 2-

direction was obtained from the 1-2 plane.

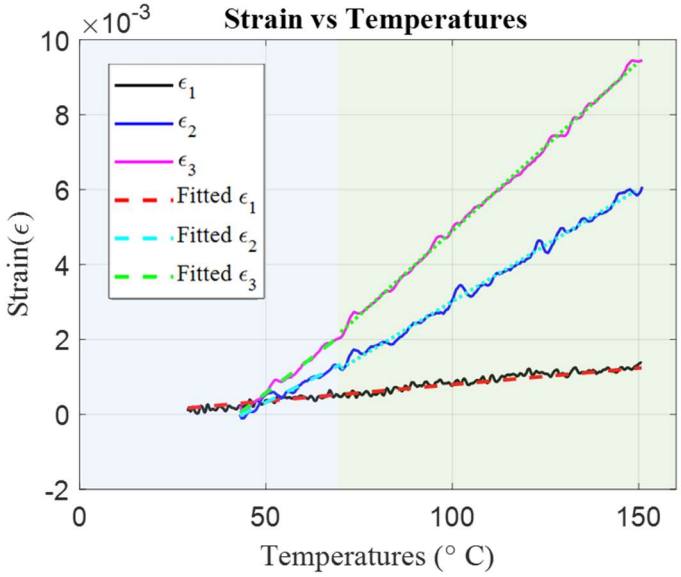

Figure 2.60: Experimental and fitted strain vs temperature.

The CTE is taken as the derivative of the fitted strain function. Therefore, the CTE will be a single value because the fitted strain is a linear function. Figure 2.61 shows the calculated CTE as a function of temperature for all the three principal directions. Those CTE as a function of temperature is also listed in Table 2.25.

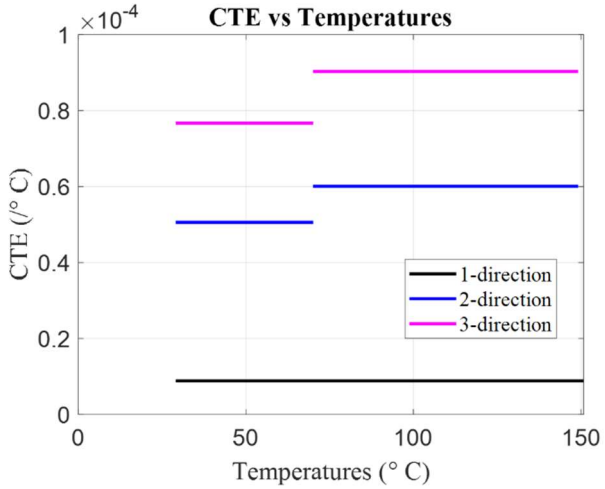

Figure 2.61: CTE as a function of temperature of the CAMRI printed parts.

Table 2.25: CTE as functions of Temperature in all three principal directions.

CTE ($°C^{-1}$)	1-direction	2-direction	3- direction
Below T_g	$8.851 \cdot 10^{-6}$	$5.055 \cdot 10^{-5}$	$7.662 \cdot 10^{-5}$
Above T_g	$8.851 \cdot 10^{-6}$	$6.004 \cdot 10^{-5}$	$9.027 \cdot 10^{-5}$

It is worthy to note that the CTE listed in Table 2.25 is the properties of sample printed in the CAMRI system. A virtual characterization involving micromechanics was needed to obtain properties of LSAM AR 4 full bead. The fiber orientation of a CAMRI and LSAM full bead is shown below.

LSAM AR4	CAMRI AR4
$A_{ij} = \begin{bmatrix} 0.57 & 0 & 0 \\ 0 & 0.34 & 0 \\ 0 & 0 & 0.09 \end{bmatrix}$	$A_{ij} = \begin{bmatrix} 0.73 & 0 & 0 \\ 0 & 0.2 & 0 \\ 0 & 0 & 0.07 \end{bmatrix}$

Digimat Mean field homogenization was the software used for this purpose. Because the 50% wt. GF-PA pellets are the same type from the same supplier, the fiber volume fraction of both CAMRI and LSAM bead is 30%. The constitutive properties of both fiber and matrix are needed for virtual micromechanics calibration as shown in Table 2.26. The fiber properties are from manufacturer and literatures. The matrix properties are calibrated from CAMRI experimental data except the Poisson ratio which is obtained from the manufacturer. The temperature was broken down to two range; below T_g and above T_g. The matrix's properties are different at each temperature range due to its viscoelastic nature.

Table 2.26: Fiber and Matrix Properties required for CTE virtual characterization.

Properties	Glass fiber	Nylon (polyamide)
Youngs modulus at 25 ℃	87 GPa	1.9 GPa
Youngs above T_g	72 GPa	1.3 GPa
Poisson Ratio	0.21	0.35
CTE below T_g	$2.5 \cdot 10^{-6}$	$8.8 \cdot 10^{-5}$
CTE above T_g	$2.5 \cdot 10^{-6}$	$1.10 \cdot 10^{-4}$
Fiber aspect ratio	27.2	-

CTE at the LSAM bead level was found utilizing the properties in Table 2.26 with the LSAM fiber orientation. One virtual characterization was done to predict the CTE below T_g and another for CTE above T_g. Finally, the CTE in the three principal direction calibrated for a full bead of LSAM with an aspect ratio of 4 is shown in Figure 2.62 and listed in Table 2.27. The Mori-Tanaka homogenization scheme used for predicting the effective CTE of the bead printed in the LSAM machine provides reliable predictions for the volume fraction in this material system [20].

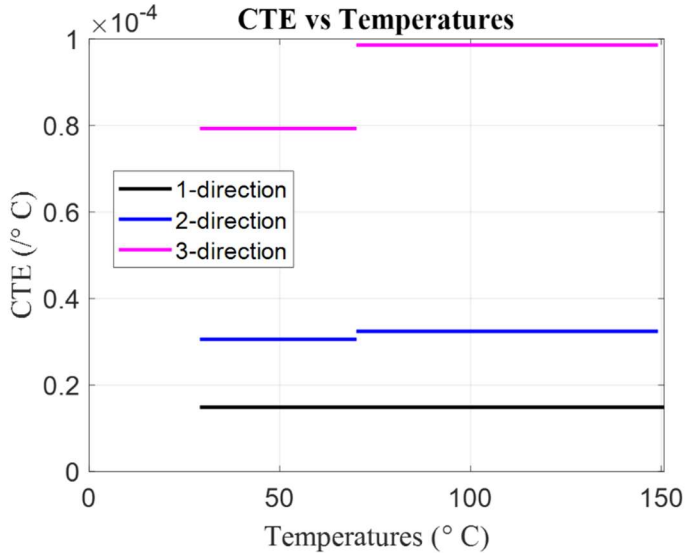

Figure 2.62: CTE as a function of temperature for the full bead printed in the LSAM.

Table 2.27: CTE as a function of temperature of the LSAM full beads

CTE ($°C^{-1}$)	1-direction	2-direction	3- direction
Below T_g	$1.487 \cdot 10^{-5}$	$3.057 \cdot 10^{-5}$	$7.93 \cdot 10^{-5}$
Above T_g	$1.487 \cdot 10^{-5}$	$3.241 \cdot 10^{-5}$	$9.861 \cdot 10^{-5}$

The CTE in the 1-direction of the LSAM's bead is significantly higher than that of CAMRI because the fibers are more collimated in the CAMRI's bead ($A_{11}^{LSAM} = 0.57, A_{11}^{CAMRI} = 0.73$). More fibers alignment helps restrain the bead from matrix expansion, while also helps restrain the bead while matrix shrinks. CTE in the 2-direction is higher for CAMRI bead because there is less fiber alignment in the 2-direction in CAMRI than in LSAM bead ($A_{22}^{LSAM} = 0.34, A_{22}^{CAMRI} = 0.2$). The 3-direction always has very few fibers alignment, therefore, the properties is dominated by the matrix. Because of this, the CTE in the 3-direction is almost identical for LSAM and CAMRI beads.

2.2.7.2. Crystallization Shrinkage

In order to estimate the effective crystallization shrinkage strains, the method illustrated in Figure 2.2-46 was employed. The figure is the strain from the 2-3 plane sample, and the focus of this paragraph is on the 2- direction strain. As illustrated in the figure for the shown example, the shrinkage strain curves were approximated with a linear fit for the strain at room temperature up to T_g (in green dashed line), and quadratic fits between T_g to the beginning of the crystallization temperature and extrapolated to the end of the crystallization temperature (in red dashed line).

The resulting shrinkage strain magnitudes are as expected, In the stacking direction (3-direction), the measured shrinkage strains of the material are the largest since almost no fibers are aligned in

this direction. In the transverse in-plane direction (2-direction) the final material shrinkage is a little more than 5 times of this value, based on the much higher amount of fibers aligning in the 2-direction, compared to the stacking direction. Finally, the total crystallization shrinkage in the printing direction (1-direction) is almost negligible due to the highly collimated fiber orientation in this direction.

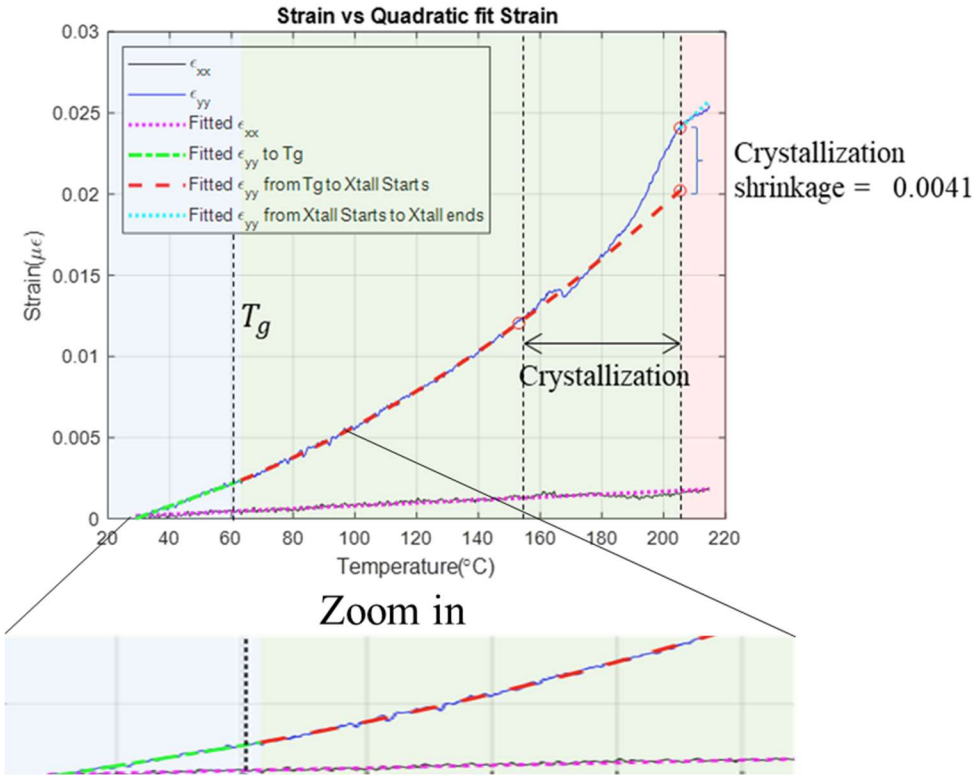

Figure 2.2-46: Experimental and fitted strain vs temperature for the 1- and 2-direction.

The crystallization shrinkage is the differences between the experimental strain and fitted strain at the end of the crystallization temperature. The strain above the end of crystallization temperature were extrapolated utilizing the same quadratic fitting coefficient (in blue dotted line). Figure 2.2-46 shows the fitted strain as a function of temperature for 1 and 2 direction.

2.2.8. Thermoviscoelastic Properties

In contrast to elastic materials, polymers show a viscoelastic mechanical material behavior. This means that they exhibit both the solid characteristics of elastic materials and store elastic energy when loaded, but also dissipate a part of the energy and flow on the microscale showing a behavior similar to fluids.

In order to characterize the thermoviscoelastic material behavior of a printed fiber-reinforced material that can be assumed orthotropic, temperature dependent relaxation experiments need to be conducted for each of the nine independent components C_{ij} of the stiffness matrix as discussed

in the 2.2.3 Elastic Properties section. A fiber- and matrix dominated relaxation behavior can be experimentally determined and applied to the corresponding other matrix components such as off-axis components of the stiffness matrix which are difficult to characterize.

A material is investigated experimentally using stress relaxation time-temperature superposition (TTS) experiments with a Dynamic Mechanical Analyzer (DMA) where material samples are automatically tested in relaxation experiments at different temperatures. The DMA sample has the dimension of 60 mm × 12 mm × 3 mm ($length$ × $width$ × $thickness$). Both the 1-direction and the 2-direction samples were extracted from the 1-2 plane. Figure 2.63 shows the location with respect to the bead of the DMA samples.

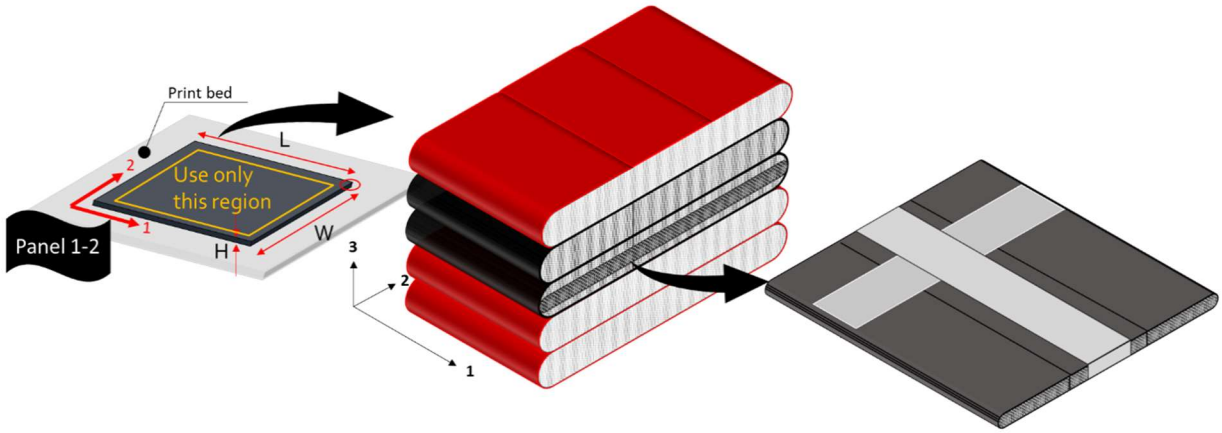

Figure 2.63: DMA samples extracted from the bead.

The TTS data was exported from the TA analysis© software and read in to Matlab©. Figure 2.64 shows the results from different relaxation experiments at various temperatures for a relaxation modulus of the 1-direction (a) and the 2-direction (b) of a printed glass fiber reinforced PA material.

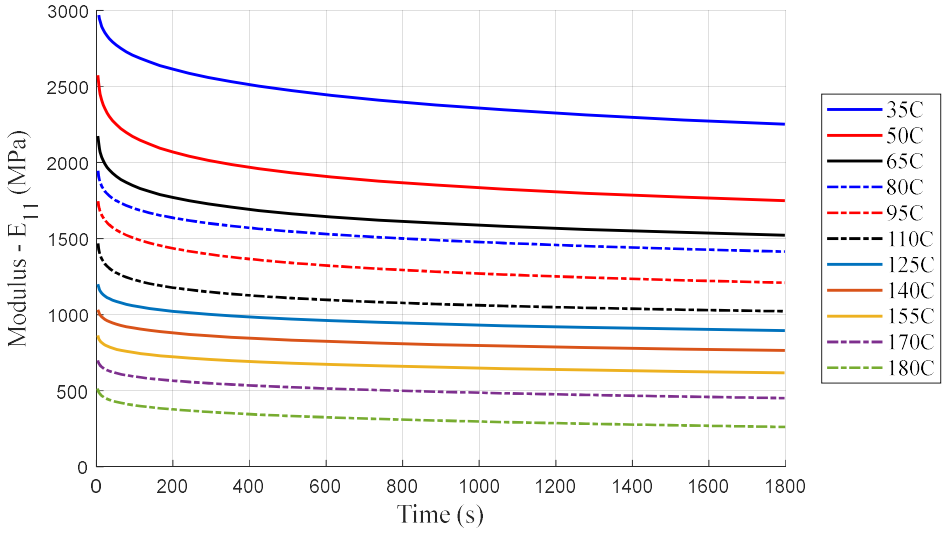

Relaxation modulus of the 1-direction at various temperatures.

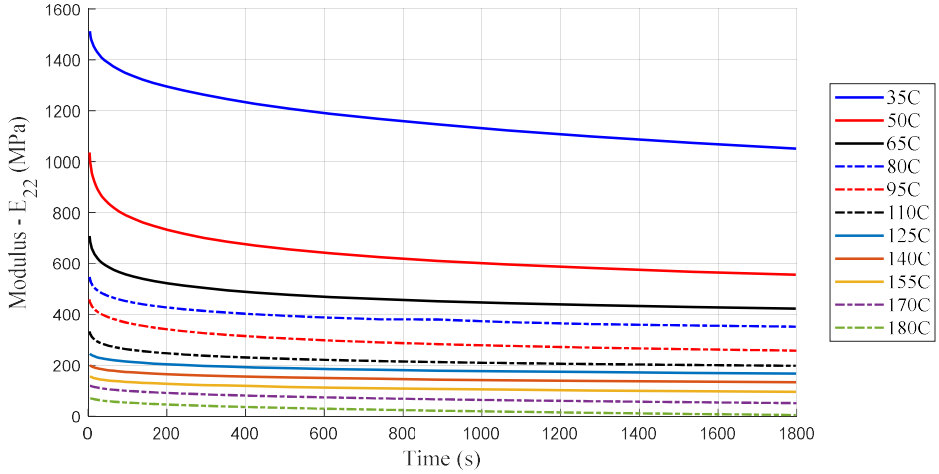

Relaxation modulus of the 2-direction at various temperatures.

Figure 2.64: Stress relaxation experiments at various temperature.

The experimental results obtained from relaxation experiments must be shifted horizontally to form master curves at a reference temperature of 65°C. The shift factor for the horizontal TTS shifts was obtained via the built-in functionality for shifting process in the software Rheology Advantage Data Analysis© from TA Instruments. A good fitting procedure is described by Brinson and Brinson [29]. Both the relaxation experiments data and the shift factor were read in to Matlab©. Figure 2.65 illustrates the resulting master curves in the 1-direction and 2- direction.

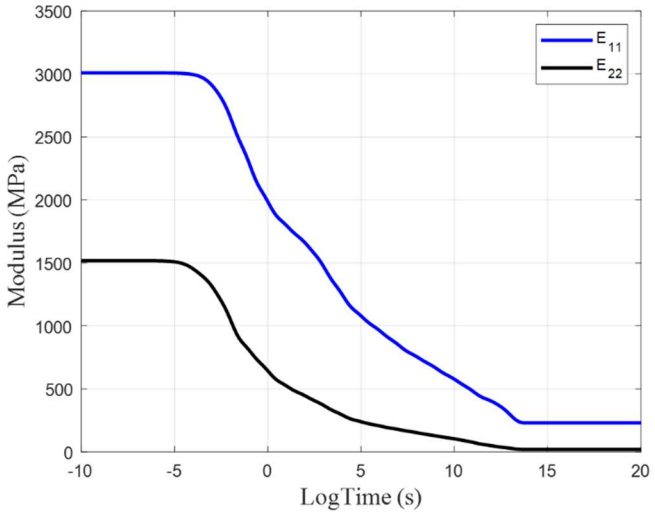

Figure 2.65: Master curves in the 1-direction and 2- direction.

A generalized Maxwell model was used to describe the relaxation behavior of the fiber reinforced polymer as a function of temperature and time [5][30]. To capture the orthotropic thermoviscoelastic behavior of the printed material, the individual components of the stiffness matrix C_{ij} were expressed with Prony series. The prony series describe master curves generated from the stress relaxation experiments conducted in the DMA at different temperatures. Further, the master curves are constructed with respect to a reference temperature T_0 as as given by Equation 2.11 [30].

$$C_{ij}(T_0, t) = C_{ij0} + \sum_{w=1}^{N} C_{ijw} \exp\left(-\frac{t}{\lambda_{ijw}}\right) \tag{2.11}$$

In the Equation 2.11, C_{ij0} are the relaxed and C_{ijw} the instantaneous parts of the stiffness matrix components. λ_{ijw} are the relaxation times of the respective Maxwell elements describing the viscoelastic behavior of the material. The accuracy of the material description is dependent on the number N of Maxwell elements used to model the material behavior. In this study 21 Maxwell elements were utilized, therefore there are 21 λ_{ijw} and 21 C_{ijw} values listed in Table 5.6 in the APPENDIX section. More information is contained in the thesis by Brenken [5].

The master curve obtained above describes the E_{11} and E_{22} of the DMA sample with a certain fiber orientation. To create a mastercurve for the properties at the bead level, micromechanics analyses are utilized as an addition to the experiments to get the full orthotropic material description. The micromechanics estimate values for all the elastic properties at the bead level can be found in Table 2.16 in the 2.2.3: Elastic Properties section. The elastic properties were multiplied to normalized master curves to estimate the full TTS behavior [1]. Figure 2.2.-50 depicted resulting master curves for the stiffness matrix components at the reference the reference

temperature of 65 ℃.

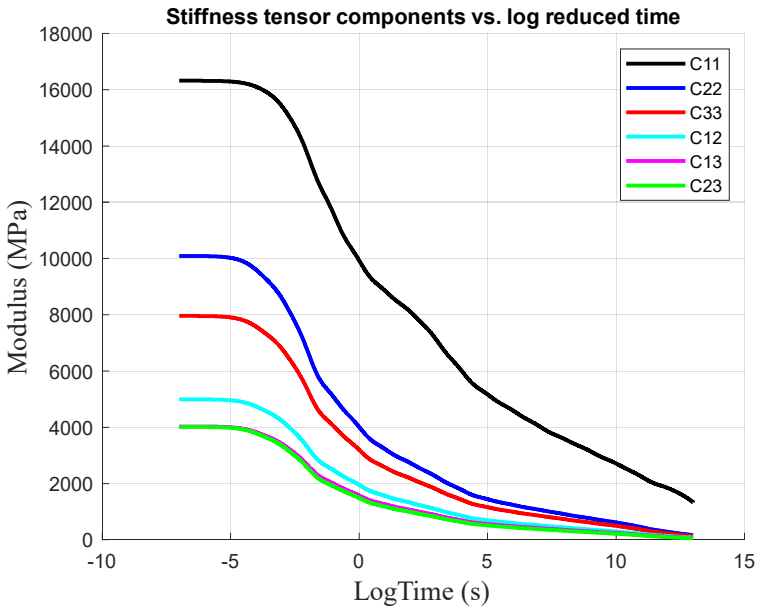

Figure 2.66: Master curves for the stiffness components.

2.3. SIMULATION OF THE EXTRUSION DEPOSITION ADDITIVE MANUFACTURING PROCESS

Predicting residual stresses and deformation developed during the printing process of a geometry is of paramount importance for mitigating expensive print trials. Printing a geometry successfully can involve multiple iterations with the current empirical approaches. Hence, predictive simulation tools are essential for assisting engineers in the design for additive manufacturing as well as for continuing expanding the applications for this technology.

A digital material card required for simulating the EDAM process with 50% wt. GF-PA was developed from the extensive characterization carried out for this material. The EDAM process is simulated using ADDITIVE3D, a physics based simulation workflow developed at Purdue University [11], [12].

2.3.1. ADDITIVE3D©

ADDITIVE3D© is a comprehensive simulation workflow that captures the multiple phenomena occurring as beads of molten material are deposited and gradually cooled during the EDAM process. Phenomena such as anisotropic heat transfer, material shrinkage, polymer crystallization, interlayer bonding, stress relaxation and creep are captured in ADDITIVE3D©. This workflow utilizes the implicit solver (Abaqus©/Standard) of the commercial finite element software Abaqus©. Utilizing the trajectory of the print head provided in the machine code, the process of

depositing material in a bead-by-bead basis is simulated by activating elements in a finite element mesh. Additionally, local orientations of the fiber reinforced polymer are mapped to each material point in the finite elements based on the trajectory of the print head [4].

The simulation of the EDAM process consists of a sequentially coupled thermomechanical analysis since the temperature field does not depend strongly on the stress and deformation fields. Figure 2.67. shows the steps involved in the simulation of the EDAM process. The first and second steps, namely geometry and slicing, are relatively standard steps in the preparation for additive manufacturing of a geometry. In the slicing process, the 3D geometry is discretized into a set of layers wherein each layer can have a unique printing pattern. The slicing outputs the machine code (G-code) that contains the trajectory for the print head. At this point in the simulation workflow, the G-code is used for generating the event series which is a discrete representation of the trajectory of the print head in time. The event series is used in both the heat transfer and mechanical analysis to coordinate the activation of the finite elements and to assign local material orientations.

The transient heat transfer analysis provides the temperature time history that governs the evolution of crystallinity in the case of semi-crystalline polymers, the thermomechanical shrinkage, and the thermoviscoelastic behavior of the printed material. Figure 2.68. summarizes the heat transfer mechanisms captured in ADDITIVE3D©. As depicted in Figure 2.68., the deposition process starts with the delivery of the extrudate of molten material at the exit of the extrusion nozzle. The material is then deposited on the top of the substrate corresponding to either the build plate or the previously deposited material. The temperature difference between a newly deposited bead and the substrate leads to heat conduction governed by the thermal conductivity that depends on the orientation of the fibers within the bead. Temperature-dependent orthotropic heat conduction is considered in ADDITIVE3D©.

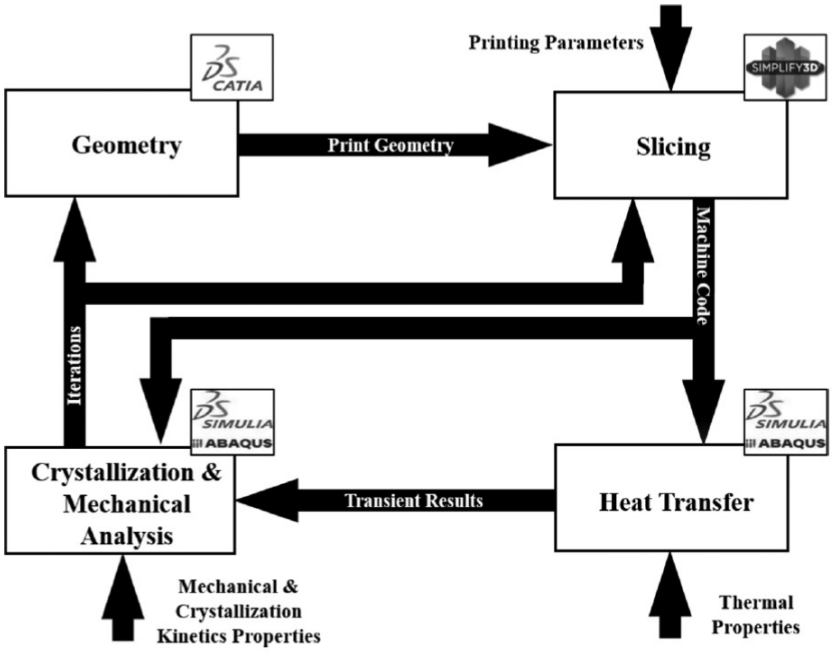

Figure 2.67. – Flowchart of process simulation in ADDITIVE3D©.

The extrudate is compacted with a roller in the LSAM to aid wetting the substrate with molten material and to close the gaps between adjacent beads. The surface of the roller is actively cooled to prevent the adhesion of the molten polymer to the surface of the roller. The temperature difference between the roller and the extrudate results in heat losses through conduction. The heat removed during compaction is captured in ADDITIVE3D© by representing the roller with an in-plane ellipsoidal heat flow distribution that moves with the deposition nozzle. Further, the total heat removed with the roller can be estimated from the heat carried with the fluid used for cooling the compacter.

The crystallization process of the polyamide used in this work releases thermal energy (exothermic process), which affects the temperature history. Further, the inverse process of melting crystallized material absorbs thermal energy. Melting and crystallization kinetics are strongly coupled with temperature in ADDITIVE3D©. As a result, changes in the temperature history affect the crystallization history and vice versa.

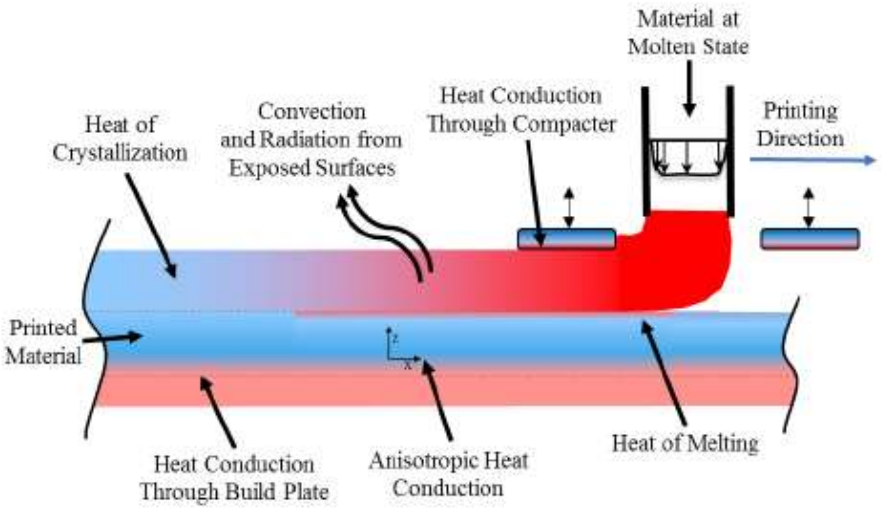

Figure 2.68. – Heat transfer mechanisms captured in ADDITIVE3D©

Thermal losses also occur by convection and radiation at the continuously changing exposed surfaces of the printed geometry. Convection arises due to heat conduction from the hot surface of the printed material to the air surrounding the part, which in turn gives rise to local changes in air density. Buoyancy driven flow arises from changes in density, thereby giving rise to a hydrodynamic and a thermal boundary layer that act together to convey thermal energy away from the surface through the movement of air. Since the convection heat transfer is highly geometry dependent, ADDITIVE3D© treats different geometric features conditions by using a set of correlation equations. Similarly, heat losses through radiation are important particularly at elevated temperatures since its contribution scales with the fourth power of the temperature at the surface. A more detailed description of the heat transfer analysis carried out in ADDITIVE3D© can be found elsewhere [6].

The stress and deformation analysis utilize the temperature and crystallinity predicted in the heat transfer analysis. Internal stresses arise primarily from restraining the anisotropic shrinkage of the printed material. As a new layer is deposited, the substrate, which is already at a relatively lower temperature is wetted with the molten material of the newly deposited bead. At that point, the shrinkage at the bottom of the newly deposited bead is practically restrained by the substrate. The difference in shrinkage developed as the layers cool down and the development of stiffness with temperature give rise to internal stresses.

The total shrinkage of a semi-crystalline thermoplastic polymer is composed of both the thermomechanical shrinkage and the crystallization shrinkage. The thermomechanical shrinkage is governed by the coefficients of thermal expansion, which is dependent on temperature and anisotropic due to the orientation of fibers within the bead. The crystallization shrinkage depends on the degree of crystallinity that forms during the cooling process and the related densification of the matrix material. Thermomechanical and crystallization shrinkage are captured in ADDITIVE3D©.

The mechanical behavior of the printed material is also anisotropic and evolves as a function of temperature and time. As the material cools down from the deposition temperature, the material stiffness undergoes multiple transitions wherein significant changes occur. For instance, fiber-reinforced semi-crystalline polymers transition from a viscoelastic-fluid like behavior to a viscoelastic-solid like behavior upon crystallization. An additional change in the stress relaxation behavior occurs at the glass transition temperature of the polymer. Including the thermoviscoelastic behavior of the fiber-reinforced polymer is paramount to predict residual stresses and deformation. ADDITIVE3D© utilizes an orthotropic thermoviscoelastic material formulation for computing the evolution of internal stresses with temperature and time. Further details on the mechanical analysis can be found elsewhere [31].

Predictions for temperature time history and deformation have been validated with a material card generated previously for 50% by weight of carbon fiber reinforced polyphenylene sulfide (PPS) [6], [11], [31].

2.3.2. Printing Experiments

Two geometries were designed and printed in the LSAM for validating predictions of the temperature time history and deformation made with ADDITIVE3D© and with the material card developed for the 50% wt. GF-PA. The geometries were designed with the following considerations. One of the geometries was designed to develop significant out-of-plane deformation due to stresses induced by the anisotropy of the printed material and by the temperature gradients developed during the printing process. Further, geometries with flat surfaces are preferred since these are less susceptible to error in the measurement of deformation. In other words, the scalloped surface introduced with the rounded ends of the printed beads can obscure the measurements of deformation. A second geometry was designed with a vertical wall to facilitate monitoring the temperature time history with a thermal camera throughout and posterior to the printing process. Further, this geometry was of similar scale as the vehicle components that are relevant to the project partners. Following these considerations, a flat plate and a curved wedge were designed and investigated in ADDITIVE3D© to confirm the expected outcome before conducting the printing experiments.

The flat plate and the curved wedge were printed with 50% wt. GF-PA in the LSAM printer at Local Motors. A build sheet made from Acrylonitrile Butadiene Styrene (ABS) was used as printing substrate. The build sheets were secured with electrical tape along the edges to a vacuum table which held the build sheets throughout the prints. A thermal camera FLIR® A655SC was used for monitoring the temperature evolution during the print. The thermal camera is calibrated for two different ranges of temperature, namely from $-40\,°C$ to $150\,°C$ and from $150\,°C$ to $650\,°C$. Thus, the temperature calibration was changed as the printed geometries cooled to below $150\,°C$. Portable cameras (GoPro®) were used for monitoring the out-of-plane deformation at specific locations in the parts during the printing process. A metric scale attached to squares placed in the field of view of the portable cameras provided a reference to estimate the out-of-plane

displacement. An extra camera was used for recording a video of the printing process.

2.3.2.1. Flat Plate

The first geometry is a flat plate with a layup (layer stack) consisting of two layers oriented at 0° followed by two layers oriented at 90°, $[0_2 90_2]$. The unsymmetrical and unbalanced configuration of this layup leads to bending-twisting coupling in the response of the plate to deformation. The chosen layup produces an anticlastic curvature that depends strongly on the mismatch in CTE of the printed material along the directions parallel and transverse to the print. Further, thermal stresses resulting from temperature gradients developed in the plane of printing also affect the anticlastic curvature developed in the plate. Hence, the flat plate is a suitable geometry for validating the predictions for deformation since deformation occurs on flat surfaces that can be readily measured with a laser scanner.

Figure 2.69 shows the CAD geometry of the flat plate printed with four layers. The plate geometry was sliced with bead dimensions of 20.32 mm by 5.08 (aspect ratio of 4). The printing speed was set to 3810 mm/min (150 in/min), thereby resulting in a print time of around 18 minutes.

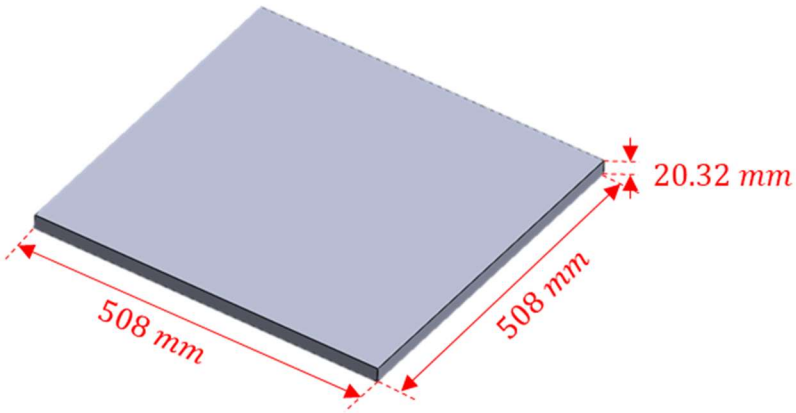

Figure 2.69: CAD geometry of the four-layer plate

Figure 2.70 shows the second and third layers generated after slicing the plate with the commercial slicer Simplify3D©. The first two layers share the same starting point whereas the last two layers share a starting point that is different from the first two layers. This slicing strategy was replicated in the slicer used for the LSAM.

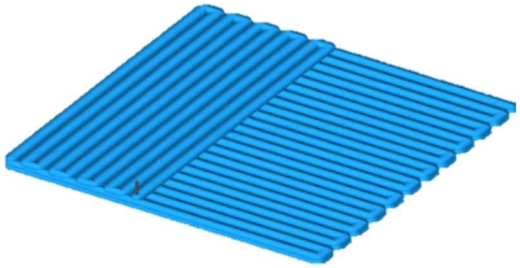

Figure 2.70: Flat plate slicing of layer 3 with Simplify 3D

Two print trials were carried out for calibrating the flow rate of the extrusion system, and thereby determining the flow rate to speed ratio necessary to close the gap between adjacent beads. Table 2.28 summarizes the process conditions used in the LSAM.

Table 2.28: Process conditions used for printing plate in LSAM

Process Conditions	Value
Print Speed (mm/min)	3810
Extrusion Temperature ($°C$)	290
Melt Pump Temperature ($°C$)	269
Nozzle Temperature ($°C$)	343
Vacuum ($mBar$)	715
Time for cooling after printing part (min)	> 15

Figure 2.71 shows the experimental setup in the LSAM which includes a thermal camera, a video camera, two portable cameras, and scales placed in the field of view of the portable cameras (not shown in this figure). The thermal camera was configured to record the temperature of the part at 15 Hz and was located at approximately 2.5 m from the plate. The first portable camera labeled as "GoPro 1" captured time-lapse photos every 10 seconds of the print and was focused on the corner labeled as 4. Similarly, the portable camera labeled as "GoPro 2" was focused at the edge of the plate in the corner labeled as 3. Finally, the video camera recorded the entire printing process of the part.

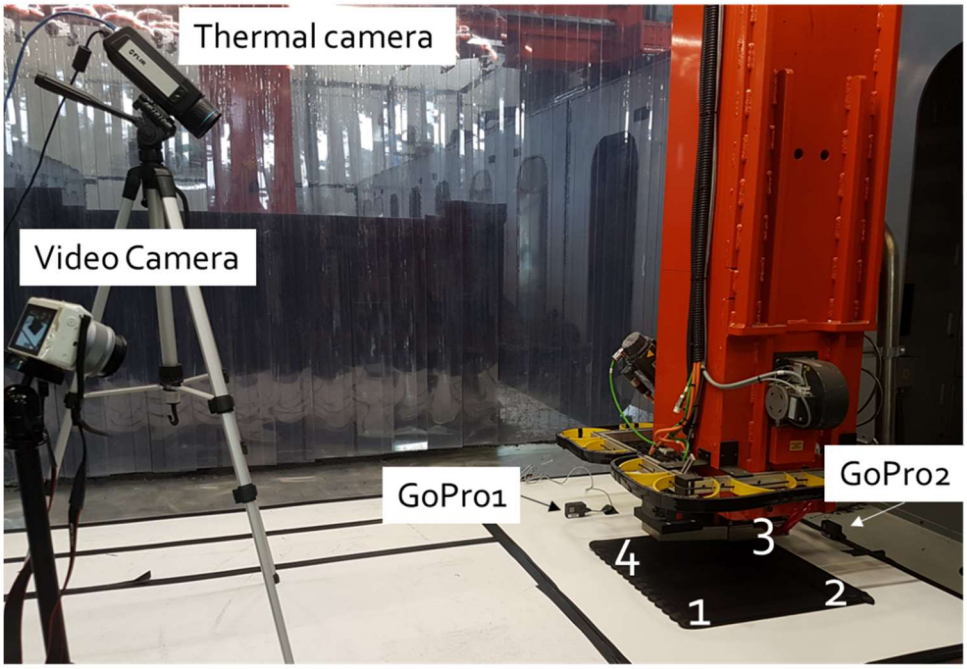

Figure 2.71: Experimental set-up used in the printing experiment of the plate.

As the plate was printed, residual stresses developed due to temperature gradients developed across the plate and to the anisotropy of the printed material, thereby giving rise to gradually debonding of the printed plate from the build sheet. The removal of the constraint imposed by the build sheet allowed the deformation of the printed plate. The time lapse photos captured the evolution of the deformation at the corners labeled as 3 and 4. Figure 2.72 shows the deformation at corner 4 at different instants of time during the print.

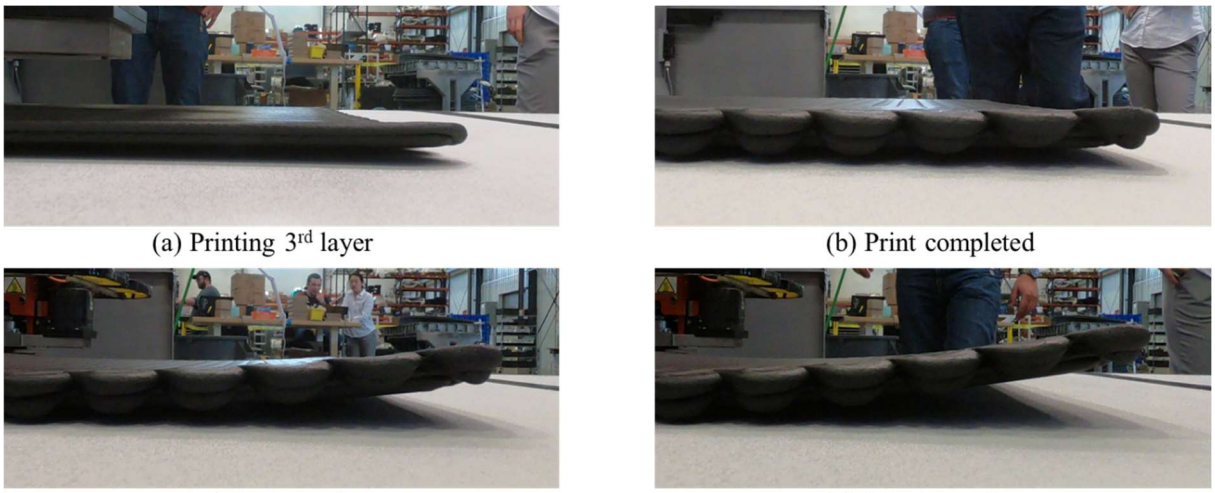

(a) Printing 3rd layer

(b) Print completed

(c) 5 min cooling

(d) 15 min cooling

Figure 2.72: Evolution of deformation at corner 4 in the printed plate captured in time-lapse photos.

The bottom surface of the printed plate was scanned using a laser Faro® arm after the part was cooled to the room temperature and the maximum deformation was developed. The bottom surface was chosen since it preserved the smoothness and continuity of the surface of the build sheet. Otherwise, the measurements would be affected by the scalloped surface created with the beads at the top of the plate. Figure 2.73 shows the point cloud scanned from the bottom surface of the printed plate.

Figure 2.73: Point cloud scanned from the bottom surface of the printed plate.

2.3.2.2. Curved Wedge

The second geometry is referred to as "Curved Wedge" and is in the scale of components relevant for the automotive industry involved in this program. Figure 2.74 shows the CAD geometry of the curved wedge. This geometry was designed with a double purpose. First, the curved section was designed to introduce stresses in the radial and hoop direction that can lead to spring-in deformation. Stresses develop due to the difference in CTE in the radial and hoop direction and thus the larger the mismatch in CTE the higher the stresses developed. Second, the tapered regions were designed to promote warpage at the ends of the part. The warpage introduced at the ends results from the competing effect of stresses developed as layers of molten material are deposited on top of previously deposited layers that are at a relatively lower temperature and the development of out-of-plane bending stiffness with the addition of new layers (bending stiffness scales with the cube of the height). Therefore, one of the ends is tapered to promote warpage by reducing the bending stiffness in the region.

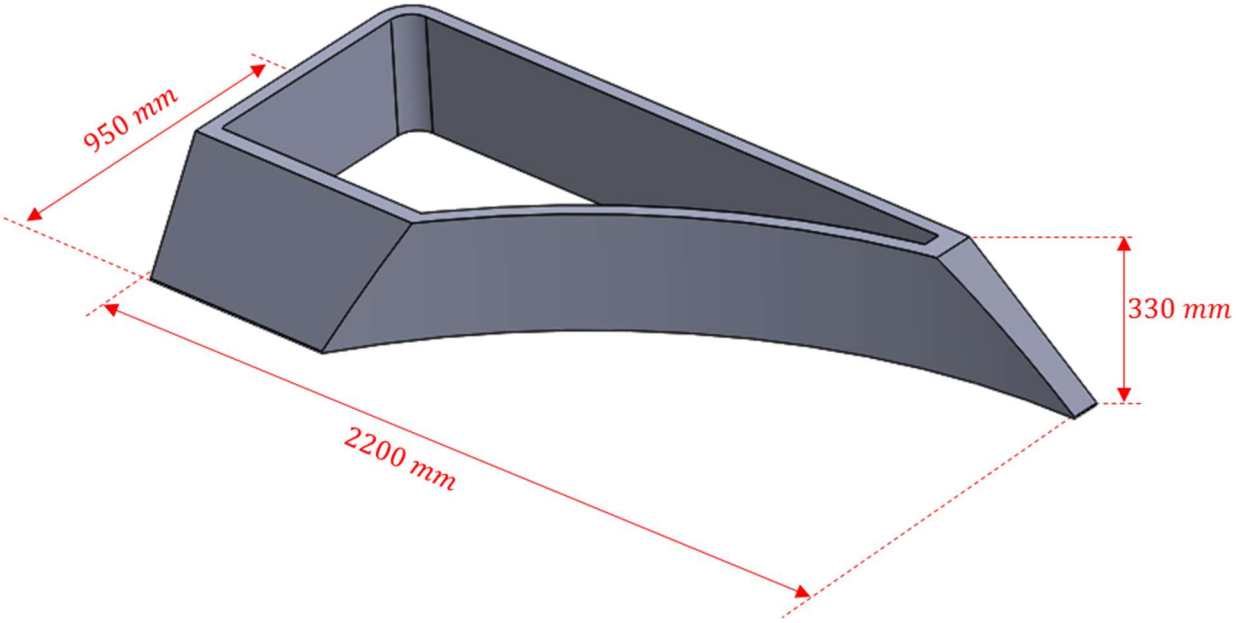

Figure 2.74: CAD geometry of the curved wedge.

The curved wedge was sliced with two beads across the width of the wall as illustrated in Figure 2.75. The beads were deposited from the inside to the outside and transitioned between layers at the front left corner as indicated in Figure 2.75. The printing speed was constant throughout the print which led to layer times decreasing from 3 min 43 sec at the bottom of the part to 3 min 4 sec" at the top of the part. Printing the 65 layers in the curved wedge took around 4 hours at a rate of 3175 mm/min (125 in/min). Once the printing process was completed, the curved wedge was left in the LSAM printer overnight for cooling with the build sheet held with vacuum. Table 2.29 summarizes the process conditions used for printing the curved wedge in the LSAM.

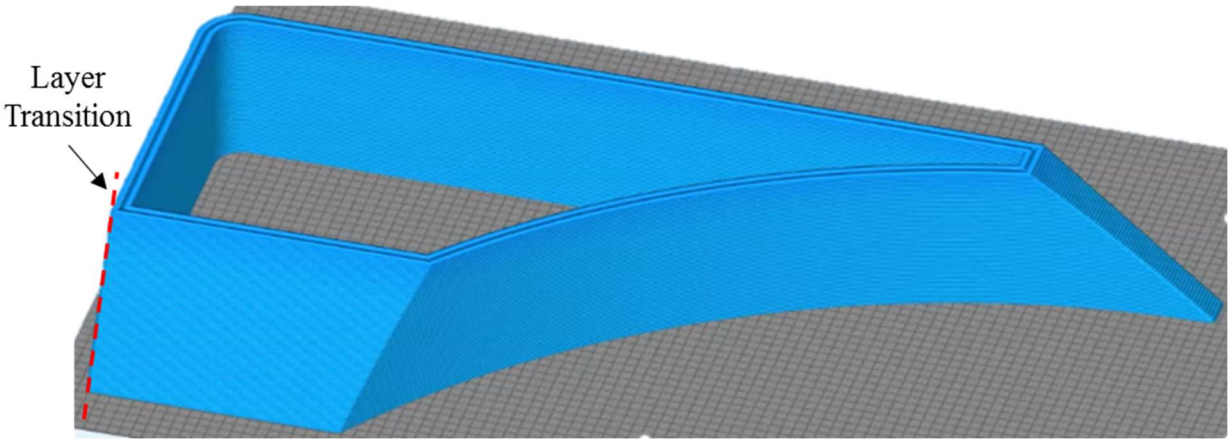

Figure 2.75: Slicing of the curved wedge geometry.

The time temperature history was recorded at the exterior surface of the longest straight wall in the curved wedge. Further, the cooling process of the part after the printing process was recorded

for about 30 minutes. Portable cameras were also employed to monitor the warpage of the curved wedge at three different corners. Figure 2.76 shows the experimental set-up used which includes a thermal camera, a video camera, three portable cameras labeled as GoPro1, 2 and 3, and three scales placed in the field of view of the portable cameras. The thermal camera was located approximately 3 m from the vertical wall in the curved wedge and recorded at 15 frames per second. The portable cameras captured time lapse photos of the print at a rate of 1 photo per 10 seconds and were focused at the corners labeled from 1 through 3 in Figure 2.76. Finally, the video camera recorded the overall printing to confirm the layer time and the start point of a new layer.

Table 2.29: Process conditions used for printing the curved wedge in the LSAM.

	Curved Wedge
Print Speed ($mm/\min$)	3175
Extrusion Temperature ($°C$)	290
Melt Pump Temperature ($°C$)	296
Nozzle Temperature ($°C$)	343
Vacuum ($mBar$)	715
Time for cooling after printing part (min)	>30

The curved wedge was printed over two pieces of build sheet connected with electrical tape at the middle. The surface appearance of the build sheets was similar despite that one section had been reused multiple times and the other section was completely new. However, differences in the adhesion of the printing material to the build sheet were noticed later between the two sections of the build sheet. Such a difference was observed while removing printing trials made for the plates. Therefore, the section of the curved wedge printed on each type of build sheet was recorded. The first 75 cm of the wide portion in the curved wedge were printed on the new build sheet (right section shown in Figure 2.76) whereas the rest of the curved wedge was printed on the reused build sheet.

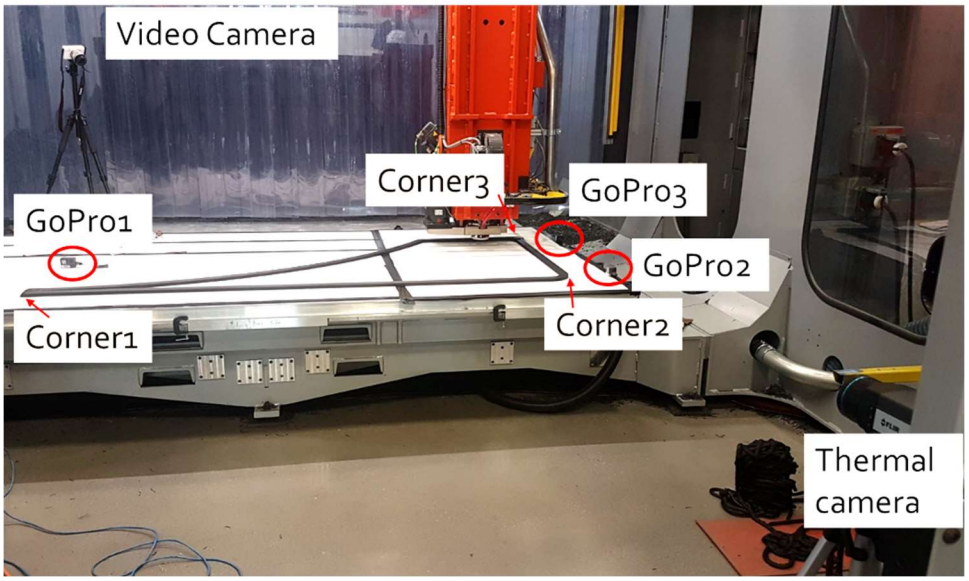

Figure 2.76: Experimental set-up used in the printing experiment of the curved wedge.

The experimental temperature was recorded with the FLIR thermal camera. The temperature extraction was done using FLIR® ResearchIR Max software. The frequency of the thermal camera was set to 15 Hz. Table 2.30 listed the parameters set for the thermal camera calibration.

Table 2.30: Calibration parameters used in FLIR ResearchIR Max.

Parameters	**Values**
Emissivity	0.92
Distance (m)	3
Reflected temp (℃)	30
Atmospheric Temp (℃)	20
Relative Humidity	50%
External optic temperature (℃)	20
Transmission	1

The curved wedge detached from the build sheet and warped up as intended at corner 1 during the print and it also warped but to a lesser extend at corners 2 and 3. Figure 2.77 shows the evolution of the deformation occurring at corner 1 as the curved wedge was printed and after cooling in the LSAM system.

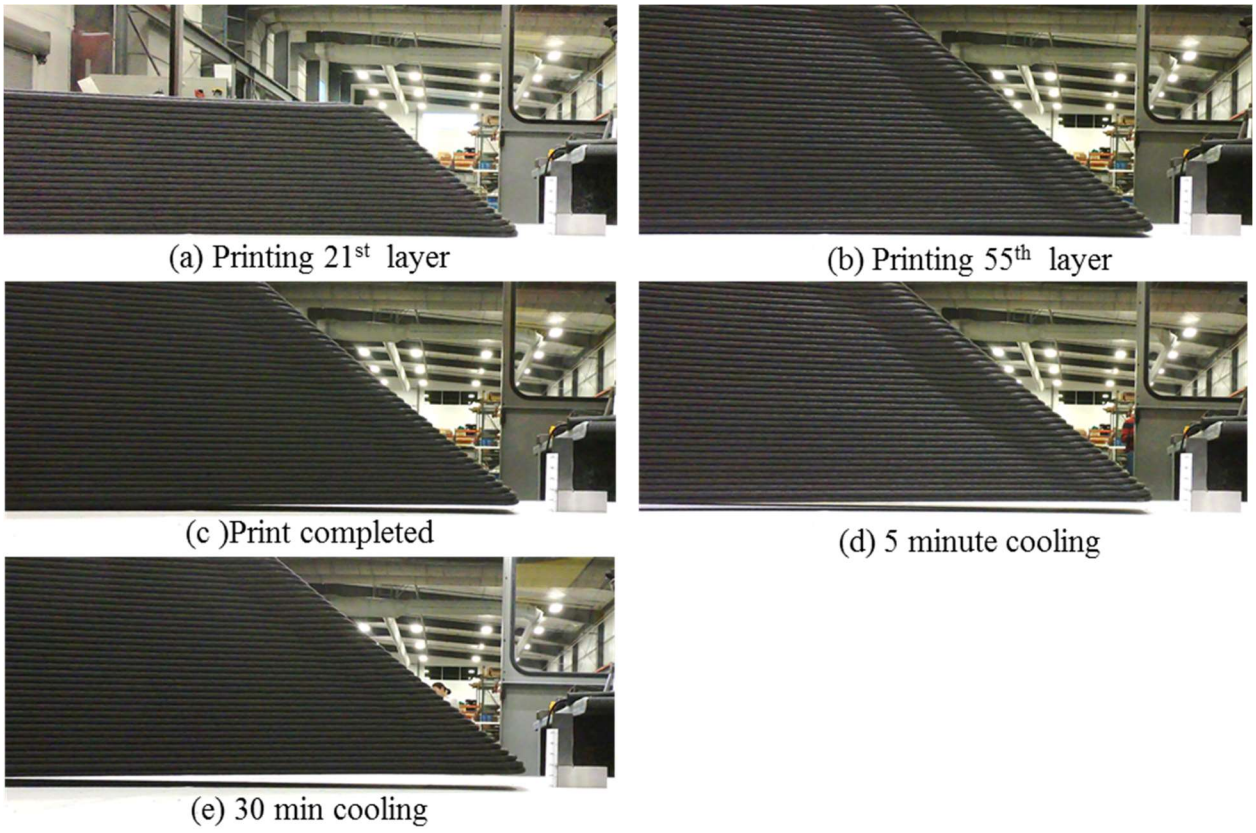

Figure 2.77: Go Pro time laps of the deformation at corner 1 of the curved wedge

Similarly, the vertical deflection was measured at the bottom of each corner after cooling the curved wedge overnight. Table 2.31 reports the vertical deformation measured at the bottom of each corner after cooling the curved wedge to room temperature.

Table 2.31: Vertical deformation measured at the bottom of each corner after cooling the curved wedge to the room temperature.

Location	Maximum deformation (mm)
Curved wedge, corner 1	16
Curved wedge, corner 2	13
Curved wedge, corner 3	13

After cooling the curved wedge overnight, the part was laser scanned with the Faro® laser scanner in three different sections. This was necessary since the reach of the scanner was not sufficient for scanning the part with a single setup. The three scans included overlap to allow aligning the three different scans in the software Geomagic Wrap©. Figure 2.78 shows the point cloud generated with the three laser scans of the curved wedge.

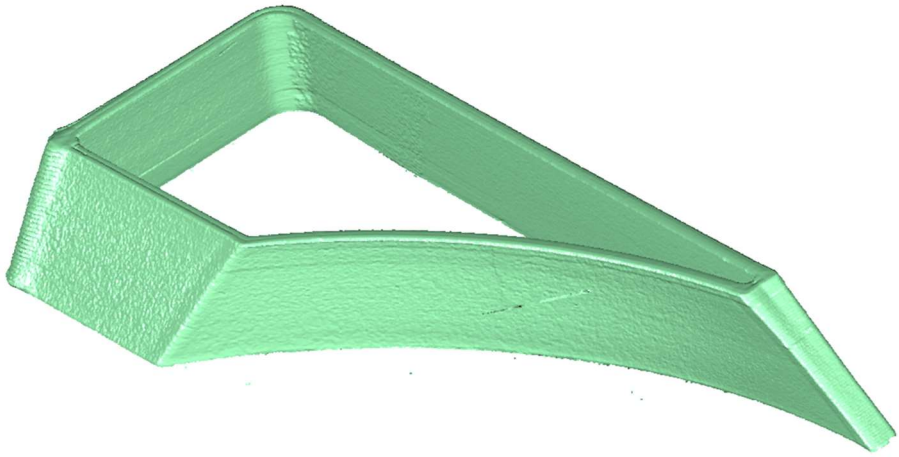

Figure 2.78: Point cloud scanned from the curved wedge printed in the LSAM.

2.3.3. Simulation of Printing Experiments

The printing process of the two geometries used for the printing experiments were simulated using ADDITIVE3D©. The first step required for simulating the printing process of a sliced geometry is to generate an event series, a spatial and temporal description of the print head motion. Utilizing the event series, the times for activating elements as well as the local orientation of the material within the part are determined [4]. The event series was generated based on the machine code (G-code) output from the slicer. A voxel finite element (FE) mesh was generated for each of the geometries using the event series. The next subsections provide the process conditions used in the simulations of the two printing experiments.

2.3.3.1. Flat Plate

A voxel FE mesh was generated based on the event series of the flat plate. Thus, elements are only present where the print head deposits material. Beads were discretized with two elements in the width and two in the height which lead to elements with dimensions of 10.16 mm in width and 2.54 mm in height. Linear brick elements type DC3D8 and C3D8 were used in the heat transfer and mechanical analysis, respectively [32]. A total of 50,045 finite elements were used to represent the geometry of the plate. To capture the process of debonding of the plate from the build sheet, a cohesive contact was defined between the bottom surface of the printed part and a substrate. The substrate was included only in the mechanical analysis and was modeled as an analytical rigid surface. This approach only considers debonding of the part from the build sheet since it was the only failure mechanisms occurring during the printing experiments. Figure 2.79 shows the FE mesh generated for the plate and the substrate that represents the build sheet.

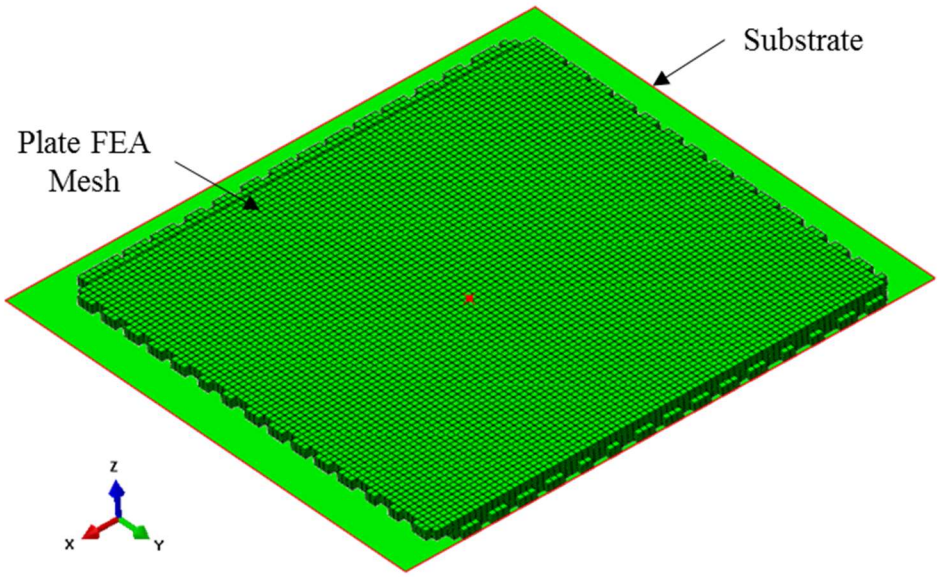

Figure 2.79: Voxel FEA mesh generated for the plate.

The material properties reported in the section Experimental Characterization Of Additively Manufactured Fiber Reinforced Thermoplastic were used in the simulation of the EDAM process. To simulate the material in the molten state prior to deposition, the temperature of the nodes in the FEA mesh were initialized to the melt temperature. The bottom surface of the plate was assumed adiabatic due to the low thermal conductivity of the material used for the build sheet (ABS). The convection conditions developed at the surface of the plate were governed by a correlation equation that provides a local convection coefficient [6]. The heat removed with the compression wheel, the emissivity, and the ambient temperature for radiation are calibrated based on the printing experiments. The addition of instrumentation such as a flow rate meter and thermocouples at the inlet and outlet of the flow lines in the compression wheel would allow characterizing the heat removed with the compression wheel [6]. Similarly, the emissivity of the material can be determined using a black body cavity printed with the same material [6]. The constitutive behavior of the cohesive contact defined between the bottom surface of the printed part and the substrate was also calibrated based on the printing experiments. The substrate was assumed to only fail under mode-I loading. Thus, a maximum stress failure initiation criterion and a displacement-based damage evolution law were used to describe the initiation and evolution of the debonding process, respectively. The cohesive stiffness, cohesive strength, and separation to failure were calibrated with the plate print experiment. Table 2.32 lists the parameters related to the process and to the material used in the simulation of the EDAM process of the plate.

Table 2.32: Parameters of the process and material used in simulation of the printing process of the plate.

Parameter	Value

Extrusion Temperature ($°C$)	300
Deposition speed (mm/min)	3810
Ambient Temperature Convection ($°C$)	35
Ambient Temperature Radiation ($°C$)	35
Heat Removed with Compression Wheel (W)	35
Emissivity - ε	0.92
Cohesive Stiffness (MPa/mm)	0.125
Cohesive Strength (KPa)	25
Separation to Failure (mm)	5

2.3.3.2. Curved Wedge

A voxel FE mesh was generated based on the event series of the curved wedge. Thus, elements are only present where the print head deposits material. Unlike the plate, a coarser mesh was used to discretize the geometry of the curved wedge. Beads were discretized with two elements in the width and one in the height which lead to elements with dimensions of 10.16 mm in width and 5.08 mm in height. Linear brick elements type DC3D8 and C3D8 were used in the heat transfer and mechanical analysis, respectively [32]. A total of 124,208 finite elements were used to discretize the geometry of the curved wedge. To capture the process of debonding of the curved wedge from the build sheet, a cohesive contact was defined between the bottom surface of the printed part and a substrate. The substrate was included only in the mechanical analysis and was modeled as an analytical rigid surface. This approach only considers debonding of the part from the build sheet since it was the only failure mechanisms occurring during the printing experiments. Figure 2.80 shows the FE mesh generated for the plate and the substrate that represents the build sheet.

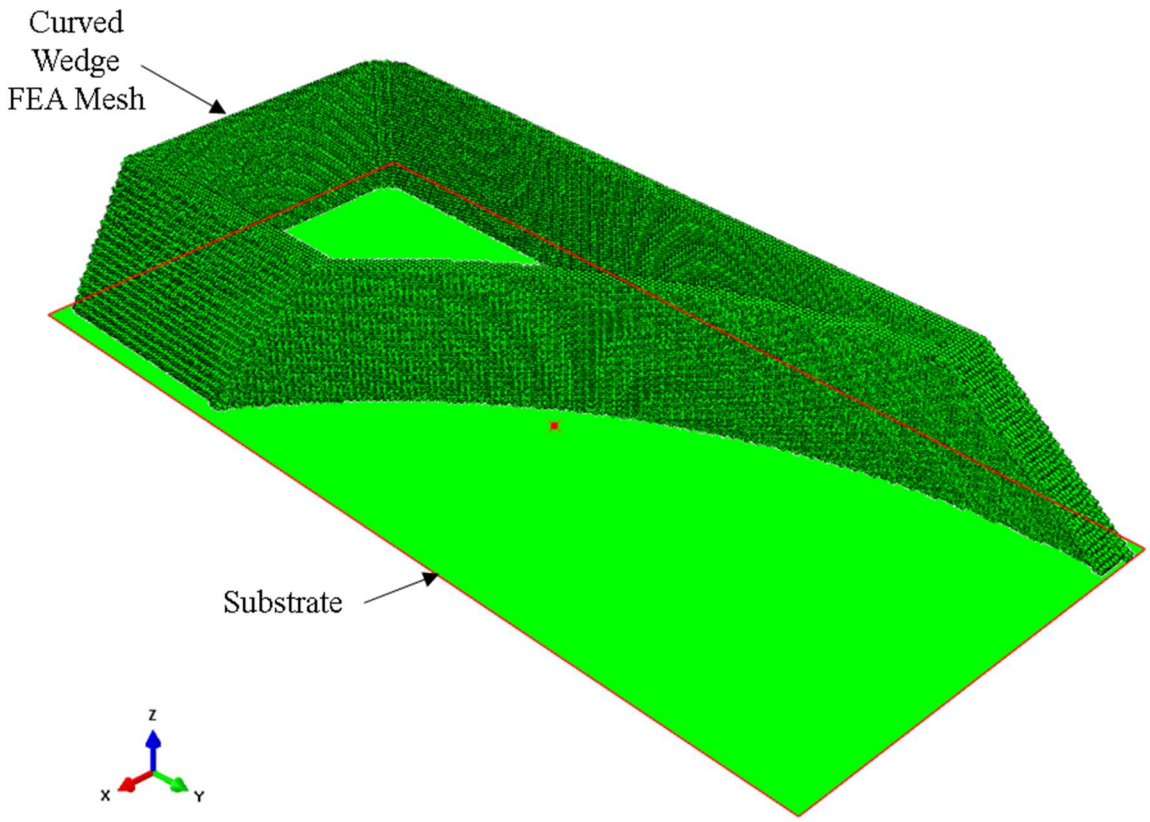

Figure 2.80: Voxel FEA mesh generated for the curved wedge.

The material properties reported in the section Experimental Characterization Of Additively Manufactured Fiber Reinforced Thermoplastic were used in the simulation of the EDAM process. To simulate the material in the molten state prior to deposition, the temperature of the nodes in the FEA mesh were initialized to the melt temperature. The bottom surface of the plate was assumed adiabatic due to the low thermal conductivity of the material used for the build sheet (ABS). The convection conditions developed at the surface of the curved wedge were governed by a correlation equation that provides a local convection coefficient [6]. The heat removed with the compression wheel, the emissivity, and the ambient temperature for radiation are calibrated based on the printing experiments. The constitutive behavior of the cohesive contact defined between the bottom surface of the printed part and the substrate was also calibrated based on the printing experiments. The substrate was assumed to only fail under mode-I loading. Thus, a maximum stress failure initiation criterion and a displacement-based damage evolution law were used to describe the initiation and evolution of the debonding process, respectively. The cohesive stiffness, cohesive strength, and displacement to failure were calibrated with the print experiments. Table 2.33 lists the parameters related to the process and to the material used in the simulation of the EDAM process of the curved wedge.

Table 2.33: Parameters of the process and material used in simulation of the printing process of the curved wedge.

Parameter	Value
Extrusion Temperature ($°C$)	300
Deposition speed (mm/min)	3175
Ambient Temperature Convection ($°C$)	35
Ambient Temperature Radiation ($°C$)	35
Heat Removed with Compression Wheel (W)	35
Emissivity - ε	0.8
Cohesive Stiffness (MPa/mm)	0.125
Cohesive Strength (KPa)	60
Displacement to Failure (mm)	5

2.4. Results

An extensive material characterization program was conducted in this program to determine the material properties required for simulating the EDAM process with 50% wt. GF-PA . The results of the material characterization were reported in the section Experimental Characterization Of Additively Manufactured Fiber Reinforced Thermoplastic.

A digital material card was generated for the 50% wt. GF-PA with the bead-level effective properties measured experimentally and computed with micromechanics. ADDITIVE3D© was used for simulating the printing process of two printing experiments conducted in the LSAM at Local Motors. The printing experiments consisted of a flat plate printed with two layers in one direction followed by two layers at ninety degrees, thereby giving rise to anticlastic deformation of the plate. A second geometry called curved wedge consisted of a double-bead wall geometry with curved and linear segments in the scale of the components that are of interest for the partners related to the automotive industry. The curved wedge was designed also to warp during and after the printing process. Results of the process simulation are presented in this section and validated against experimental measurements.

Predicting the temperature history is of paramount importance in the EDAM process since temperature controls the evolution of the viscoelastic behavior, crystallization, and shrinkage of the printed material. Figure 2.85 shows a qualitative comparison between the temperature fields captured with the thermal camera (left) and the temperature field predicted in the process simulations (right) after printing the second, the third and the fourth layer. The temperature gradient in both temperature fields are in the same scale. Overall, temperature fields characterized experimentally and predicted through the EDAM process simulations are in a good agreement. The predicted temperature field is slightly colder than the one observed experimentally.

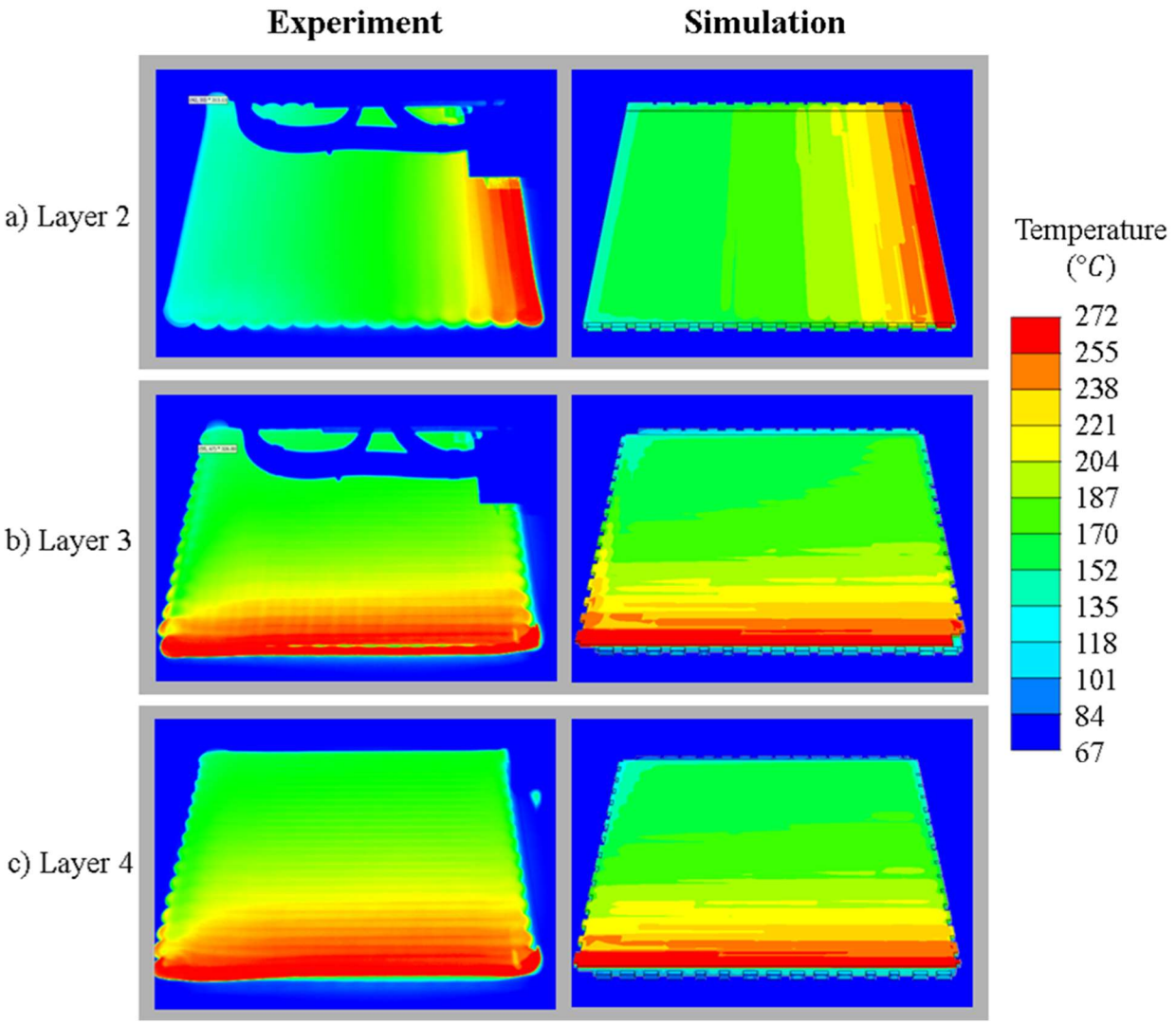

Figure 2.81: Comparison of temperature fields measured experimentally and predicted with process simulation at different instants of the printing process of the plate.

The development of temperature gradients during the printing process of the plate drove the evolution of crystallinity in the same direction than the temperature gradients. Figure 2.82 shows the evolution of the degree of crystallinity as the plate was printed. The crystallinity in the plate started to develop around the end of the second layer and developed from the edge that was deposited first and moved towards the side that was deposited last (Figure 2.82-a). The crystallization of the polymer was not completely developed at the end of the printing process and required about six minutes to reach the maximum crystallinity level of 25% (Figure 2.82-e and d). It should be noted that the temperature fields shown in Figure 2.81 a displayed from a different perspective than the crystallinity fields shown in Figure 2.82.

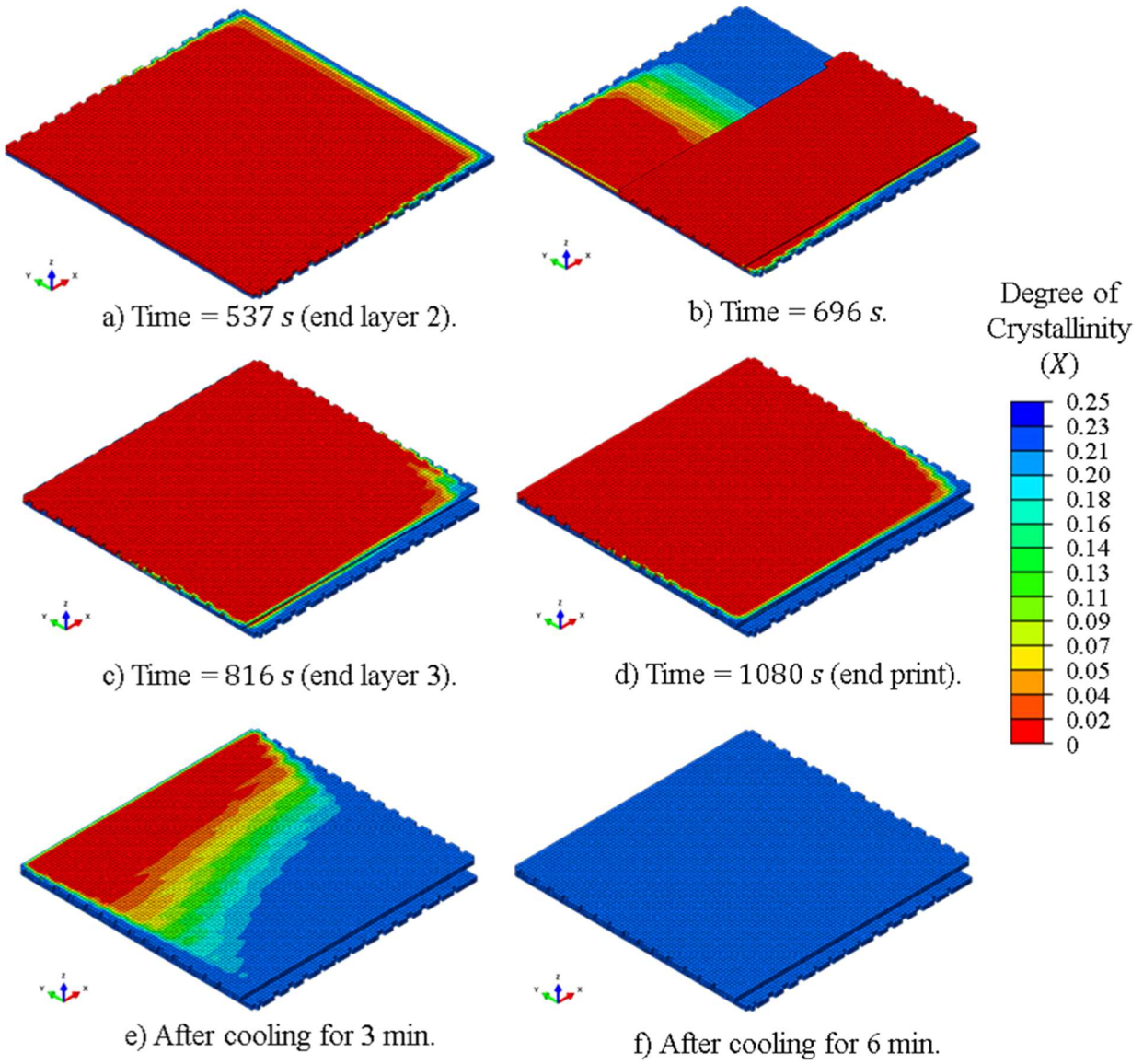

Figure 2.82: Predictions of the degree of crystallinity at different instants of time during the printing process of the plate.

In order to validate the degree of crystallinity, a DSC test was performed. A small sample was extracted at the surface of the plate and heated at a heating rate of 30 °C/min to 280 °C. The goal is to observe the cold crystallization peak. The cold crystallinity peak appears when the material was quenched cool and didn't allow enough time for the polymer chains to crystallize [25]. However, if the material had achieved maximum crystallinity during the cool down process, the cold crystallization peak should not be observed in the heat flow curve. Figure 2.83 shows the heat flow and temperature in blue and green, respectively, recorded in the DSC experiment conducted for validating the degree of crystallinity predicted with ADDITIVE3D. The plot in the left of Figure 2.83 shows the response of the as-received 50% wt. GF-PA pellet. An exothermic reaction

was observed at temperatures around the T_g for the as-received material which corresponds to a cold crystallization phenomena that occurs when a semi-crystalline material is in the amorphous state and the temperature is increased close to T_g [25]. The temperature at the peak of the cold crystallization phenomena is labeled as T_{cc} in Figure 2.83. A similar DSC test was performed for a sample extracted at the surface of the flat plate to confirm that crystallinity has reached the maximum percentage that is possible for this material system (25%) as predicted by the process simulations in ADDITIVE3D. The absence of an exothermic reaction or cold crystallization peak (right side of Figure 2.83) in the heat flow response confirmed the material developed the maximum crystallinity.

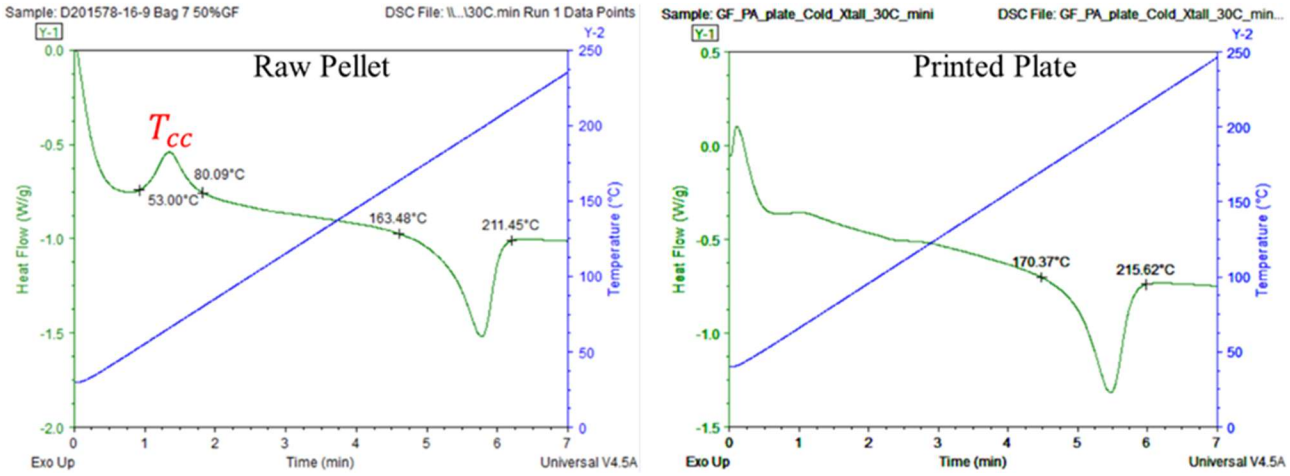

Figure 2.83: DSC experiment of a sample extracted from the flat plat showing no cold crystallization to validate predictions of crystallinity.

A quantitative comparison of the deformation measured in the stacking direction was carried out for the plate. The displacement in the 3-direction was extracted along two profiles located at the middle of the plate and along the two in-plane directions. Figure 2.84 shows the location of the profiles used to extract the deformation of the plate. Data points were extracted from the point cloud shown in Figure 2.73 along the same two profiles. The plot in Figure 2.84 compares the deformation in the stacking direction measured experimentally against the deformation predicted with the simulations. The maximum deformation at the end of the plate in the x profile obtained from the experiment was 19.87 mm whereas the deformation predicted with the process simulation was 19.35 mm. Thus, a maximum difference of about 2.6% was observed between the experimental measurements and the numerical predictions along the X-profile. Similarly, the the largest deformation measured experimentally along the Y-profile was 7.9 mm and the deformation predicted with the process simulation was 9.7 mm for the same location. The difference between the experimental and numerical predictions were below 2% for the most part of the Y-profile and increased to around 23% at the ends of the profile. In general, the simulation predictions are in good agreement with the experimental observations for the most part of the profiles.

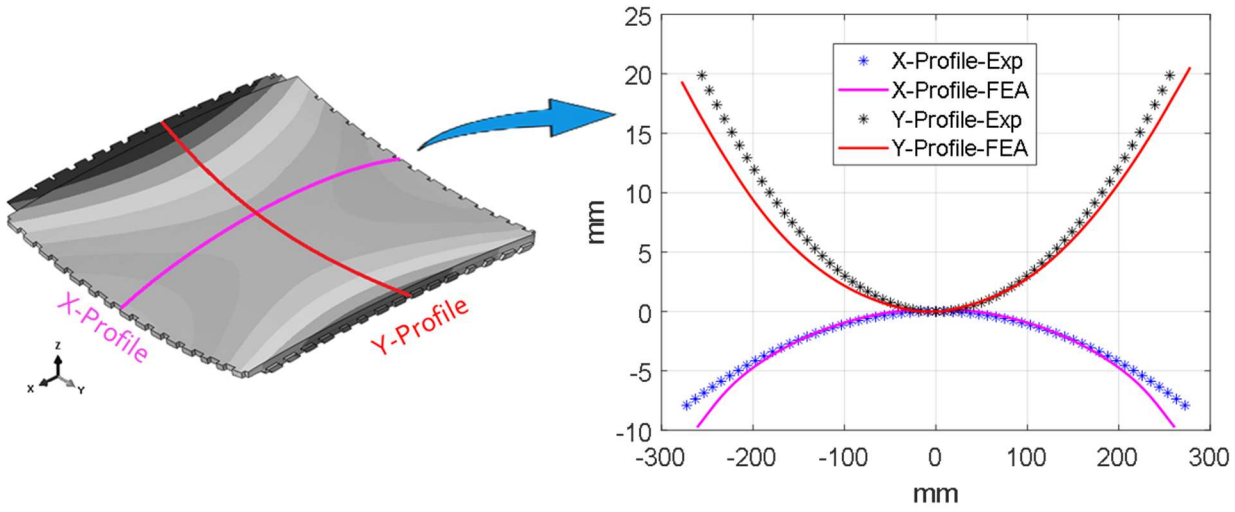

Figure 2.84: Comparison of deformation measured experimentally and predicted in process simulation.

Figure 2.85 shows a qualitative comparison between the temperature field captured with the thermal camera (left) and the temperature field predicted in the process simulations (right) after printing 20 layers, 40 layers and 60 layers. Further, the scales in both temperature fields are in the same temperature range to be able to compare side-to-side the experimental and predicted temperature fields. Overall, a great correlation between the temperature fields characterized experimentally and predicted through the EDAM process simulations was observed.

One observation that should be noted is that the simulation was constructed with a voxel FE mesh. As result of this discretization approach, the surface of the material exposed to convective and radiative heat losses can be overestimated in the curved regions (e.g., by a factor of up to 40% in the worst case). Thereby, the cooling rate is slightly overestimated in the curved regions. A clear example of this is shown in the front corner shown in Figure 2.85 (corner 2) where the temperature predicted with the process simulations is lower by around 10 $°C$ compared to the experimental measurements. Despite the effects introduced by the mesh discretization method in the corners, the temperature distribution predicted in the vertical wall is in great agreement with the experimental measurements.

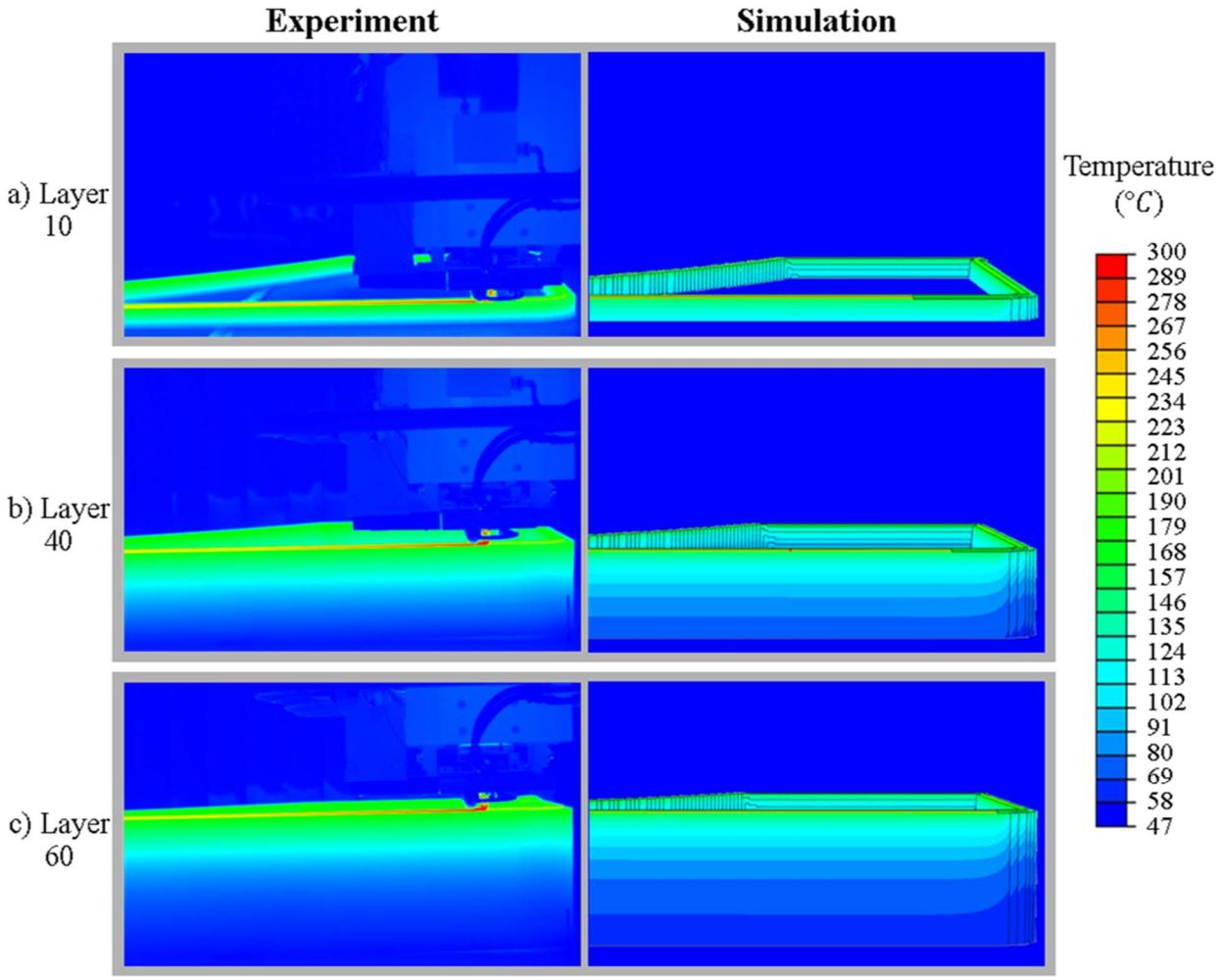

Figure 2.85: Validation of temperature fields characterized experimentally (left) and predicted (right) in the EDAM process simulation. A) Temperature field at layer 20. B) Temperature field at layer 40. C) Temperature field at layer 60.

The transient temperature evolution during the printing process of the curved wedge was extracted at different layer locations for both the experimental temperature measurement and the temperature simulation predictions. A quantitative comparison of the time-temperature history obtained from the simulation and measured experimentally was carried out. Seven layer locations were chosen starting at the layer 10 and increasing in an interval of ten until layer 60. The last layer, number 65, was also included.. Figure 2.86 shows approximately the layer locations from which transient temperature evolution was extracted for both experiment and simulation temperature history. The transient experimental temperature evolution was extracted at the middle of a printed bead right after the material deposited. The simulation temperature of a layer was extracted at the top node of the elements. The temperature history of every 10 layers and the last layer was extracted and imported into Matlab© to plot for visualization.

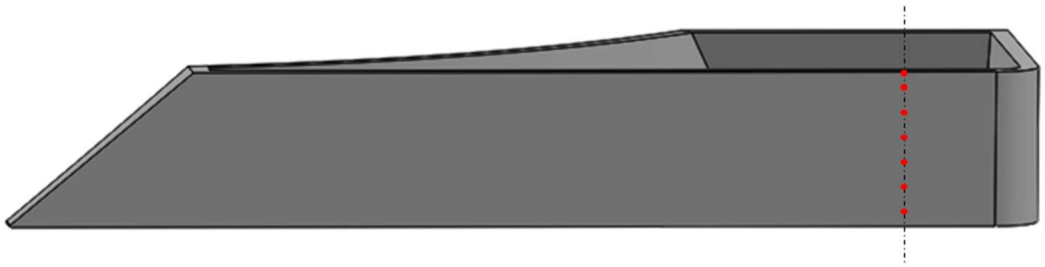

Figure 2.86: Layer locations in the curved wedge used for extracting time-temperature history.

Figure 2.87 compares the experimental and predicted transient temperature evolution at the seven layer locations. The predictions of the transient temperature evolution are in good agreement with the experimental measurements, thereby demonstrating that the relevant heat transfer mechanisms are captured in the EDAM process simulation. The plot of the transient temperature evolution shows the relatively rapid cooling the material undergoes at the surface which is primarily due to heat losses through radiation and due to heat removed by the compression wheel. A local increase in temperature can be also noticed in the first six transient temperature curves as a new layer of material is deposited on top of the layer observed. Once the temperature decreased to about 150 $°C$, the polymer started to crystallize and thus to release heat of crystallization which is not noticeable in the plots of the transient temperature evolution. A more detailed analysis of the heat transfer mechanisms can be found elsewhere [6].

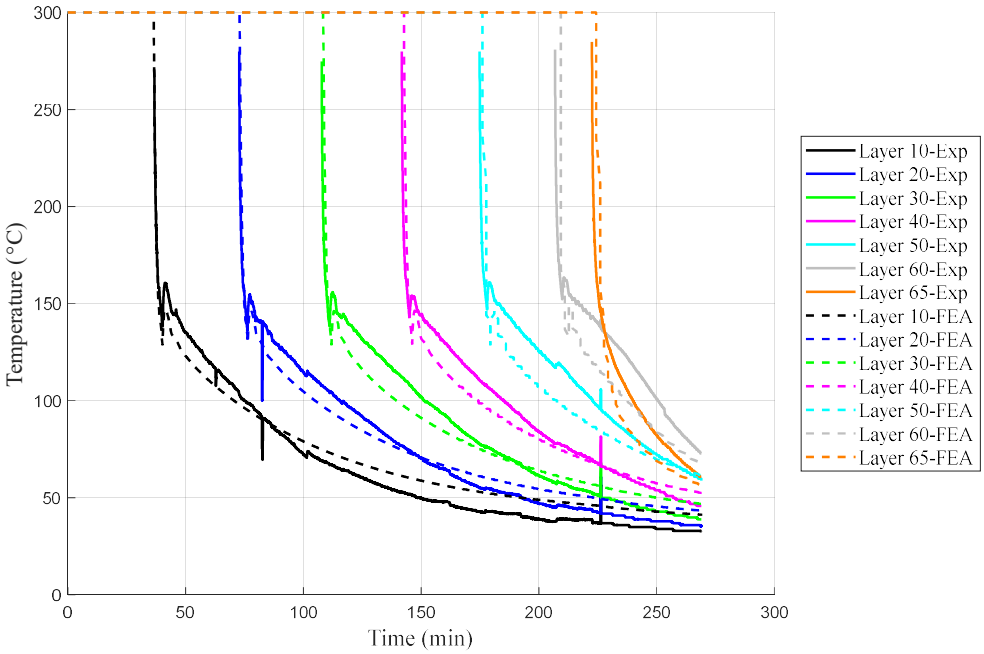

Figure 2.87: Comparison of time-temperature history measured experimentally and predicted with process simulation for different layers in the curved wedge.

The development of temperature gradients along the height of the curved wedge caused the

crystallinity to start developing at the bottom of the part and to progress in the vertical direction as the part was build layer-by-layer. Figure 2.88 shows the evolution of the degree of crystallinity X predicted in the EDAM process simulation of the curved wedge at layer 10, 40, 60 and after cooling for 5 minutes. Since the time between layers was at least three minutes for the curved wedge, the printed material had sufficient time to cool down and to partially crystallize. Thus, the crystallization front closely followed the layer deposition as shown for the 10^{th}, 40^{th}, and 60^{th} layer in Figure 2.88. A degree of crystallinity of 0.25 was achieved in the entire part which corresponds to the maximum degree of crystallinity attained in this material. Achieving the maximum degree of crystallinity is important since it provides thermal stability to the printed material. Furthermore, the crystallinity also affects the thermoviscoelastic behavior of the printed material and the process of crystallization leads to shrinkage [5].

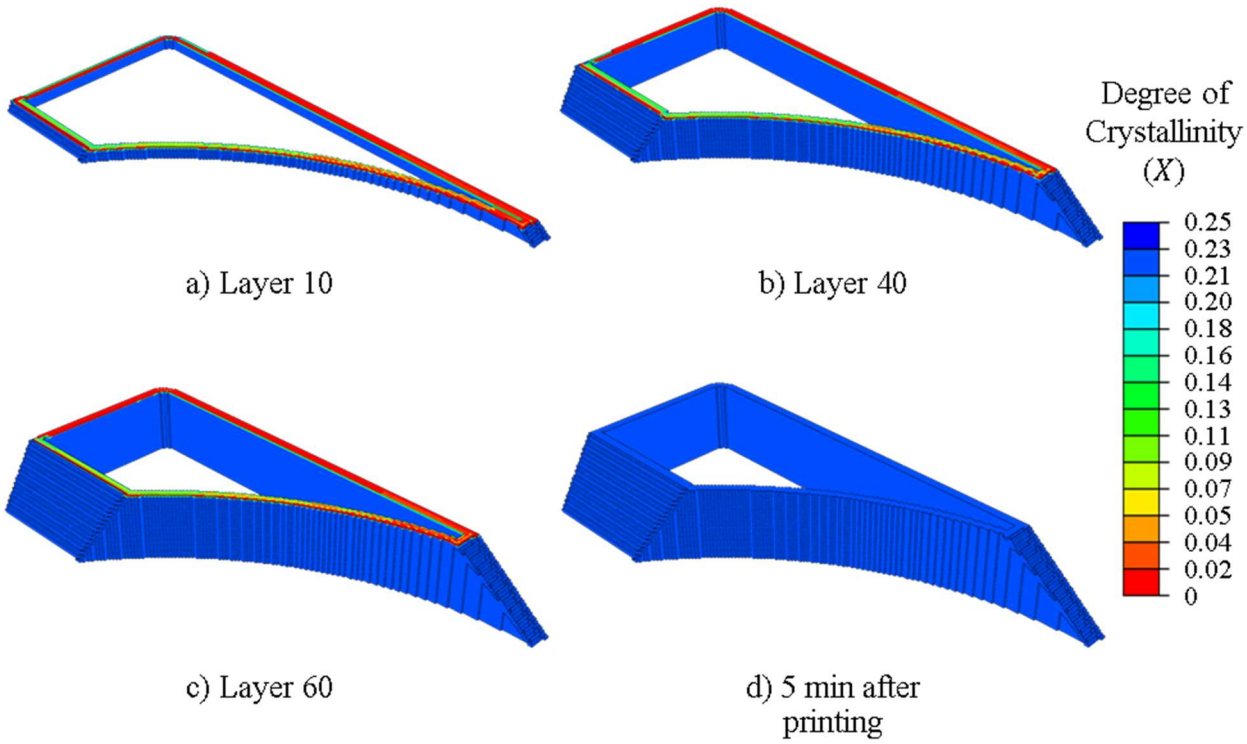

Figure 2.88: Evolution of the degree of crystallinity X predicted in the EDAM process simulation of the curved wedge.

The deformation of the curved throughout the printing process and after cooling was also predicted in the process simulation. The curved wedge was initially bonded to the build sheet and gradually debonded from the build sheet as stresses develop in the part, thereby allowing the part to deform in the vertical direction. Figure 2.89 shows the evolution of the displacement in the layer stacking direction (3-direction) at different instants of the printing process of the curved wedge. The "Corner 1" of the curved wedge (indicated as C-1 in Figure 2.89) debonded from the substrate and started to curve up at around layer 40.

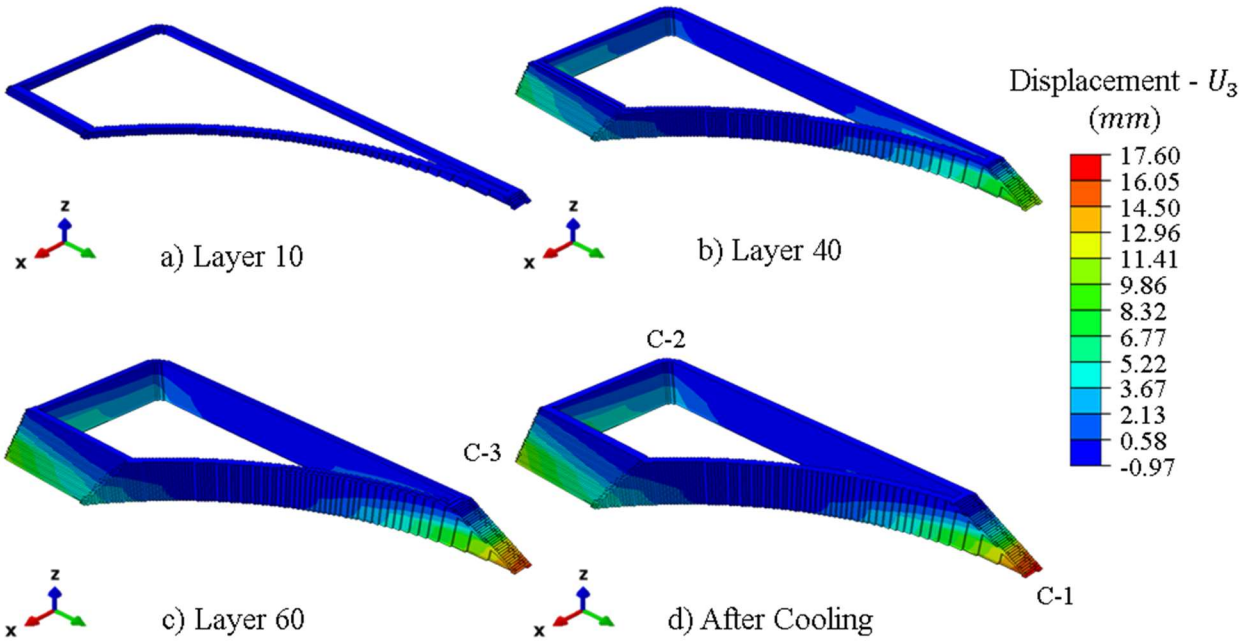

Figure 2.89: Deformation in the layer-stacking direction at different instants of the printing process of the curved wedge.

The deformation measurements carried out at the three different corners of the curved wedge (Table 2.31) were also compared to the deformation extracted at same locations in the process simulations. Table 2.34 shows the comparison between the maximum deformations measured experimentally and the maximum deformation predicted with the simulation of the EDAM process. The deformation predicted for corners 1 and 3 are in good agreement with the experimental observations whereas the deformation in corner 2 was underestimated in the simulations. The difference observed for corner 2 is attributed to the difference in the bonding behavior observed between the two pieces of build sheet used in the experiment (Refer to the section 2.3.2for further details).

Table 2.34: Comparison of deformation at three different corners in the curved wedge measured experimentally and predicted with simulations.

Location	Maximum deformation experiments (mm)	Maximum deformation predictions (mm)	Difference %
Curved wedge, corner 1	16.0	17.6	10.0
Curved wedge, corner 2	13.0	4.1	-68.5
Curved wedge, corner 3	13.0	12.1	-6.9

3. IMPACTS

The effect of additive manufacturing (AM) on energy demand for the aerospace and construction sector showed the potential for energy savings of 5-25% and 4-21%, respectively [1]. Weight reductions that are possible via AM were the largest factor for aerospace energy savings. For automotive and aerospace selective laser sintering (SLS) of metals has led the way, offering more efficient production processes and providing light-weight constructions, which lowers the vehicles energy demand [2]. This work aims to extends the adoption of AM for automotive to include semi-crystalline engineering polymers. Expanding the AM material options for AM helps achieve more sustainable vehicle production by shortening process chains, allowing more efficient process that reduce material consumption, and capturing the benefits of light weight automotive designs. Understanding the viability of a 50% by weight short fiber glass composite system as a 3D Printable resin, will help define the need for carbon fiber reinforced composites for automotive applications. Simulation methods advanced in this work can be applied to a wide variety of materials including both glass and carbon fiber reinforced resins.

The industry partners may leverage the results from this study in a number of ways.

Local Motors may adopt a semi-crystalline glass fiber reinforce material in a future application. Local Motors will uncertainly apply the advanced AM simulation methods validated by this work to augment future vehicle designs.

DuPont will apply the learnings for this project of make future improvements of the AM material offerings. The adoption of DuPont materials for vehicle manufacturing will create a market that will help sustain future material development programs.

4. CONCLUSIONS

An investigation on the effects of process conditions on the fiber orientation distribution and tensile properties was carried out for 50% glass fiber reinforced polyamide (50% wt. GF-PA) printed in the LSAM and the CAMRI system. The nozzle diameter and flow conditions developed in the CAMRI system led to beads with higher alignment of fibers in the print direction compared to the beads printed in the LSAM with a larger nozzle diameter. Further, the difference in the degree of fiber alignment obtained with the two printers was also observed as an increase of about 34% (aspect ratio of 4) in the tensile modulus in the print direction for samples prepared in CAMRI. The elastic properties characterized for both CAMRI and LSAM also showed that the elastic moduli and strengths targeted in this program can be achieved by choosing processing conditions that would produce the desired fiber orientation distribution in the bead. This preliminary investigation showed the potential changes to the anisotropy of the printed material that result from variations in printer systems and configurations (e.g., nozzle size and bead aspect ratio) and which would result in changes to the residual stresses and deformation of a printed part. Future work should continue to focus on understanding the relationship between print processing conditions on the fiber orientation distribution within the printed bead. An improved understanding

of this relationship will expand the ability to tailor design 3D printed parts via modeling and simulation.

The results of mode-I interlayer fracture toughness demonstrated that the measured property met or exceeded the goal of achieving 75% of the interlayer fracture toughness measured from printed specimens that were heat-treated to enhance interdiffusion of polymer chains and achieve maximum crystallinity.

Extensive experimental and virtual material characterization was carried out for the 50% wt. GF-PA printed in the LSAM and CAMRI for beads printed with an aspect ratio of 4. The characterized material properties were used for generating a digital material card to enable simulating the EDAM process with ADDITIVE3D©. Two geometries consisting of a [0/0/90/90] plate and a curved wedge were designed and printed in the LSAM with 50% wt. GF-PA which served for validating the time temperature history, degree of crystallinity, and deformation predicted with ADDITIVE3D©. The degree of crystallinity was predicted to have developed completely at the end of the printing process of the two geometries considered. This prediction was validated with the absence of cold crystallization observed in a DSC experiment carried out with material extracted from the plate geometry. The degree of crystallinity prediction was in great agreement with the results obtained from the DSC experiment. Similarly, the temperature predictions were validated against the temperature field recorded with a thermal camera during the printing process of the geometries. The temperature predictions were in great agreement with the measurements and with maximum variations of around $10\ °C$.

The deformation of the curved wedge and the plates printed in the LSAM were compared with the deformation predicted with the process simulation. The difference in deformation was less than 3% for most of the plate, with the exception of one of the edges of the plate where the difference was greater than 10%. Similarly, the deformation of the curved wedge was measured at the three corners and at the end of the printing process. The predicted deformation was within 10% of the experimental values for two of the corners whereas a larger difference was observed for the third corner. The larger difference in the third corner was attributed to differences in the adhesion characteristics observed between the two sections of build sheet used in the printing experiments. The experimental validation of the simulation predictions provide confidence on the characterization conducted for the printed material and the phenomena considered in the process simulation. Future work should involve additional experimental validation to increase the confidence on the simulation predictions and should investigate more the effects of the build sheet on the residual deformation of the printed part.

5. REFERENCES

[1] L. A. Verhoef, B. W. Budde, C. Chockalingam, B. G. Nodar, and A. J. M. van Wijk, "The effect of additive manufacturing on global energy demand: An assessment using a bottom-up approach," *Energy Policy*, vol. 112, pp. 349–360, 2018.

[2] T. Hettesheimer, S. Hirzel, and H. B. Roß, "Energy savings through additive manufacturing: an analysis of selective laser sintering for automotive and aircraft components," *Energy Effic.*, vol. 11, no. 5, pp. 1227–1245, 2018.

[3] L. J. Love *et al.*, "The importance of carbon fiber to polymer additive manufacturing," *J. Mater. Res.*, vol. 29, no. 17, pp. 1893–1898, 2014, doi: 10.1557/jmr.2014.212.

[4] A. Favaloro, B. Brenken, E. Barocio, and R. B. Pipes, "Simulation of Polymeric Composites Additive Manufacturing using Abaqus," in *Science in the Age of Experience by Dassault Systemes*, 2017.

[5] B. Brenken, "Extrusion Deposition Additive Manufacturing of Fiber Reinforced Semi-crystalline Polymers," Ph.D. Dissertation - Purdue University, 2017.

[6] E. Barocio, "Fusion Bonding of Fiber Reinforced Semi-Crystalline Polymers in Extrusion Deposition Additive Manufacturing," Ph.D. dissertation, Purdue University, 2018.

[7] S. G. Advani and C. L. Tucker, "The Use of Tensors to Describe and Predict Fiber Orientation in Short Fiber Composites," *J. Rheol. (N. Y. N. Y).*, vol. 31, no. 8, pp. 751–784, 1987, doi: 10.1122/1.549945.

[8] ASTM, "D638 Standard Test Method for Tensile Properties of Plastics," *ASTM Int.*, vol. 82, no. C, pp. 1–15, 2016, doi: 10.1520/D0638-14.1.

[9] ASTM, "ASTM D5528 - Standard Test Method for Mode I Interlaminar Fracture Toughness of Unidirectional Fiber-Reinforced Polymer Matrix Composites." 2013.

[10] L. A. Carlsson, D. F. Adams, and R. B. Pipes, *Experimental characterization of advanced composite materials*. CRC press, 2014.

[11] B. Brenken, E. Barocio, A. Favaloro, V. Kunc, and R. B. Pipes, "Development and validation of extrusion deposition additive manufacturing process simulations," *Addit. Manuf.*, vol. 25, pp. 218–226, 2019, doi: 10.1016/j.addma.2018.10.041.

[12] E. Barocio, B. Brenken, A. Favaloro, M. Bogdanor, and R. B. Pipes, "Extrusion Deposition Additive Manufacturing with Fiber-Reinforced Thermoplastic Polymers," in *Structure and Properties of Additive Manufactured Polymer Components*, 1st ed., K. Friedrich and R. Walter, Eds. Woodhead Publishing, 2020, p. 450.

[13] S.-Y. Fu and B. Lauke, "Effects of fiber length and fiber orientation distributions on the tensile strength of short-fiber-reinforced polymers," *Compos. Sci. Technol.*, vol. 56, no. 10, pp. 1179–1190, 1996, doi: http://dx.doi.org/10.1016/S0266-3538(96)00072-3.

[14] H. J. Wolf, "Screw plasticating of discontinuous fiber filled thermoplastic: Mechanisms and prevention of fiber attrition," *Polym. Compos.*, vol. 15, no. 5, pp. 375–383, 1994, doi: 10.1002/pc.750150508.

[15] C. A. Schneider, W. S. Rasband, and K. W. Eliceiri, "NIH Image to ImageJ: 25 years of image analysis," *Nat. Methods*, vol. 9, no. 7, pp. 671–675, 2012.

[16] N. M. Barkoula, B. Alcock, N. O. Cabrera, and T. Peijs, “Fatigue properties of highly oriented polypropylene tapes and all-polypropylene composites,” *Polym. Polym. Compos.*, vol. 16, no. 2, pp. 101–113, 2008, doi: 10.1177/096739110801600203.

[17] ASTM, “Astm D3039/D3039M,” *Annu. B. ASTM Stand.*, pp. 1–13, 2014, doi: 10.1520/D3039.

[18] ASTM, “Standard Test Method for Shear Properties of Composite Materials by the V-Notched,” *Annu. B. ASTM Stand.*, no. March, pp. 1–13, 2012, doi: 10.1520/D5379.

[19] T. Mori and K. Tanaka, “Average stress in matrix and average elastic energy of materials with misfitting inclusions,” *Acta Metall.*, vol. 21, no. 5, pp. 571–574, 1973.

[20] Digimat, “Digimat User’s Manual.” Belgium, 2019.

[21] MatWeb, “E-Glass Fiber, Generic.” .

[22] S. K. Dey and M. Xanthos, “Glass Fibers,” *Funct. Fill. Plast.*, vol. 21, no. Ref 19, pp. 141–162, 2010, doi: 10.1002/9783527629848.ch7.

[23] ASTM, “Standard test method for thermal diffusivity of solids by the flash method (E1461-01),” *Am. Soc. Test. Mater.*, vol. 14, no. 2, pp. 1–13, 2001, doi: 10.1520/E1461-13.2.

[24] Y. Wang, H. L. Kang, R. Wang, R. G. Liu, and X. M. Hao, “Crystallization of polyamide 56/polyamide 66 blends: Non-isothermal crystallization kinetics,” *J. Appl. Polym. Sci.*, vol. 135, no. 26, pp. 1–13, 2018, doi: 10.1002/app.46409.

[25] E. Piorkowska and G. C. Rutledge, *Handbook of polymer crystallization*. John Wiley & Sons, 2013.

[26] C. N. Velisaris and J. C. Seferis, “Crystallization kinetics of polyetheretherketone (peek) matrices,” *Polym. Eng. Sci.*, vol. 26, no. 22, pp. 1574–1581, 1986, doi: 10.1002/pen.760262208.

[27] A. Greco and A. Maffezzoli, “Statistical and kinetic approaches for linear low-density polyethylene melting modeling,” *J. Appl. Polym. Sci.*, vol. 89, no. 2, pp. 289–295, 2003, doi: 10.1002/app.12079.

[28] E. A. Turi, *Thermal Characterization of Polymeric Materials*, Second Edi. Brooklyn: Academic Press, 1997.

[29] H. F. Brinson and L. C. Brinson, *Polymer engineering science and viscoelasticity: An introduction, Second edition*. 2015.

[30] P. Sunderland, W. Yu, and J.-A. MÃ¥nson, “A thermoviscoelastic analysis of process-induced internal stresses in thermoplastic matrix composites,” *Polym. Compos.*, vol. 22, no. 5, pp. 579–592, 2001, doi: 10.1002/pc.10561.

[31] B. Brenken, “Extrusion Deposition Additive Manufacturing of Fiber Reinforced Semi-crystalline Polymers,” Ph.D. dissertation, Purdue University, 2017.

[32] Dassault Systèmes, “SIMULIA User Assistance 2019,” 2019. [Online]. Available: https://help.3ds.com/. [Accessed: 09-Oct-2019].

LEAD PARTNER BACKGROUND

DuPont de Nemours, Inc., with $21.5 billion 2019 revenues, provides technology-based materials, ingredients and solutions. As a global company, with headquarters in Wilmington, DE USA, it offers products and solutions across four businesses: Electronics and Imaging, Nutrition and Biosciences, Safety and Construction, and Transportation and Industrial. DuPont provides solutions to a range of markets, including automotive, building and construction, energy, government and public sector, military, law enforcement, emergency response, packaging and printing, and safety and protection industries. The Company provides materials for additive manufacturing (AM) machines reinforced with both carbon and glass fibers. The advanced simulation methods for AM developed in this work supports the adoption of these AM materials into commercial applications.

APPENDIX

Table 5.1: Components of the fiber orientation tensor for each section of the bead printed in the LSAM with an aspect ratio of 4.

A11 = 0.58	1	2	3	4
1	0.68	0.57	0.58	0.63
2	0.66	0.47	0.51	0.61
3	0.62	0.44	0.43	0.61
4	0.62	0.49	0.45	0.62
5	0.67	0.62	0.6	0.68
6	0.64	0.64	0.6	0.54

A22 = 0.32	1	2	3	4
1	0.2	0.31	0.31	0.22
2	0.23	0.45	0.4	0.25
3	0.29	0.5	0.5	0.29
4	0.3	0.44	0.49	0.3
5	0.23	0.29	0.31	0.23
6	0.24	0.26	0.3	0.35

A33 = 0.10	1	2	3	4
1	0.13	0.11	0.11	0.15
2	0.11	0.08	0.08	0.14
3	0.09	0.06	0.06	0.1
4	0.08	0.07	0.06	0.08
5	0.1	0.09	0.09	0.09
6	0.12	0.1	0.1	0.11

Table 5.2: Area weighted components of the fiber orientation tensor for each section of the bead printed in the LSAM with an aspect ratio of 4.

Weighted A11 = 0.57	**1**	**2**	**3**	**4**
1	0.32	0.33	0.31	0.27
2	0.58	0.47	0.51	0.49
3	0.60	0.44	0.43	0.52
4	0.59	0.49	0.45	0.52
5	0.60	0.62	0.60	0.52
6	0.26	0.20	0.12	0.04
Weighted A22 = 0.34	**1**	**2**	**3**	**4**
1	0.09	0.18	0.17	0.09
2	0.20	0.45	0.40	0.20
3	0.28	0.50	0.50	0.25
4	0.29	0.44	0.49	0.25
5	0.21	0.29	0.31	0.17
6	0.10	0.08	0.06	0.02
Weighted A33 = 0.09	**1**	**2**	**3**	**4**
1	0.06	0.06	0.06	0.06
2	0.10	0.08	0.08	0.11
3	0.09	0.06	0.06	0.09
4	0.08	0.07	0.06	0.07
5	0.09	0.09	0.09	0.07
6	0.05	0.03	0.02	0.01

Table 5.3: Area weighted components of the fiber orientation tensor for regions of the bead used in the tensile and shear specimens prepared from panels printed in LSAM (AR=4).

Weighted A11 after Machining = 0.53	**1**	**2**	**3**	**4**
1	0.06	0.10	0.10	0.05
2	0.10	0.47	0.51	0.09
3	0.09	0.44	0.43	0.09
4	0.09	0.49	0.45	0.09
5	0.10	0.62	0.60	0.10
6	0.04	0.05	0.04	0.01
Weighted A22 after Machining = 0.39	**1**	**2**	**3**	**4**
1	0.02	0.05	0.05	0.02
2	0.03	0.45	0.40	0.04
3	0.04	0.50	0.50	0.04
4	0.04	0.44	0.49	0.04
5	0.03	0.29	0.31	0.03
6	0.01	0.02	0.02	0.01
Weighted A33 after Machining = 0.08	**1**	**2**	**3**	**4**
1	0.01	0.02	0.02	0.01
2	0.02	0.08	0.08	0.02
3	0.01	0.06	0.06	0.01
4	0.01	0.07	0.06	0.01
5	0.01	0.09	0.09	0.01
6	0.01	0.01	0.01	0.00

Tensile specimen dimensions

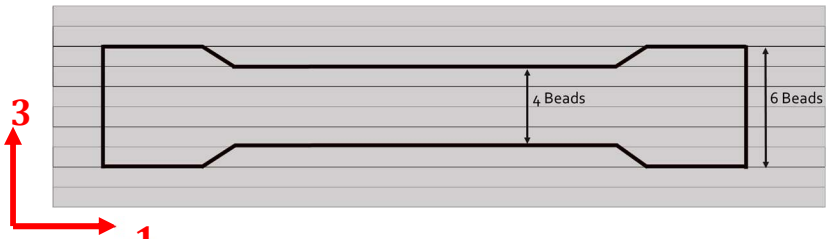

(a) Beads in the gage and tab region

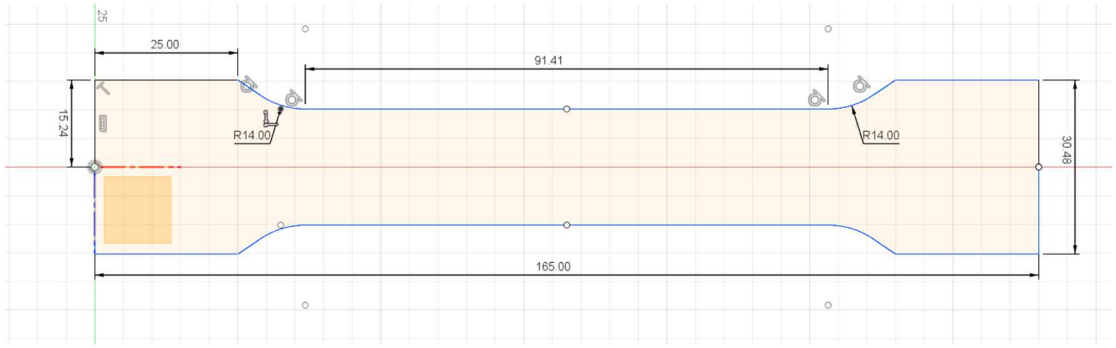

(a) Dimensions of the tensile specimen in mm

Figure 5.1: Dimensions of specimens prepared for testing tensile properties in the 1-direction.

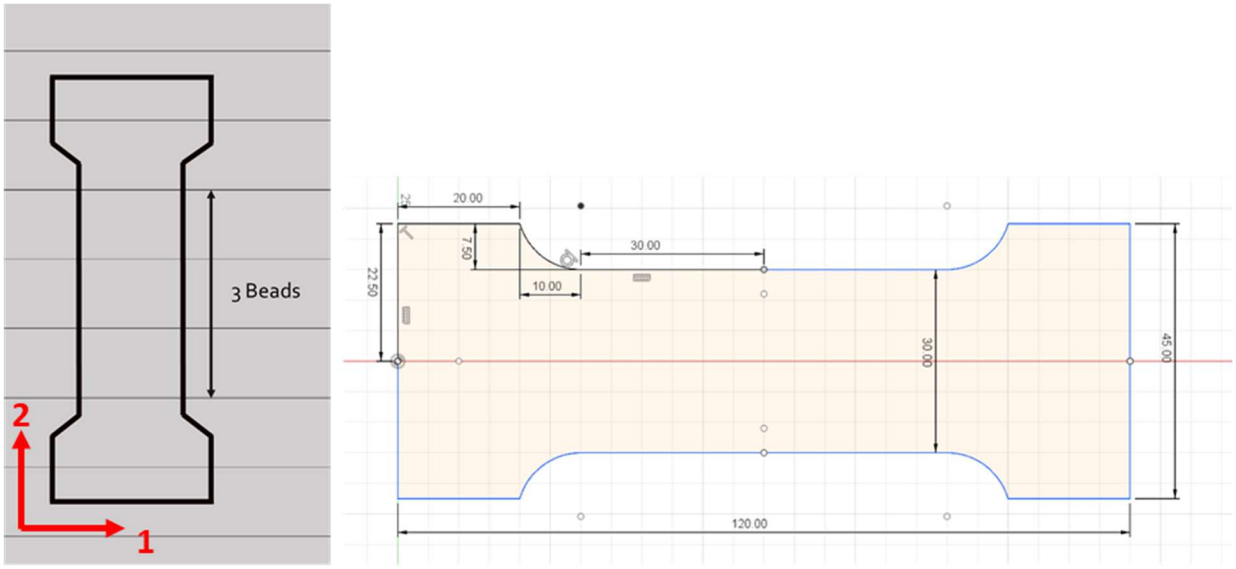

Figure 5.2: Dimension of the Tensile Specimen in the 2 Direction.

direction.

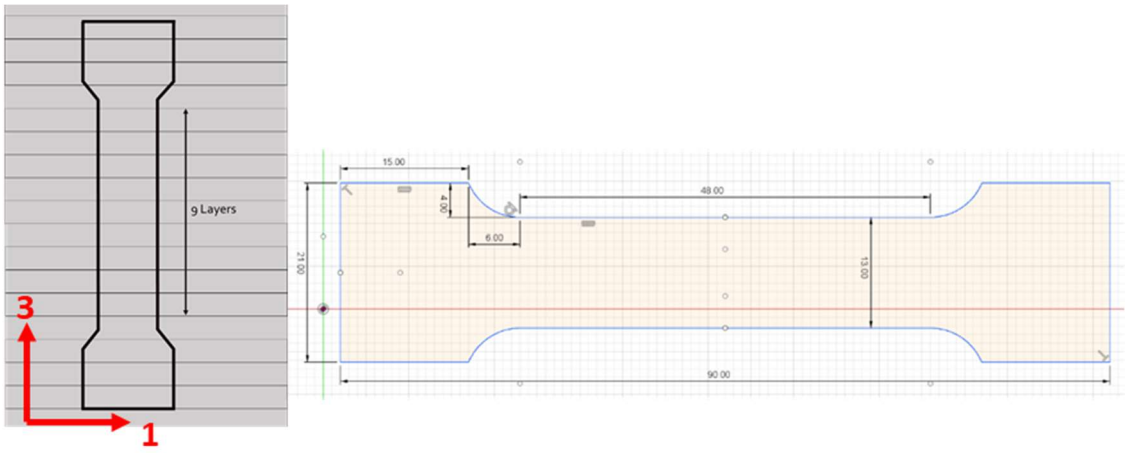

Figure 5.3: Dimension of the Tensile Specimen in the 3 Direction.

Table 5.4: Heat Capacity as a Function of Temperature.

Temperature (◦C)	Heat Capacity (W·sec/gm·K)
23	1.1459
25	1.1528
30	1.1702
35	1.1876
40	1.2051
45	1.2227
50	1.2404
55	1.2582
60	1.276
65	1.294
70	1.312
75	1.3301
80	1.3483
85	1.3666
90	1.3851
95	1.4034
100	1.4222
105	1.4442
110	1.4688
115	1.499
120	1.5316
125	1.5603
130	1.5866
135	1.6121
140	1.6346
145	1.6541
150	1.6686
155	1.6818
160	1.698

Temperature (◦C)	Heat Capacity (W·sec/gm·K)
165	1.7223
170	1.7584
175	1.8118
180	1.8895
185	2.0259
190	2.1986
195	2.3359
200	2.2758
205	1.9933
210	1.7797
215	1.7216
220	1.7113
225	1.7139
230	1.7196
235	1.7254
240	1.7322
245	1.7393
250	1.7462
255	1.7528
260	1.7595
265	1.7659
270	1.7723
275	1.7786
280	1.7856
285	1.7918
290	1.7978
295	1.8038
300	1.8058

Table 5.5: Thermal Conductivity of 50% wt. GF-PA as a Function of Temperature in the Three Principal Direction.

	Temperature (◦C)	Density (g/cm^3)	Specific Heat (W·sec/g·K)	Diffusivity (cm^2/sec)	Thermal Conductivity (W/cm·K)
1-Direction	23	1.4083	1.1459	0.00249	0.403
	50	1.4083	1.2404	0.00232	0.407
	100	1.4083	1.4222	0.00203	0.406
	150	1.4083	1.5686	0.0018	0.397
	200	1.4083	1.6815	0.00152	0.361
	250	1.4083	1.7462	0.00105	0.258
	300	1.4083	1.8058	0.0009	0.228
2- Direction	23	1.4931	1.1459	0.00279	0.478
	50	1.4931	1.2404	0.0026	0.481
	100	1.4931	1.4222	0.00225	0.477
	150	1.4931	1.5686	0.00192	0.449
	200	1.4931	1.6815	0.00162	0.408
	250	1.4931	1.7462	0.0001	0.28
	300	1.4931	1.8058	0.0001	0.27
3- Direction	23	1.4164	1.1459	0.00212	0.345
	50	1.4164	1.2404	0.00203	0.356
	100	1.4164	1.4222	0.00175	0.352
	150	1.4164	1.5686	0.00151	0.335
	200	1.4164	1.6815	0.00133	0.316

Table 5.6: Summary of the Prony series descriptions of the TTS mater curves for the moduli E_1 and E_2.

λ_w relaxation time (s)	E_{1w} (MPa)	E_{2w} (MPa)
-	229.84	20
10^{-7}	3.0E-14	2.3E-14
10^{-6}	2.2E-14	4.4E-14
10^{-5}	2.2E-14	4.3E-14
10^{-4}	2.2E-14	75.16
10^{-3}	94.14	143.16
10^{-2}	350.88	369.77
10^{-1}	385.04	165.76
1	279.96	175.35
10^{1}	136.53	91.10
10^{2}	123.79	68.65
10^{3}	229.57	82.54
10^{4}	235.36	78.97
10^{5}	129.41	38.84
10^{6}	110.49	31.08
10^{7}	118.27	25.92
10^{8}	80.10	26.10
10^{9}	94.37	24.23
10^{10}	81.90	21.54
10^{11}	113.55	34.16
10^{12}	42.28	22.45
10^{13}	172.15	22.72